HIGH POWER ION CYCLOTRON RESONANCE HEATING IN THE WISCONSIN LEVITATED OCTUPOLE

by

CLIFFORD MARK FORTGANG

A thesis submitted in partial fulfillment of the
requirements for the degree of

DOCTOR OF PHILOSOPHY
(Physics)

at the

UNIVERSITY OF WISCONSIN-MADISON

1983

ABSTRACT

HIGH POWER ION CYCLOTRON RESONANCE HEATING IN THE WISCONSIN LEVITATED OCTUPOLE

Clifford Mark Fortgang

Under the supervision of Professor J.C. Sprott

Ion cyclotron resonance heating has been investigated, both experimentally and theoretically, on the Wisconsin Levitated Octupole. Heating of both ions and electrons has been observed. Typically, a two component ion energy distribution is produced (300 eV and 50 eV) with the application of 500 kW of RF power into a 5×10^{12} cm^{-3} density plasma. Power is coupled to the plasma with an antenna that also serves as the inductor of an oscillator tank circuit. The oscillator is tunable from 1-3 MHz and can be applied for periods up to 10 msec. The experiments were performed with hydrogen, gun injected plasmas.

Most of the theoretical work presented deals with a calculation that predicts the plasma loading. A slab model is used, and the questions of accessibility, polarization, and damping of the radio frequency electromagnetic fields are addressed. It is found that cold plasma theory cannot account for the heating, and therefore hot plasma theory is invoked to explain the heating. The loading measurements and theoretical predictions are found to be in reasonable agreement.

Neutral reflux from the walls is enhanced with the application of RF. Charge exchange limits the ion energy confinement, and impurity radiation limits the electron energy confinement. An ion temperature profile, obtained with a gridded ion energy analyzer probe, shows the ion temperature peaking on the magnetic flux surface that crosses the resonance zone nearest to the antenna.

J. C. Sprott

ACKNOWLEDGEMENTS

I would like to thank Professor J.C. Sprott for his support and enthusiasm throughout the duration of my research. It has been a privilege and an invaluable experience working with Dr. E.J. Strait. Most of the data presented in this thesis was obtained in conjunction with Dr. Strait. My many discussions with Dr. Strait were both productive and enjoyable.

There were a number of contributors to various technical aspects of the experiment. T. Lovell designed the antenna and provided me with an excellent introduction to the subject of radio frequency electronics. J. Laufenberg, and his staff, do an excellent job in keeping the Octupole running, as well as, designing and building first-rate electronic circuits. Dr. J. Barter fabricated the original oscillator and provided profitable assistance in the early stages of the experiment.

All my fellow graduate students, especially those on the Levitated Octupole: Arnie Kellman, Mike Zarnstorff, Stephen Painchaud, and Greg Severn were of great help. Their friendship and advice were essential in completing this work.

The ideas and assistance, received from Professors R.N. Dexter and S.C. Prager, are gratefully acknowledged.

The moral support of my friend, Linda Kristensen, was very important to me, especially when things weren't going according to plan. Her patience and encouragement were extremely helpful.

None of this would have been possible without the guidance and support of my father. Though he has recently passed on he is still with me, in my heart, providing an example I can look up to, of a fine and decent human being.

Financial support was provided by the United States Department of Energy.

TABLE OF CONTENTS

CHAPTER 1

INTRODUCTION

All magnetically confined plasmas require some form of heating to reach the temperatures required to ignite the fusion reaction[1]. Ohmic heating fails, in most confinement devices, as the temperature rises because the high electrical conductivity necessitates unacceptably large plasma currents. Neutral beam heating is technologically difficult. As a result, radio frequency heating has become a major focus of numerous plasma physics experiments[2-8]. In particular, ion cyclotron resonance heating (ICRH) is especially attractive because it heats ions directly, with good efficiency ($\gtrsim$50%), and uses well established technology.

This thesis describes an investigation of ion cyclotron resonance heating in the Wisconsin Levitated Octupole. The experiments were performed with hydrogen, gun injected plasmas, at the fundamental ion cyclotron frequency. For the reader more familiar with fast wave heating on tokamaks there are important differences with the Octupole experiment that should be pointed out. Since the Octupole magnetic field is poloidal, the antenna is oriented in the toroidal direction. Figure 1.1 shows the Octupole flux lines, the position of the antenna (which spans 120° toroidally), Faraday shield, and a typical resonant mod-B surface.

Fig. 1.1 Octupole poloidal field lines with a typical resonance zone. The antenna is Faraday shielded, spans 120° in the toroidal direction, and is located on the midcylinder, 4.5 cm above the lower lid.

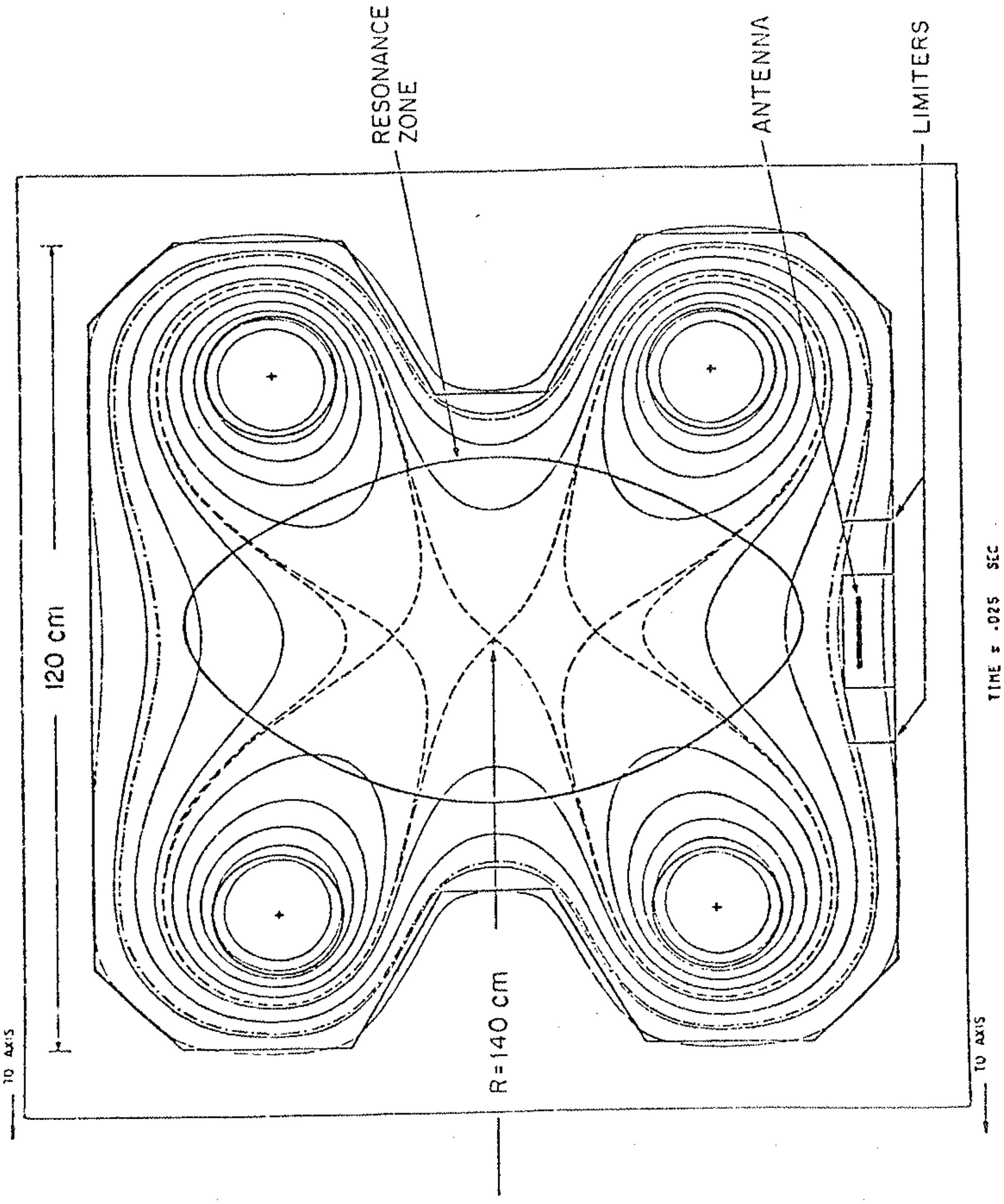
RESONANCE ZONE
ANTENNA
LIMITERS
120 cm
R=140 cm
TO AXIS
TO AXIS
TIME = .025 SEC

Unlike the small spatial variation in the toroidal field of a tokamak, the Octupole poloidal magnetic field varies widely from $|\vec{B}|=0$ at the center, to typically 1 kG at the Faraday shield, to 5 kG in the bridges, the narrow region between the rings and machine wall. These field strengths require RF driving frequencies in the range of 1-3 MHz, which are somewhat lower than typically found on tokamak experiments. However, there are some similarities with tokamaks. For example, the presence of the perpendicular ion cyclotron resonance[9] between the antenna and the $\omega=\omega_{ci}$ layer for the case of high field incidence. Hot plasma effects and parallel wavelength spectra[10] are used to explain the heating in the Octupole as well as in tokamaks.

This thesis makes some direct comparisons with a similar experiment performed by J. Barter and J. C. Sprott[11,12,13] on the Small Octupole, a device which preceded the Levitated Octupole. This experiment extends the work done by Barter to a larger machine, at higher density (10^{10}-10^{11} to 10^{12}-10^{13} cm^{-3}), and higher RF power ($\simeq$100 kW to $\simeq$500 kW). Though similar in design the new parameter regime brought both some expected and unexpected results. For example, electron drag becomes a power loss channel for the ions, thus making impurity radiation an important process for power balance. Also, the plasma loading is observed to be lighter than was originally expected from a simple density and size scaling from Barter's experiment. A theoretical explanation is presented which considers the plasma response to the RF fields, and thus modifications to the vacuum electric field polarization.

In Chapter 2 a description of the Levitated Octupole, the RF source and antenna, and the diagnostics is presented. A more thorough discussion is given for the diagnostics that were especially important to this experiment in particular, such as the charge exchange analyzer and the RF magnetic probe.

A theoretical model for calculating the loading is presented in Chapter 3. In order to do this, one has to consider the questions of accessibility, polarization, and damping. With certain simplifying assumptions these questions are addressed, providing a predicted plasma radiation resistance which can be compared with experimental measurement. Fortunately, measurements of the toroidal component to the RF electric field in the presence of plasma can be made and provide an additional test of the theory.

In Chapter 4 the measured scaling of plasma loading with magnetic field, density, and power is presented, along with the theoretical predictions. Heating results are also discussed. Typically, 500 kW of RF power is coupled to the plasma, and both ion and electron heating are observed. With highly convoluted field lines and an antenna that spans only 120° around the machine, the Octupole is a truly three-dimensional machine. This fact makes it difficult to model all the atomic (e.g. charge exchange, impurity radiation) and classical particle transport effects that are taking place. However, various types of probes can be inserted into the plasma, and, along with other diagnostics (charge exchange, optical, bolometer), a qualitative picture can be made for the dominant processes in the power balance.

Chapter 5 includes conclusions and proposals for future work.

In this thesis references are made to PLP reports, internal papers of the University of Wisconsin Plasma Physics Group. Copies of these reports are available on request from:

Plasma Physics Department
University of Wisconsin
1150 University Avenue
Madison, WI 53706.

REFERENCES - CHAPTER 1

1. S.O. Dean, J.D. Callen, H.P. Furth, T. Ohkawa, P.H. Rutherford, S.C. Burnett, J.B. McBride, and N.A. Davies, Status and Objectives of Tokamak Systems for Fusion Research, (WASH 1295, USERDA).

2. P.L. Colestock, S.L. Davis, J.C. Hosea, D.Q. Hwang, and H.R. Thompson, Proceedings of the Second Joint Grenoble-Varenna International Sypmposium on Heating in Toroidal Plasmas, Grenoble, Vol. 1, p. 471 (1980).

3. T.L. Owens, J.H. Mullen, F.W. Baity, W.A. Davis, O.C. Eldridge, D.L. Hillis, Nuclear Fusion 23,49 (1983).

4. R.J. Taylor, G.J. Morales, Proceedings of the Second Joint Grenoble-Varenna International Symposium on Heating in Toroidal Plasmas, Grenoble, Vol. 1, p. 509 (1980).

5. M.P.J. Gaudreau, M. Sansone, B.D. Blackwell, F. Knowlton, D. Lavoie, C. Holtier, and B. Abbanat, Proceedings of the Fourth Topical Conference on Radio Frequency Plasma Heating, Austin, A9 (1981).

6. Y. Lapierre, TFR Group, Proceedings of the Fourth Topical Conference on Radio Frequency Plasma Heating, Austin, A12 (1981).

7. A.W. Molvik, S. Falabella, and T. Moore, Proceedings of the Fifth Topical Conference on Radio Frequency Plasma Heating, Madison, A-1.5 (1983).

8. P.P. Lallia, P.H. Rebut, and J. Jacquinot, Proceedings of the Fifth Topical Conference on Radio Frequency Plasma Heating, Madison, B-1.1 (1983).

   Reports on additional experiments as well as theoretical papers can be found in the proceedings of the conferences referenced above.

9. F.W. Perkins, Nuclear Fusion 17,1197 (1977).

10. J.E. Scharer, B.D. McVey, and T.K. Mau, Nuclear Fusion 17,297 (1977).

11. J.D. Barter, Ph.D. Thesis, University of Wisconsin (1976).

12. J.D. Barter and J.C. Sprott, Phys. Rev. Lett. 34,1607 (1975).

13. J.D. Barter and J.C. Sprott, Plasma Physics 19,945 (1977).

CHAPTER 2

APPARATUS

2.1 Machine Description

The Wisconsin Levitated Octupole is shown in Fig. 2.1. Descriptions of multipoles and their confinement properties[1] in general and of the Wisconsin Levitated Octupole[2,3] in particular have been discussed in detail elsewhere. A brief discussion will be given here.

The machine is a toroidal device with four internal rings which are inductively driven to form the octupole poloidal field. A poloidal gap prevents the machine wall from shorting out the internal rings. The Octupole can be thought of as a transformer where all the flux created by the secondary (the rings) is leakage flux which remains inside the machine. A capacitor bank and the primary windings on the iron core form an LC resonant circuit with a half-period of ~43 msec. Plasma experiments are run near peak magnetic field, ~21 msec. The rings are supported by prods which can be pneumatically removed for a period of 20 msec during which the plasma experiment is performed. A combination of magnetic pressure and inertia keep the rings stationary or levitated until the prods are reinserted after the experiment. The important specifications for the machine are listed in Table 2.1.

Fig. 2.1 Wisconsin Levitated Octupole

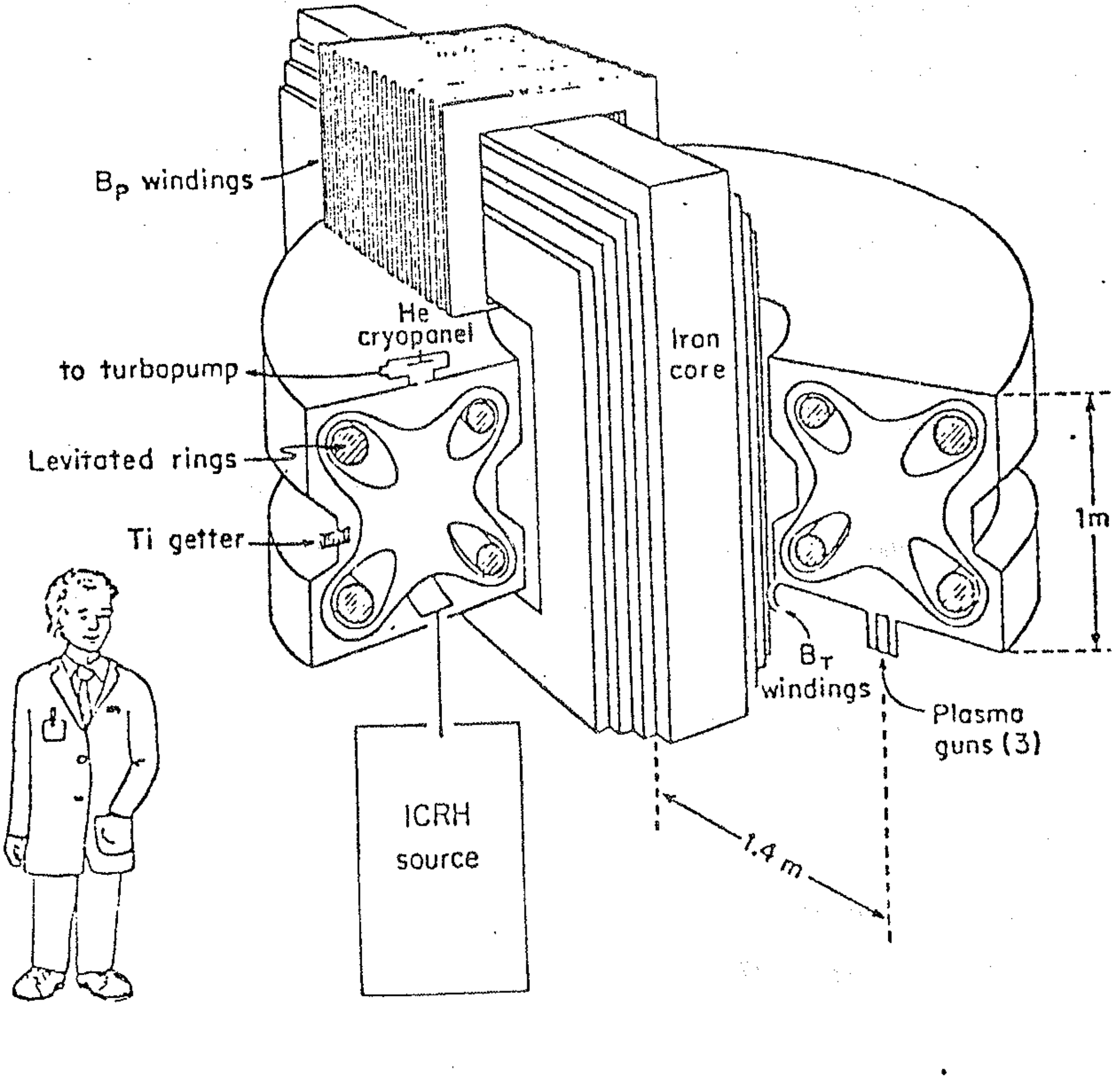
B_p windings
He cryopanel
to turbopump
Levitated rings
Ti getter
Iron core
1m
B_T windings
Plasma guns (3)
ICRH source
1.4 m

TABLE 2.1 LEVITATED OCTUPOLE PARAMETERS

Major Radius:	140 cm	Vacuum Tank volume:	8.6 m^3
Minor Radius (typical):	50 cm	MHD Stable Volume:	7.7 m^3
Minor Radius of Rings:	8.9 cm		

Magnetic Fields: Uncrowbarred Pulse Length: 43 msec

Crowbarred Decay Time: 70 msec

Poloidal Field

	Inner Ring	Outer Ring	Wall
Max. B at Surface:	11.6 kG	5.6 kG	8.5 kG
Current:	.46 MA	.25 MA	1.43 MA

Engergy: .60 MJ

Toroidal Field

B at midcylinder: 450 G

Energy: 37 kJ

Figures 2.2 and 2.3 show the poloidal flux plot and mod-B surfaces, respectively. There are two kinds of flux lines, private flux which encircles one ring and common flux which encircles all four rings. The separatrix, ψ_{sep}, is the flux line that separates the two regions of flux. The center of the machine has a degenerate field null, and so most of the plasma volume is situated in a minimum average B magnetic well. The strongest magnetic fields are in the bridges, the narrow regions between the rings and the machine wall. The outermost dashed line in Figure 2.2 is called the critical surface, ψ_{crit}, which marks the boundary where the flux lines go from being average good to average bad curvature. Thus, outside ψ_{crit} the plasma is unstable to the interchange mode. As a matter of convenience the poloidal flux lines are labelled in units of Dories with 10 Dories being the total flux that enters the machine through the gap. At peak field $\psi_{sep}\approx 5.7$, $\psi_{crit}\approx 7.8$, and in the lower outer bridge $\psi\approx 2.5$ is at the ring. At maximum field strength there is 0.72 webers of poloidal flux.

There is also a toroidal gap, and by running current in the machine walls a toroidal field with the usual 1/R dependence is produced. Most of the data taken for this thesis was without toroidal field.

The machine vacuum is maintained with two turbomolecular pumps, a helium cryo pump, and six titanium getters which are situated around the machine on the upper and lower lids. Typical pressures are 6×10^{-8} torr with hydrogen and water being the major constituents

Fig. 2.2 Poloidal cross-section of Octupole showing flux surfaces labelled in Dories.

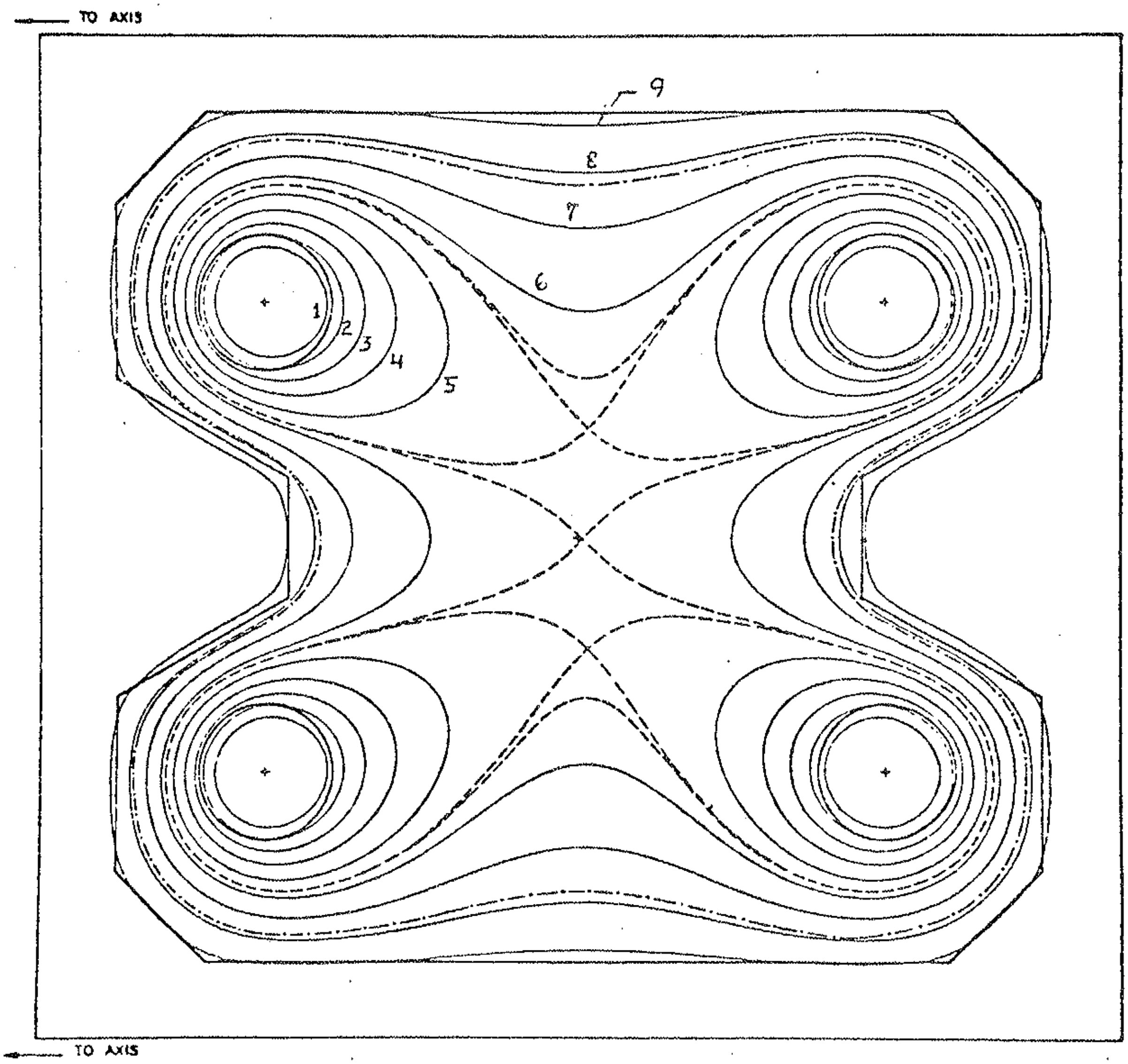

Time= .025 sec

Fig. 2.3 Poloidal cross-section of Octupole showing mod-B contours (units in kG) for 0.63 Webers of flux in the machine.

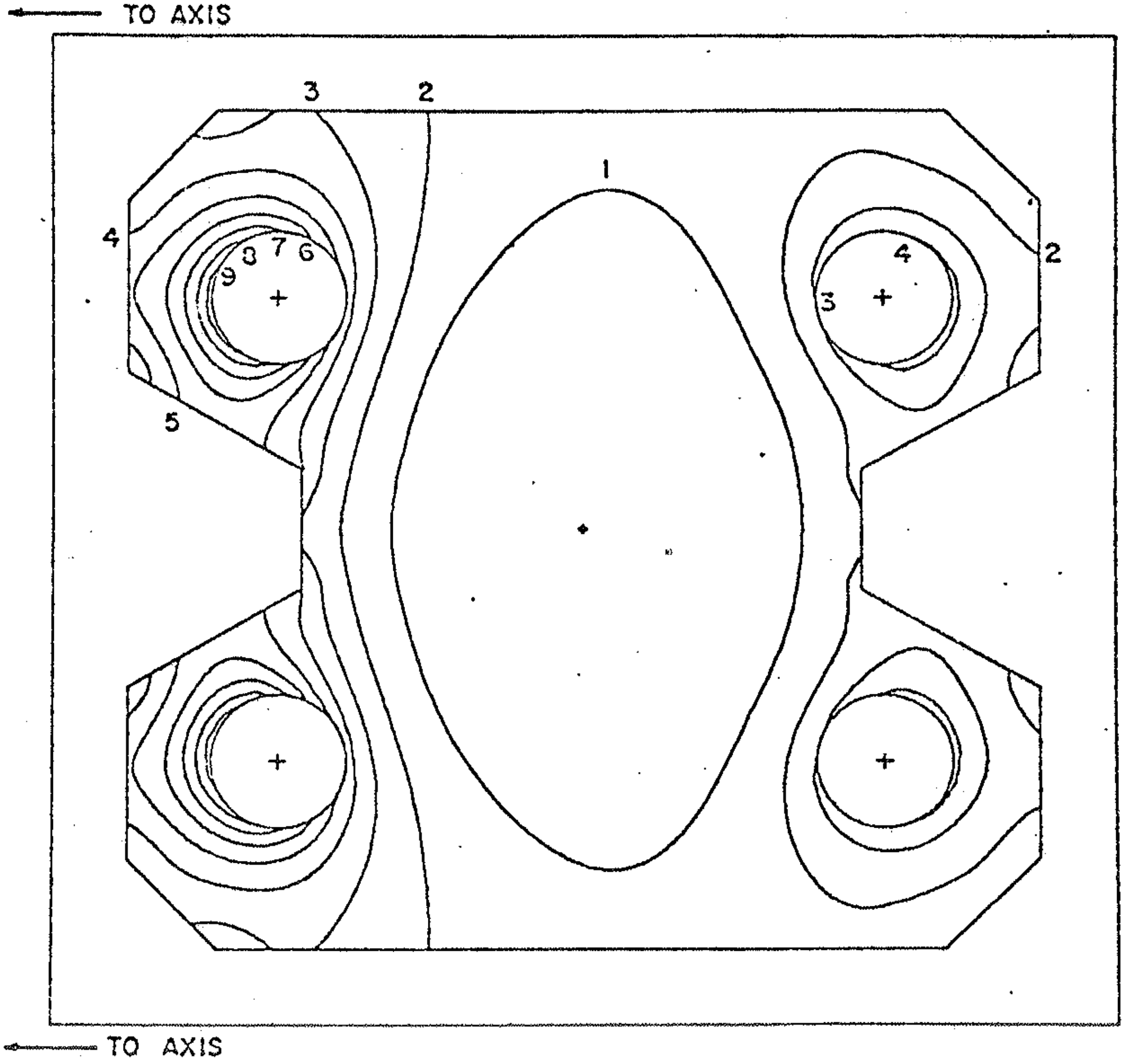

TIME = .025 SEC

of the background gas. Seventy-five percent of the vauum surface is gettered[4]. Most of the ungettered surface is comprised of the bridge regions which are in the getter shine shadow of the rings.

2.2 Plasma Sources

There are presently three coaxial Marshall[5] guns installed on the Octupole. A fast valve puffs in a controlled amount of hydrogen between the concentric gun electrodes. Approximately 300 μsec later a high voltage is applied between the electrodes causing the hydrogen gas to break down and thus creating a plasma. The $\vec{J}\times\vec{B}$ force propels the plasma up towards the machine. Upon encountering the poloidal field the electrons and ions separate and produce a polarization $\vec{E}$ field such that the plasma $\vec{E}\times\vec{B}$ drifts into the center of the machine. Plasma fills the machine, and equilibrium is reached within 400 μsec after injection. Programmable gas puffing is available and is used whenever it is desirable to keep the density constant in time.

2.2.A Intermediate Density Gun

Most of the RF target plasmas, with which the experiments for this thesis were done, were made with the intermediate density gun. Typical initial parameters on the separatrix for an intermediate density gun plasma are:

$$n = 1.5 \times 10^{13} \text{ cm}^{-3}$$

$$T_i \approx T_e = 15\text{-}20 \text{ eV}.$$

The density and temperature decay with ~5 msec e-folding times for a non-RF heated plasma. These parameters are characteristic of a "typical" RF target plasma at high poloidal field (1.25 kG at the RF antenna and 5 kG in the bridge). The target plasma can be varied by changing the gun gas pressure and/or the delay between the gas puff and breakdown.

2.2.B Large Density Guns

There are two nearly identical large density guns also mounted on the Octupole. They work in a manner similar to that of the intermediate density gun. With larger capacitor banks these "big" guns can break down more gas and thus make larger density plasmas, $3\text{-}4\times10^{13}$ cm^{-3}. These guns were used in experiments that explored the high density region of parameter space.

2.3 RF System

The RF source is the third of its kind used for ICRF (Ion Cyclotron Range of Frequencies) heating experiments at the University of Wiconsin Physics department[6,7]. Similar to the previous sources, the RF heating system for this experiment can be divided into three major components, as shown in Fig. 2.4. A pulse-forming network[8] is the power supply for the RF oscillator. It consists of twelve inductively coupled LC sections. A pulse forming network (PFN), or delay line, is the electrical equivalent circuit for a transmission line. The fundamental equations are:

$$T = 2\sqrt{LC}$$

$$Z_o = \sqrt{L/C}$$

where,

$$L = nL_n$$

$$C = nC_n \quad ,$$

n being the number of LC networks and C_n, L_n, being the capacitance and inductance of each section. T is the pulse length, and Z_o the characteristic impedance of the line. For the PFN used in this experiment

Fig. 2.4 Three major components of RF heating system. The center-tapped tank circuit inductor also serves as the antenna.

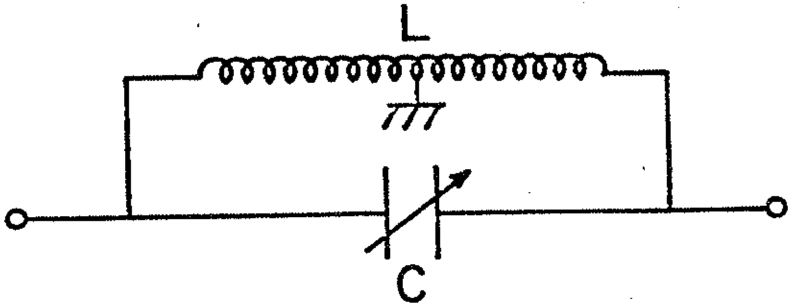

Tank Circuit

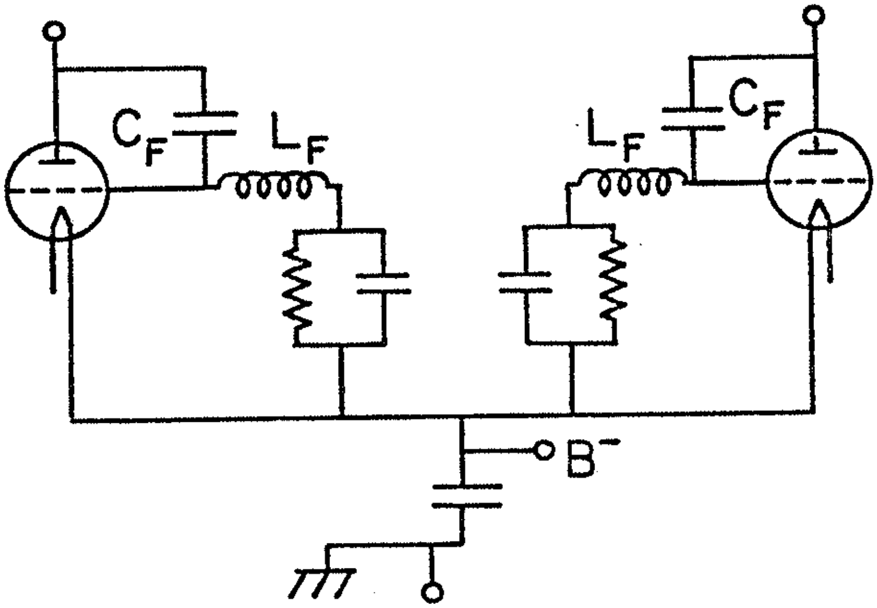

Oscillator

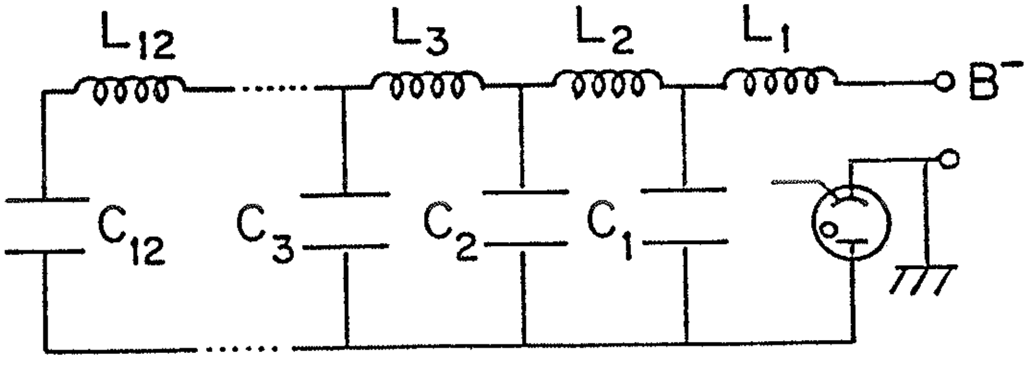

Pulse Forming Network

$$T = 10 \text{ msec}$$

$$Z_o = 100\ \Omega\ .$$

The voltage pulse to a load R_L is $V_oR_L/(Z_o+R_L)$ at a current of $V_o/(Z_o+R_L)$ where V_o is the capacitor charging voltage. A maximum power of $V_o^2/4Z_o$ is delivered to a matched load $R_L=Z_o$. For unmatched loads there are multiple reflections with successively decreasing amplitude. In order to operate in a mode where the oscillator was driven by a single, somewhat constant energy pulse a crowbar ignitron was employed to shunt the oscillator after 10 msec and quickly terminate the RF.

The RF source (Fig. 2.4) is a tuned-plate, tuned-grid, class C, push-pull oscillator. The tubes are operated with tuned grid feedback, and the oscillation frequency (1-3 MHz), is chosen by adjusting the capacitance of the plate tank circuit. The antenna (discussed below) serves as the inductor of the plate tank circuit. Since the high power triode tubes, manufactured by Machlett (Model ML-5682), are not quite identical, each tube is provided with its own grid biasing network. The feedback network provides an RF voltage on the grid of

$$V_g = V_p \frac{\omega^2}{\omega^2-\omega_f^2}$$

where V_p is the RF plate voltage, ω is the operating frequency, $\omega=(LC)^{-.5}$, and ω_f the feedback network resonant frequency, $\omega_f=(L_fC_f)^{-.5}$. For sustained oscillation a 180° phase shift is needed between V_g and V_p which implies $\omega_f>\omega$. Figures 2.5a and 2.5b show idealized PFN waveforms to the oscillator, and Figs. 2.5c and 2.5d show the tube electrode RF voltages and Class C current spikes.

The oscillator is provided with diagnostics to monitor various voltages and currents.

1) A pickup coil near the voltage minimum between the antenna and the machine wall. It is calibrated to read the circulating current in the antenna.
2) A current transformer around one of the transmitting capacitors. As shown in Fig. 2.4, C is actually a number of capacitors in parallel. The current transformer is around one of these and is calibrated to read the total circulating current. Therefore it is a double check on the pickup coil.
3) Resistive voltage dividers that read the RF voltage at the anode of each tube. As a consequence of transmission line effects and the finite inductance leads, the anode voltages are not the same as that on the antenna leads.
4) Current transformers around the leads coming from the anodes. They monitor the total drive current, I_{dt} to

Fig. 2.5 Idealized waveforms for RF system. The PFN delivers a constant voltage (a) and current (b) to the oscillator for 10 msec. Figure (c) shows plate and grid voltages and (d) illustrates Class C current spikes.

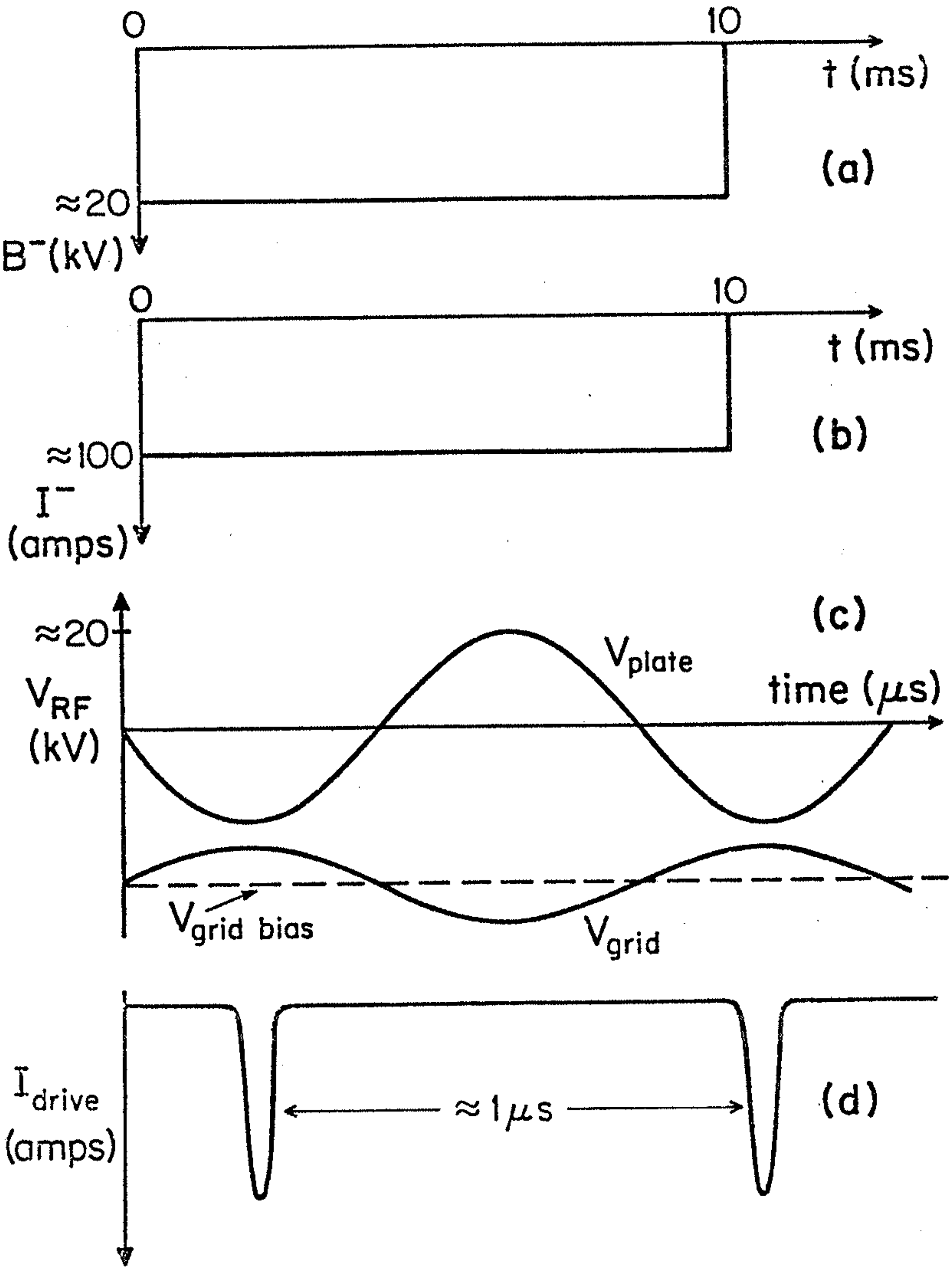
0
10
t (ms)
(a)
≈20
B⁻(kV)
0
10
t (ms)
(b)
≈100
I⁻
(amps)
(c)
≈20
V_plate
time (μs)
V_RF
(kV)
V_grid bias
V_grid
I_drive
(amps)
≈1μs
(d)

the tank circuit and thus display the current spikes that arise with Class C operation.

5) B^- voltage sample monitors the voltage pulse coming out of the pulse forming network. This is a negative going pulse and is applied to the tube filaments.

6) I^- sample monitors the current pulse from the pulse forming network. This is almost the time average of the drive current to the tank current. Some of the I^- current is drawn by the grids for biasing.

The antenna serves as the inductor for the oscillator tank circuit. The antenna is Faraday-shielded with three layers of aluminum strips and is located near the lower lid as shown in Fig. 2.6. It is center fed and grounded at the ends with the return current flowing in the machine floor. The antenna extends one-third of the way around the machine in the toroidal direction so as to produce an inductive electric field which is primarily perpendicular to the purely poloidal octupole magnetic field. The copper antenna sits in a teflon tray with a teflon cover. Grooves are machined into the teflon to increase the path length between the antenna and ground and thus inhibit arcing. The shield strips are arranged so there is no direct line of sight from the plasma to the antenna. This protects the teflon from plasma bombardment and prevents getter shine from coating the teflon cover and shorting the antenna. There are also limiters which help keep the plasma from coming in direct contact with the antenna.

Fig. 2.6 (a) Toroidal cross-section of antenna.

(b) Poloidal cross-section of antenna.

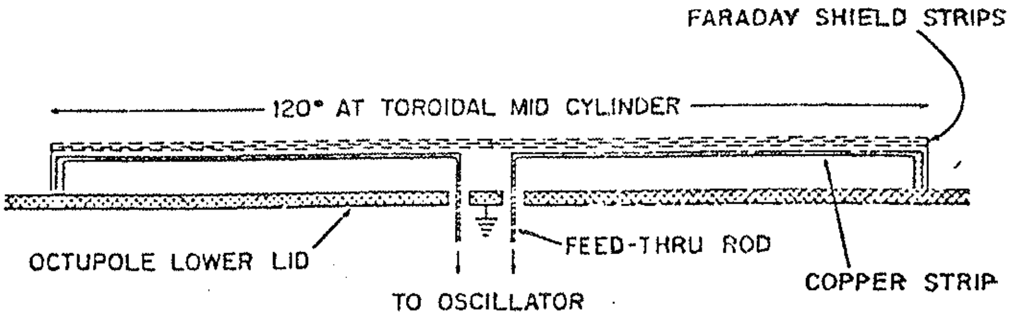
FARADAY SHIELD STRIPS
120° AT TOROIDAL MID CYLINDER
OCTUPOLE LOWER LID
FEED-THRU ROD
COPPER STRIP
TO OSCILLATOR

(a)

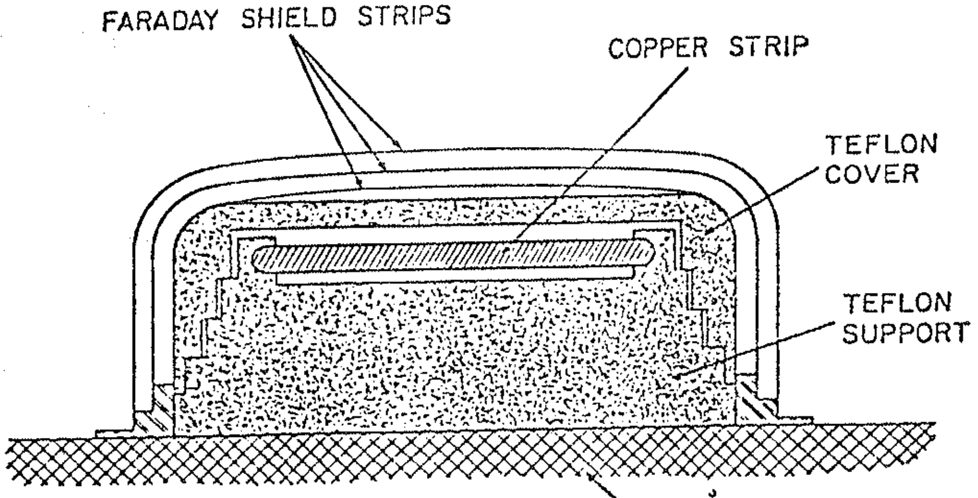
FARADAY SHIELD STRIPS
COPPER STRIP
TEFLON COVER
TEFLON SUPPORT

(b) OCTUPOLE LOWER LID

2.4 Diagnostics

2.4.A Charge Exchange Analyzer

A charge exchange analyzer was the principal diagnostic used to measure the ion temperature. It is a single channel 127° curved plate electrostatic analyzer with a nitrogen stripping cell. A schematic of the charge exchange system is shown in Fig. 2.7. A conceptual description of the analyzing process is first given followed by a more detailed description.

A proton charge exchanges with a neutral in the plasma and enters the analyzer. The fast neutral loses its electron in the nitrogen stripping cell and then is analyzed by a 127° curved plate analyzer[9]. The ion is accelerated to ~20 kV in a Daly detector[10,11] where secondary electrons are produced in proportion to the number of incident ions and independent of ion energy. The electrons then enter a scintillator and finally the photons are detected with a photomultiplier tube. The signal as a function of analyzer acceptance energy is calibrated for the various atomic processes and analyzer bandwidth. The resultant function is an exponential, and T_i is determined by the inverse slope of the data when plotted on a semi-log graph.

Charge exchange cross sections for H^+ on H^o available in the literature[12] are used to calculate the charge exchange rate.

$$R_{c-x} = n_o \sigma_{c-x} v$$

Fig. 2.7 Charge exchange analyzer system.

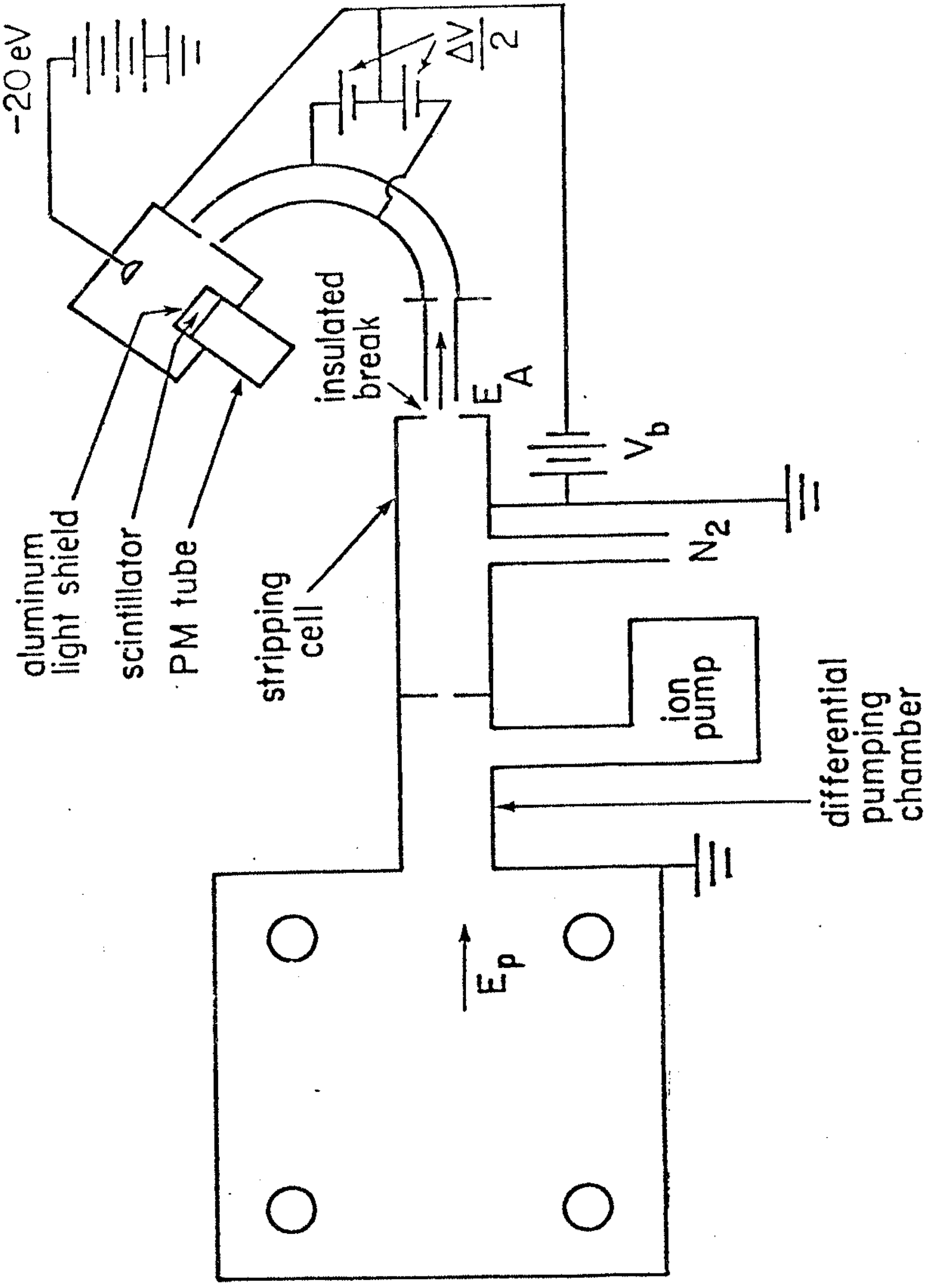
−20 eV
ΔV/2
aluminum light shield
scintillator
PM tube
insulated break
E A
V b
stripping cell
N2
ion pump
differential pumping chamber
E p

where n_o is the neutral density and v is the ion speed. Charge exchange cross sections on H_2 are smaller by over an order of magnitude from that on H^o over most of the energy range for which the ion distribution is measured. A good approximation up to 2 keV for the charge exchange cross section is[13]

$$\sigma_{c-x} \simeq 6.8\ 10^{-15}\ E^{-1/6}(\mathrm{eV})\ \mathrm{cm}^2 \quad .$$

The neutral upon leaving the plasma enters the charge exchange analyzer and encounters a nitrogen stripping cell where it has some probability of losing its electron.

$$H^o + N_2^o \rightarrow H^+ + N_2^-$$

Unfortunately, unlike the charge exchange cross section, the nitrogen stripping efficiency has a strong energy dependence[14] and is not well known below 150 eV. This uncertainty prevents the charge exchange analyzer from measuring the ion distribution function below 150 eV. Therefore it is the tail that is being observed for temperatures below this lower limit. The curved plate analyzer has a bandwidth ΔE, proportional to the ion energy E that it is accepting. In order to take advantage of this, the stripping cell is biased positive, usually to 200 V, to increase the analyzer bandwidth. The high pressures needed for the stripping cell, ~0.01 torr, are measured with a fast ion gauge[15].

The curved plates accept protons that satisfy:

$$\frac{e\Delta V}{\Delta R} = \frac{mv^2}{R} = \frac{2E_A}{R}$$

$$E_A = \frac{e\Delta V}{2} \frac{R}{\Delta R} \quad .$$

where ΔV is potential difference between the curved plates, E_A the ion energy (including post-acceleration by the stripping cell) in the analyzer, ΔR the plate separation and R is the radius of the center line.

The analyzer can be run in one of two modes. In the d.c. mode the curved plates acceptance energy is kept constant during the shot, and the distribution function is measured by varying the curved plate voltage from shot to shot. In the swept mode the distribution function is measured in a single shot by sweeping the curved plate voltage in a time short compared to times for variations of the ion temperature. The analyzer can be swept several times during the shot to get the ion temperature time dependence.

The signal from the PM tube is,

$$S(E) \propto \sigma_{c-x}(E) v \delta E_A \eta(E) f(E) n_o n_i$$

where E and v are the energy and speed of the ion in the plasma, $\eta(E)$ is the stripping efficiency, and E_A is the energy of the ion in the analyzer which includes the post-acceleration energy. The analyzer bandwidth δE_A is proportional to E_A and, for a Maxwellian

$$f(E) \propto E^{1/2}\, e^{-E/kT} \quad .$$

To obtain the temperature we plot on semilog paper

$$n_o n_i \frac{f(E)}{E^{1/2}} \propto \frac{S(E)}{\sigma_{c-x}(E) E^{1/2} E_A \eta(E)} \propto e^{-E/kT}$$

and the inverse slope gives the temperature.

For most RF heated plasmas there is a two component Maxwellian as illustrated in Fig. 2.8. It is usually necessary to extrapolate the hot component distribution back to lower energies and subtract it from the lower energy signal to more accurately analyze the cold component distribution. The fitted lines for each component can be written as,

$$g_h(E) \propto n_{oh} n_{ih} T_h^{-3/2}\, e^{-E/kT_h}$$

$$g_c(E) \propto n_{oc} n_{ic} T_c^{-3/2}\, e^{-E/kT_c}$$

Fig. 2.8 Typical two component Maxwellian ion energy distribution as measured by charge exchange analyzer.

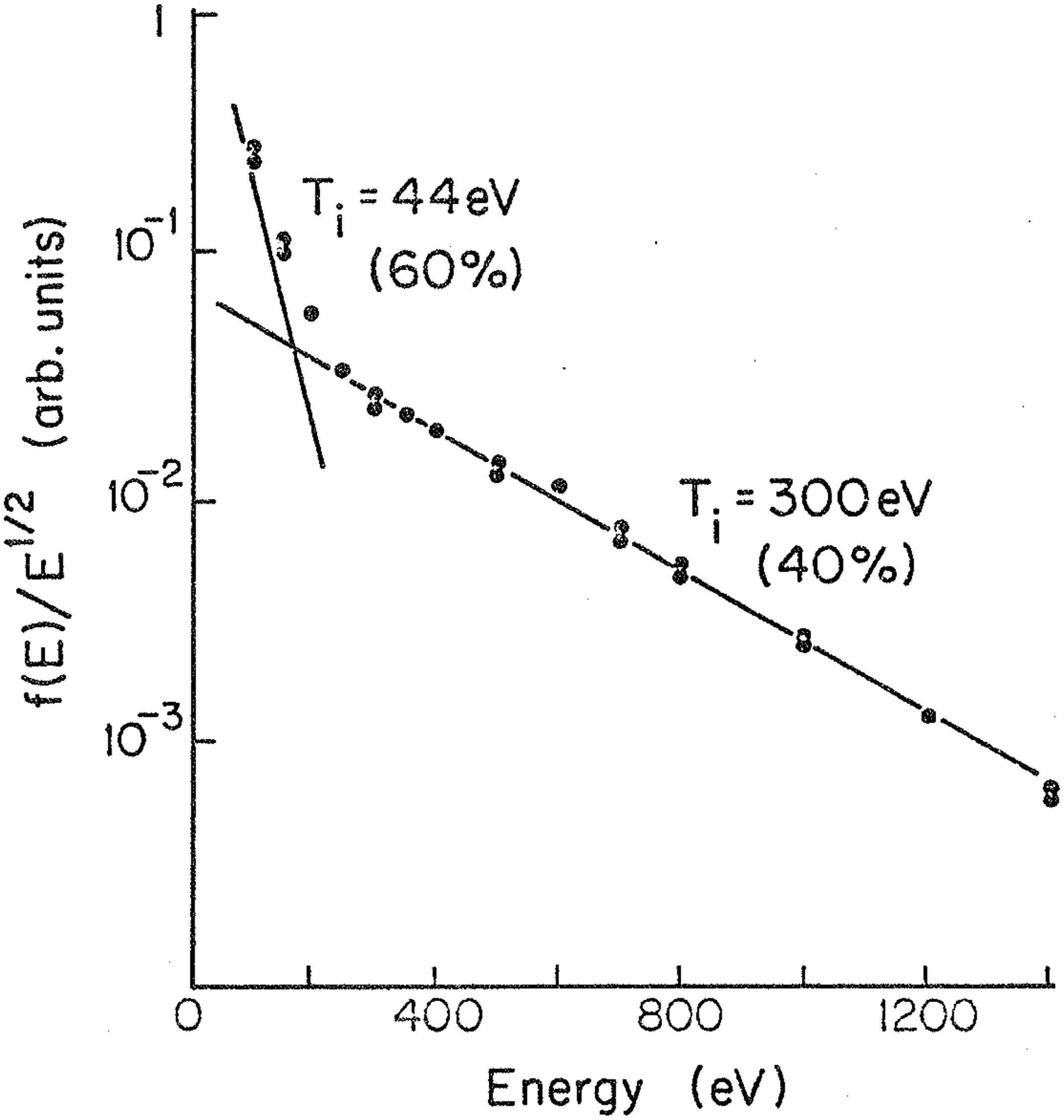
1
10^{-1}
10^{-2}
10^{-3}
$f(E)/E^{1/2}$ (arb. units)
$T_i = 44$ eV
(60%)
$T_i = 300$ eV
(40%)
0
400
800
1200
Energy (eV)

If we assume that $n_{oh} \approx n_{oc}$, that is the two components come from the same place inside the plasma, then,

$$\frac{n_{ih}}{n_{ic}} = \frac{g_h(0)T_h^{3/2}}{g_c(0)T_c^{3/2}} \quad .$$

Since everything on the right-hand side is known, this expression determines the relative population of the two components.

2.4.B RF Electric Field Probe

Figure 2.9 shows the probe used to map the RF toroidal electric field structure. The probe is rotated so the tip is aligned in the toroidal direction, perpendicular to $\vec{B}_o$. Integrating curl $\vec{E}$ over the area of the loop yields

$$V = \int \vec{\nabla} \times \vec{E} \cdot d\vec{A} = \int \vec{E} \cdot d\vec{\ell} = Ew = -\dot{\Phi}$$

where E is the toroidal field strength at the tip of the probe. There is no contribution to the line integral along the long sides of the loop since there $\vec{E}$ toroidal is perpendicular to $d\vec{\ell}$ or at the top where the probe is in the machine wall or outside the vacuum and $\vec{E}$ is negligibly small. Any vertical electric field gives equal and opposite contributions along the long sides of the probe. Therefore the signal from the probe is directly proportional to the electric field at the tip and is independent of any gradients. Since $\vec{E}$ is

Fig. 2.9 Magnetic probe used to measure RF toroidal electric field.

Electric Field Probe

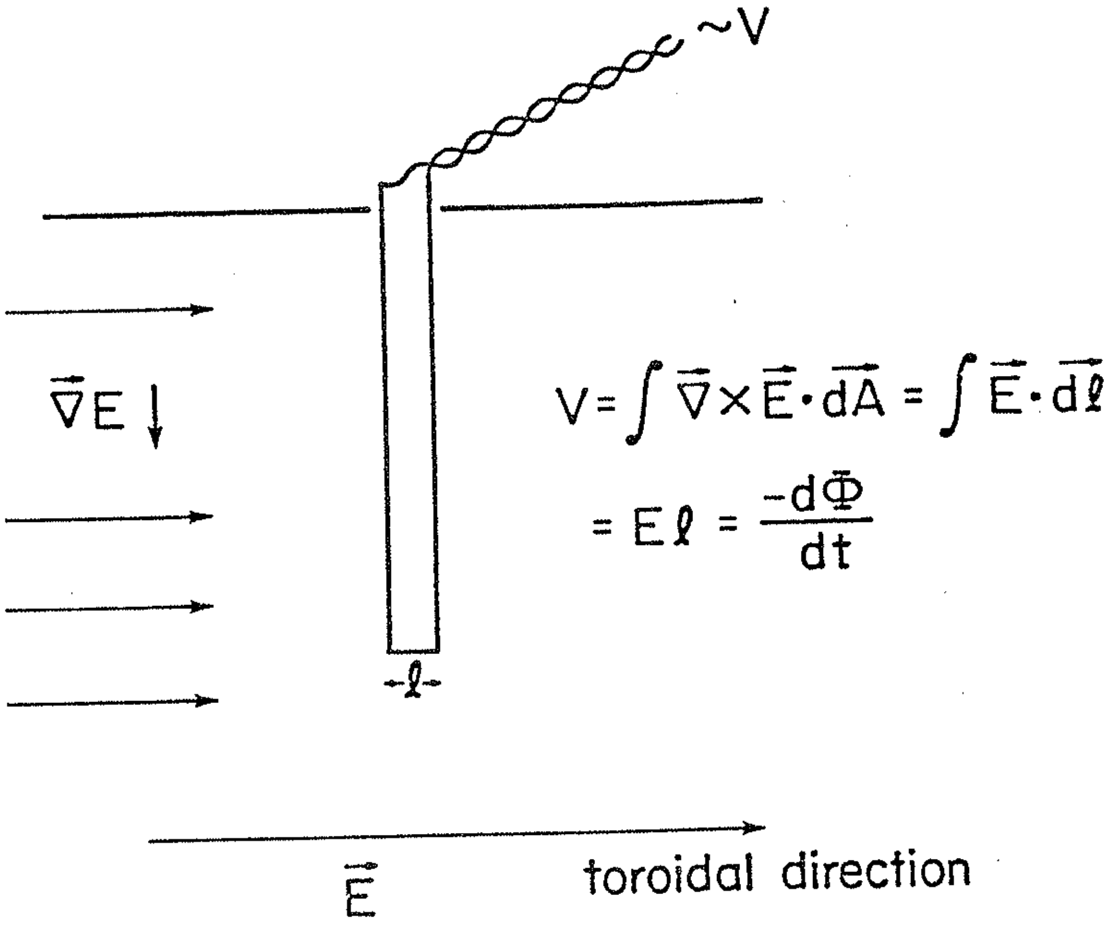

toroidal, the probe can be swiveled in a poloidal plane to measure the electric field off the midcylinder. Note that, although the signal is proportional $-\dot{\Phi}$, it is unlike a conventional magnetic probe (Fig. 2.10) which cannot be related in a simple manner to the local electric field. From Fig. 2.10

$$V = \int \vec{E} \cdot d\vec{\ell} = (E_2 - E_1)w = -\dot{\Phi}$$

The probe consists of four turns with a grounded center tap, and the signal is detected differentially. The quality of construction is tested by measuring how well the signal nulls when the probe is rotated 90°.

2.4.C Gridded Ion Energy Analyzer

An electrostatic gridded energy analyzer was used to measure local ion temperatures. Figure 2.11 illustrates how the grids are biased. The front grid is not externally biased and thus is at the floating potential. It is a low transparency grid to limit the ion flux into the probe. Next is the discriminator grid which is biased to some positive potential with respect to ground. It passes ions whose energy satisfy the equation,

$$E + eV_p > eV_d$$

where E is the ion energy, V_p the plasma potential, and V_d the discriminator voltage. All ions that make it through the

Fig. 2.10 Conventional magnetic probe.

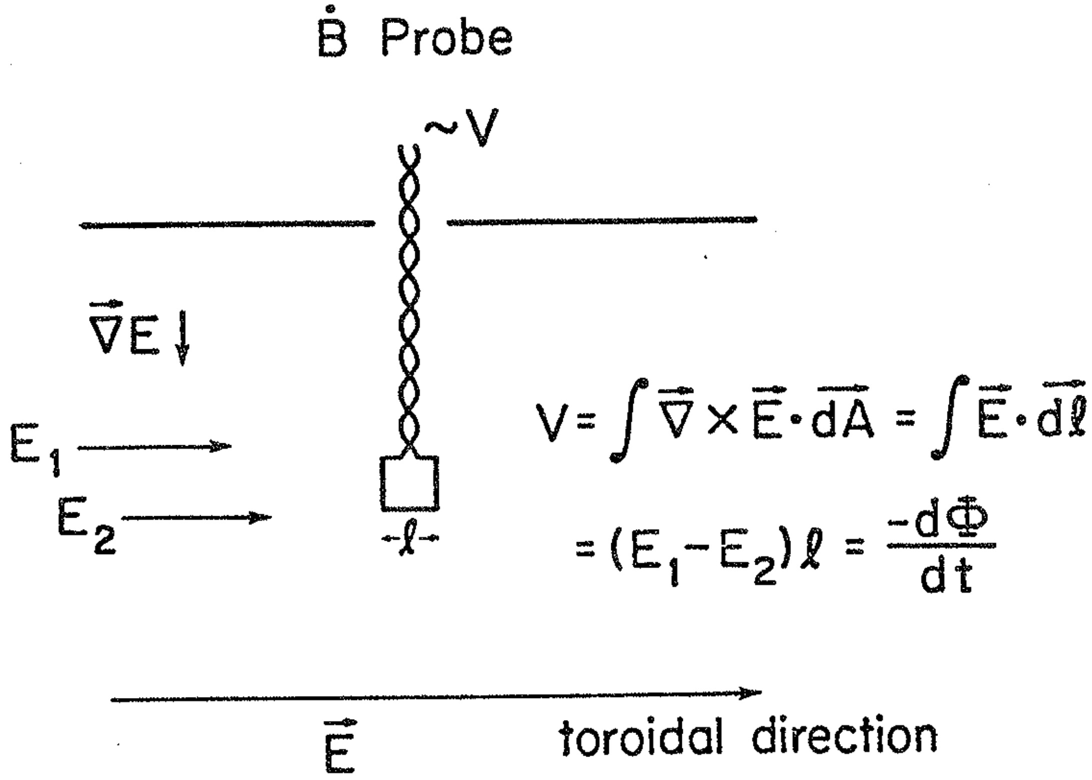
$\dot{B}$ Probe
~V
$\vec{\nabla}E$
E_1
E_2
ℓ
$V = \int \vec{\nabla} \times \vec{E} \cdot \vec{dA} = \int \vec{E} \cdot \vec{d\ell}$
$= (E_1 - E_2)\ell = \frac{-d\Phi}{dt}$
$\vec{E}$
toroidal direction

Fig. 2.11 Relative biasing potentials of the grids that constitute the electrostatic gridded ion energy analyzer.

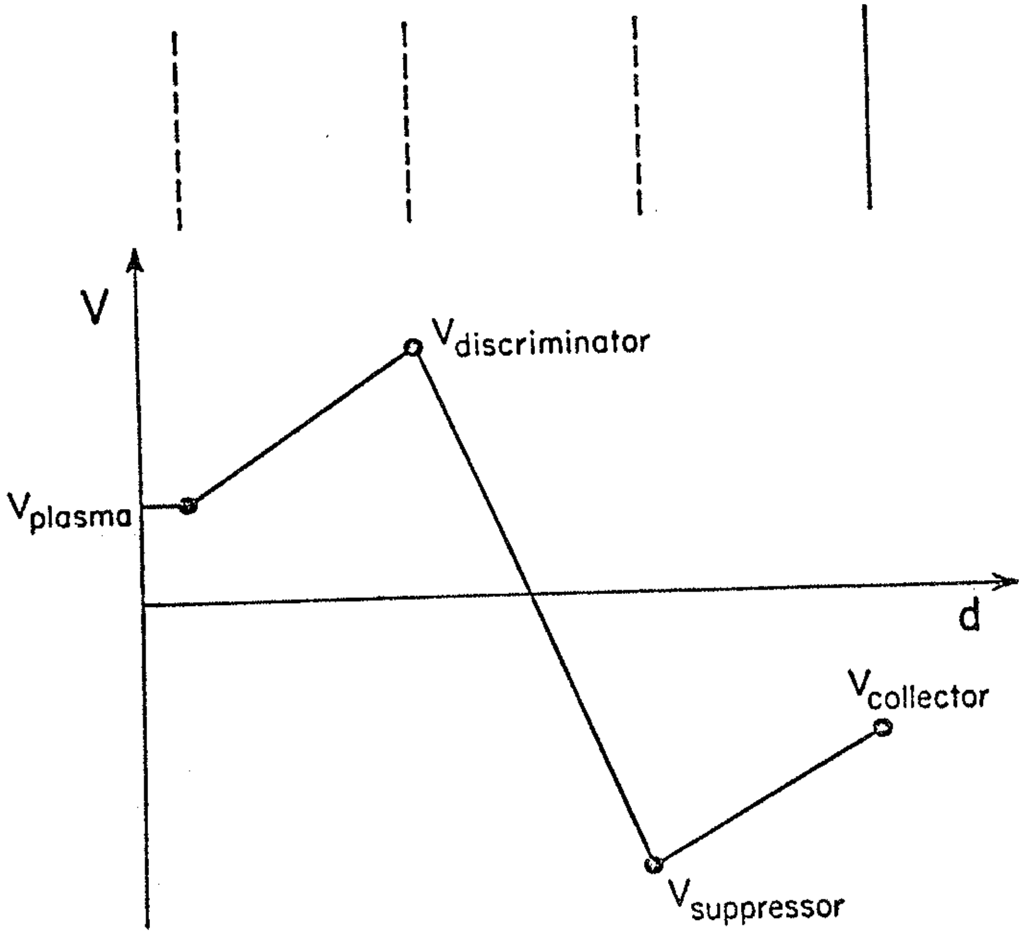
V
$V_{discriminator}$
V_{plasma}
d
$V_{collector}$
$V_{suppressor}$

discriminator are collected by the negatively biased collector grid. The suppressor grid eliminates collector current from secondary electrons emitted by the collector due to ion impact.

The current collected by the collector for a given discriminator voltage, $V_d > V_p$ is,

$$I(eV_d) \propto \int_{e(V_d-V_p)}^{\infty} (E-eV_p)^{1/2}\ f(E-eV_p)dE$$

$$\propto \int_{E_d'}^{\infty} E'^{1/2} e^{-E'/kT}\ dE' \propto e^{-E_d'/kT}$$

where $E_d' = e(V_d - V_p)$ and $E' = E - eV_p$. The collector current is plotted as a function of discriminator voltage, yielding an exponential curve with an e-folding energy of kT_i. For discriminator voltages less than the plasma potential, all the ions are collected. Figure 2.12 shows a graph of the collector signal versus discriminator energy with a computer fit to the exponential. The knee in the curve is the plasma potential.

As with the charge exchange analyzer, the probe can be operated in either a d.c. or swept mode and is subject to the same restrictions. The probe can be oriented in two directions with respect to the magnetic field to read either the "perpendicular" or "parallel" ion temperature.

Fig. 2.12 Typical data from electrostatic gridded ion energy analyzer with fitted slope used to determine the ion temperature.

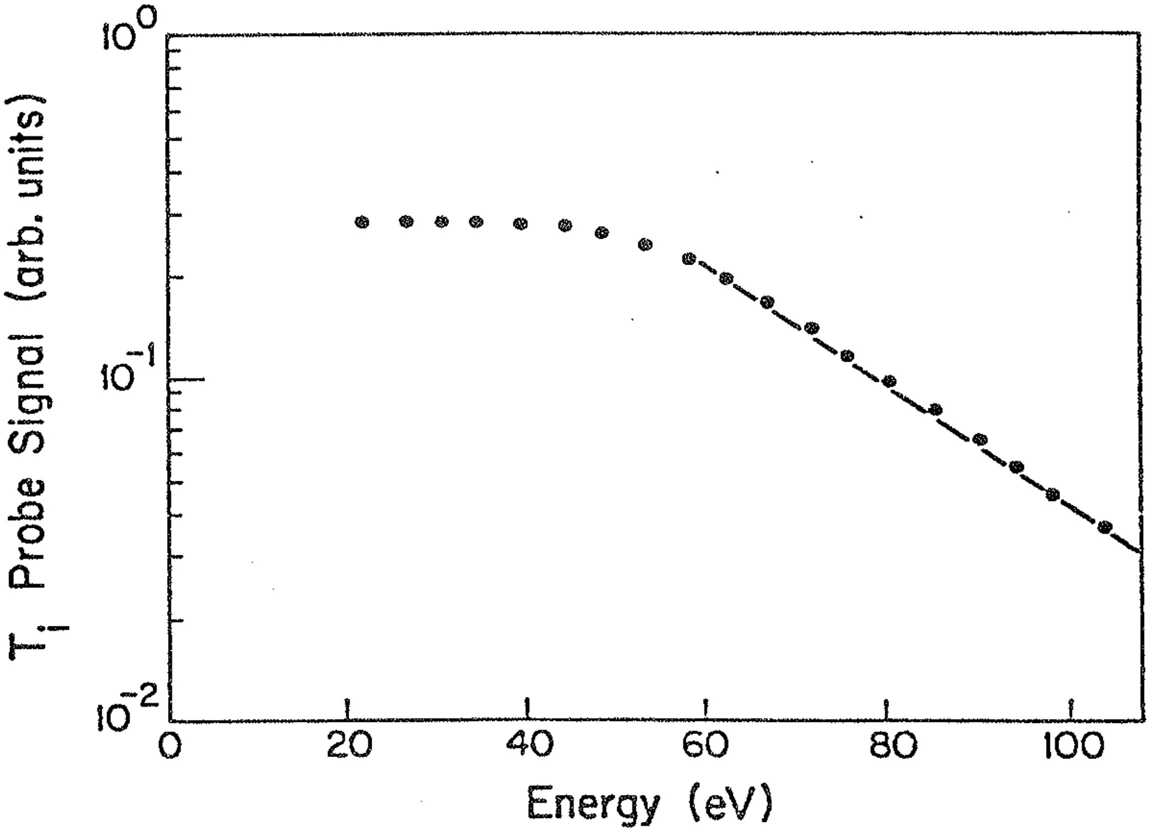
10^0
10^{-1}
10^{-2}
0
20
40
60
80
100
Energy (eV)
T_1 Probe Signal (arb. units)

2.4.D Langmuir Probes

Langmuir probes[16] were used extensively to measure the electron temperature and, to a lesser extent, to get an indication of the plasma density profile. The probes consist of platinum electrodes supported by bored ceramic. The idealized I-V trace for a single Langmuir probe is shown in Fig. 2.13. The response in the transition region is given by

$$I(V) = I_{oe}\, e^{(e(V-V_p)/kT_e)} - I_{oi}$$

where I_{oe} and I_{oi} are the electron and ion saturation currents and are given by,

$$I_{oe} = \frac{1}{2}\, neA\left(\frac{2kT_e}{\pi m}\right)^{1/2}$$

$$I_{oi} = \frac{1}{2}\, neA\left(\frac{2kT^*}{\pi M}\right)^{1/2}$$

A is the probe area, n the density, and T* the hotter of the electron and ion temperatures.

Since there is no electric field between the plasma and the probe when the probe is at the plasma potential, the electron saturation current is determined by the random electron flux to the probe. The factor of $\left(\frac{2kT_e}{\pi m}\right)^{1/2}$ represents the average velocity of the electrons in a single direction, from the plasma toward the

Fig. 2.13 Idealized I-V trace for a single tipped Langmuir probe.

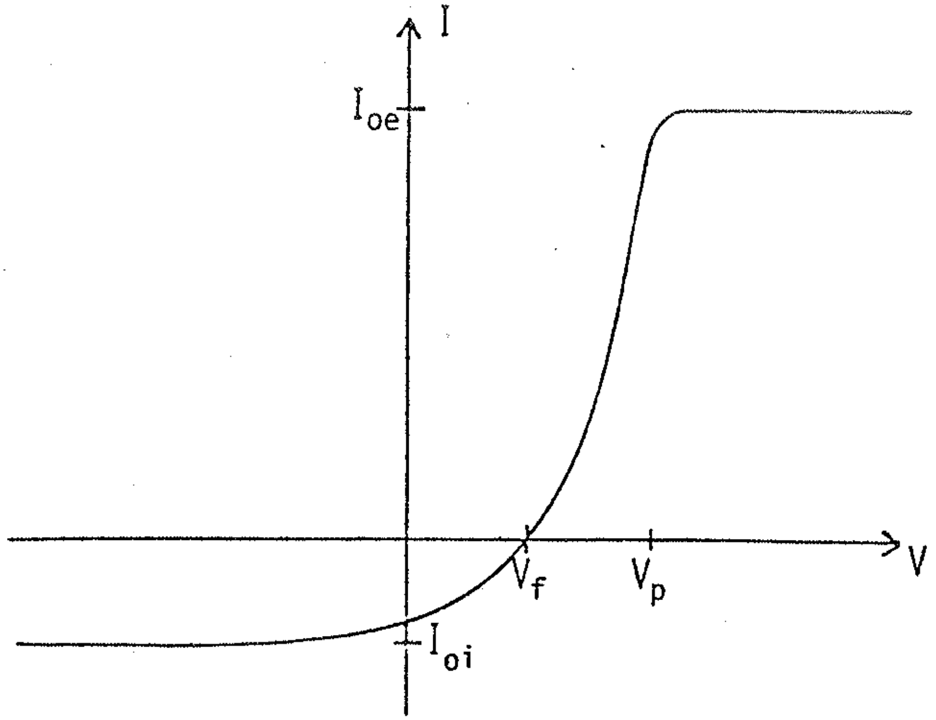
I
I_{oe}
V_f
V_p
V
I_{oi}

probe. The factor of $\frac{1}{2}$ comes from the fact that at the sheath-plasma boundary the density is half as great as what it is in the plasma.

The equation for ion saturation current is somewhat more complicated in the case of $T_i<T_e$ due to the Bohm sheath criterion[16,17]. This requires that the ions have a minimum velocity $v_o>(\frac{kT_e}{m_i})^{1/2}$ upon entering the sheath. Under that condition the ion density is larger than the electron density in the sheath so as to be consistent with the fact that the probe is repelling electrons. In order to satisfy the condition a "pre-sheath" is formed to accelerate the ions to the critical speed. For $T_i>T_e$ there is no problem in satisfying the criterion, and the expression for the ion saturation current is analogous to that for the electrons.

An admittance probe, developed by Sprott[18], was used to measure the electron temperature. The plasma sheath impedance is across one leg of a capacitance bridge. The bridge is driven by a low voltage (~1V) sine wave (~400 kHz). The bridge is balanced without plasma, and the signal during the shot is proportional to the sheath admittance. The probe is calibrated using external resistors. Since the sheath admittance[19] is

$$Y=\frac{1}{R}=\frac{dI}{dV}\bigg|_{V_f}=\frac{eI_{oi}}{kT_e} ,$$

the electron temperature is obtained from

$$\frac{kT_e}{e} = I_{oi}R \quad .$$

Two tips on a triple probe measure the ion saturation current, and the third tip measures the admittance. The admittance probe is similar to the double probe method of measuring T_e in that it involves measuring the slope of the I-V curve at the floating potential and the ion saturation current.

2.4.E Interferometer

A 70 GHz microwave digital multiradian fringe shift interferometer[20,21] measures the separatrix density. The change in phase shift between the plasma signal and a reference signal is measured with a phase locked loop and is proportional to changes in the density. The system is absolutely calibrated such that the time dependent density is displayed on an oscilloscope.

2.4.F Optical Diagnostics

There is an array of spectroscopic diagnostics mounted on the Octupole. At one port on the lower lid, four light pipes with optical filters and PM tubes measure the intensity of CIII, NIII, OIII, and H-beta transition lines. On the upper lid viewing the midcylinder, there is a vacuum ultraviolet monochromator. A bolometer that measures the time integrated incident energy[22] is used to indicate radiated power.

REFERENCES - CHAPTER 2

1. T. Ohkawa and D.W. Kerst, Phys. Rev. Lett. 7, 41 (1961).
2. H.K. Forsen, D.W. Kerst, R.A. Breun, A.J. Cavallo, J.R. Drake, J.C. Sprott in Fourth European Conference on Controlled Fusion and Plasma Physics (CNEN, Rome, 1970), p. 24.
3. See University of Wisconsin Ph.D. Theses by J.R. Drake (1973), J.W. Rudmin (1974), R.A. Breun (1975), A.J. Cavallo (1975), G.A. Navratil (1976), C.J. Armentrout (1977), E.J. Strait (1979).
4. H.R. Garner, University of Wisconsin PLP 834 (1980).
5. J. Marshall, Phys. Fluids 3, 134 (1960).
6. J.D. Barter, Ph.D. Thesis, University of Wisconsin (1976).
7. A.P. Biddle, Ph.D. Thesis, University of Wisconsin (1980).
8. C.M. Fortgang, University of Wisconsin PLP 826 (1980).
9. H.P. Eubank and T.P. Wilkerson, Rev. of Sci. Intstr. 34, 12 (1963).
10. N.R. Daley, Rev. of Sci. Instr. 31, 720 (1960).
11. N.R. Daley, Rev. of Sci. Instr. 31, 264 (1960).
12. R.L. Freeman and E.M. Jones, Culham Laboratory Report CLM-R-137 (1974).
13. E.J. Strait, University of Wisconsin PLP 592 (1982).
14. C.F. Barnett and J.A. Ray, Nuclear Fusion 12, 65 (1972).
15. G.J. Schulz and A.V. Phelps, Rev. of Sci. Instr. 28, 1051 (1957).
16. F.F. Chen in Plasma Diagnostic Techniques, R.H. Huddlestone and S.L. Leonard, eds., (Academic Press, N.Y., 1965), Chap. 4.
17. D. Bohm in The Characteristics of Electrical Discharges in Magnetic Fields, A. Guthrie and R.K. Wakerling, eds., (McGraw-Hill, N.Y., 1949), Chap. 3.

18. J.C. Sprott, Rev. of Sci. Instr. 39, 1569 (1968).

19. J.C. Sprott, University of Wisconsin PLP 74 (1966).

20. H.R. Garner, University of Wisconsin PLP 833 (1980).

21. C.M. Fortgang, University of Wisconsin PLP 861 (1981).

22. J. Twichell, private communication.

CHAPTER 3

ACCESSIBILITY, POLARIZATION, AND DAMPING

3.1 Introduction

The heating of ions requires the presence of a left-hand circularly polarized component to the RF electric field at a region in the plasma where the local ion gyrofrequency matches the frequency of the RF. We start by considering cold plasma theory as formulated by Stix[1]. We will be using the standard slab coordinate system to model the plasma in the region near the antenna. The magnetic field lines lie in the z-direction (major radius), any gradients lie in the x-direction (vertical) and everything is assumed symmetric in the y-direction (toroidal), as shown in Fig. 3.1. We define z=0 at the midcylinder and x=0 at the antenna. Note that for the Octupole the density and magnetic field gradients point in opposite directions on the midcylinder. From cold plasma theory we will calculate a dispersion relation, $k_x=k_x(k_z, \omega, \omega_{ci}, \omega_{pi})$, and electric field polarization. As we shall see, cold plasma theory predicts that the left-hand component of the RF electric field (E^+) is identically zero at $\omega=\omega_{ci}$, independent of density and k_z. A better calculation is then done using the lowest order warm plasma effects and folding in the k_z spectrum of the antenna. This calculation predicts a finite E^+ at $\omega=\omega_{ci}$ for a given temperature

Fig. 3.1 Coordinate system used for theoretical slab model. The antenna and vacuum electric field lie in the $\hat{y}$-direction.

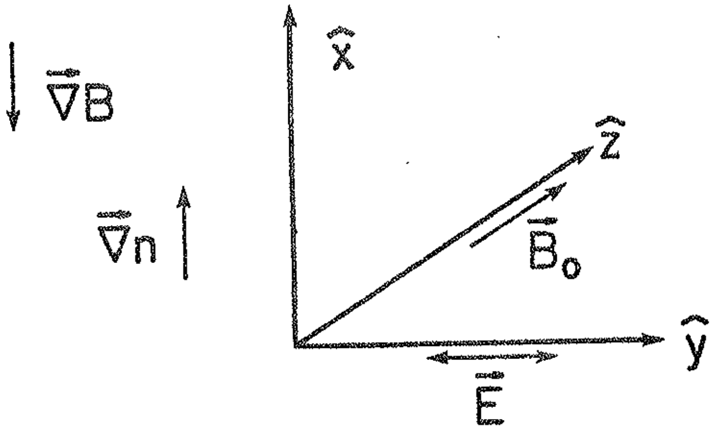
$\vec{\nabla}B$
$\vec{\nabla}n$
$\hat{x}$
$\hat{z}$
$\vec{B}_o$
$\hat{y}$
$\vec{E}$

and density. Using this value of E^+, the plasma loading is predicted using a damping model developed by Sprott[2] and Barter[3]. Accessibility is examined using the slab approximation and solving a differential equation for E_y

$$\frac{\partial^2}{\partial x^2} E_y + c(x)E_y = 0 \quad . \tag{3.1}$$

3.2 <u>Homogeneous Cold Plasma Theory</u>

Using the notation of Stix we start by writing down the cold plasma dielectric tensor

$$\overleftrightarrow{K} \cdot \vec{E} = \begin{pmatrix} S & -iD & 0 \\ iD & S & 0 \\ 0 & 0 & P \end{pmatrix} \begin{pmatrix} E_x \\ E_y \\ E_z \end{pmatrix} \tag{3.2}$$

where

$$S = \frac{1}{2}(R+L) \qquad D = \frac{1}{2}(R-L)$$

$$R = 1 - \sum_\alpha \frac{\omega_{p\alpha}^2}{\omega^2}\left(\frac{\omega}{\omega+\omega_{c\alpha}}\right)$$

$$L = 1 - \sum_{\alpha} \frac{\omega_{p\alpha}^{2}}{\omega^{2}}\left(\frac{\omega}{\omega-\omega_{c\alpha}}\right) \tag{3.3}$$

$$P = 1 - \sum_{\alpha} \frac{\omega_{p\alpha}^{2}}{\omega^{2}}$$

$$\omega_{p\alpha} = \frac{4\pi n_{\alpha} e^{2}}{m_{\alpha}}$$

$$\omega_{c\alpha} = \frac{qB_{o}}{m_{\alpha} c}$$

where α indicates particle species.

In this analysis we assume the first order linear perturbations vary as exp $i(\vec{k}\cdot\vec{r}-\omega t)$. The plasma satisfies Maxwell´s equations

$$\vec{\nabla} \times \vec{E} = -\frac{1}{c}\frac{\partial \vec{B}}{\partial t}$$

$$\vec{\nabla} \times \vec{B} = \frac{1}{c}\overleftrightarrow{K} \cdot \frac{\partial \vec{E}}{\partial t} \qquad (3.4)$$

which combine to give,

$$-\nabla^2\vec{E} + \vec{\nabla}(\vec{\nabla}\cdot\vec{E}) - k_o^2\overleftrightarrow{K} \cdot \vec{E} = 0 \qquad (3.5)$$

or,

$$\begin{pmatrix} S - n^2\cos^2\theta & -iD & n^2\cos\theta\sin\theta \\ iD & S-n^2 & 0 \\ n^2\cos\theta\sin\theta & 0 & P - n^2\sin^2\theta \end{pmatrix} \begin{pmatrix} E_x \\ E_y \\ E_z \end{pmatrix} = 0 \qquad (3.6)$$

where we have defined,

$$n^2 = \frac{k^2c^2}{\omega^2} = \frac{k^2}{k_0^2}$$

$$k_x = k\sin\theta$$

$$k_z = k \cos\theta$$

and θ is the angle between $\vec{k}$ and the magnetic field ($\hat{z}$). Equation (3.6) is valid for all the frequency regimes. In the ion cyclotron range of frequencies (ICRF) we make the low-frequency high-conductivity approximation as Stix[4] did that $|E_z| << |E_x|$, and $|E_z| << |E_y|$. This allows us to rewrite Eq. (3.6) as,

$$\begin{pmatrix} k_z^2 - Sk_o^2 & +iDk_o^2 \\ -iDk_o^2 & k^2 - Sk_o^2 \end{pmatrix} \begin{pmatrix} E_x \\ E_y \end{pmatrix} = 0 \qquad (3.7)$$

where for the ICRF

$$S = \frac{\omega_{pi}^2}{\omega_{ci}^2 - \omega^2}$$

$$(3.8)$$

$$D = - \frac{\omega_{pi}^2 \omega}{\omega_{ci}(\omega_{ci}^2 - \omega^2)} \quad .$$

Note that the role played by the electrons is important and that they are included in the summations of Eq. (3.3) which in the ICRF yield Eqs. (3.8). Setting the determinant of Eq. (3.7) equal to zero and dropping the ion subscript yields the dispersion relation,

$$k_x^2c^2 = \frac{\omega^4\gamma^2\omega_c^2-\omega^2(2\gamma\omega_c^2k_z^2c^2+k_z^4c^4)+\omega_c^2k_z^4c^4}{\omega^2(\gamma\omega_c^2+k_z^2c^2)-\omega_c^2k_z^2c^2} \tag{3.9}$$

where,

$$\gamma = \omega_p^2/\omega_c^2 \quad .$$

The polarization is given by the first line in Eq. (3.7),

$$P = \frac{iE_x}{E_y} = \frac{-Dk_o^2}{Sk_o^2-k_z^2} \tag{3.10}$$

where P=+1 for right circular polarization (RCP), −1 for left circular polarization (LCP), and 0 or ±∞ linear polarization. The singularities in k_x^2 and E_x are one and the same and occur for

$$Sk_o^2 = k_z^2 \tag{3.11}$$

The two roots to Eq. (3.9) are plotted for a particular set of parameters in Fig. 3.2. The two roots correspond to the fast and slow or ion cyclotron waves. They can be identified by their relative phase velocities for a given k_x or their polarization at

Fig. 3.2 Cold plasma dispersion relation: $|\vec{B}|=1.2$ kG, $\omega/\omega_{ci}=0.66$, $n=5.0\times10^{12}$ cm^{-3}.

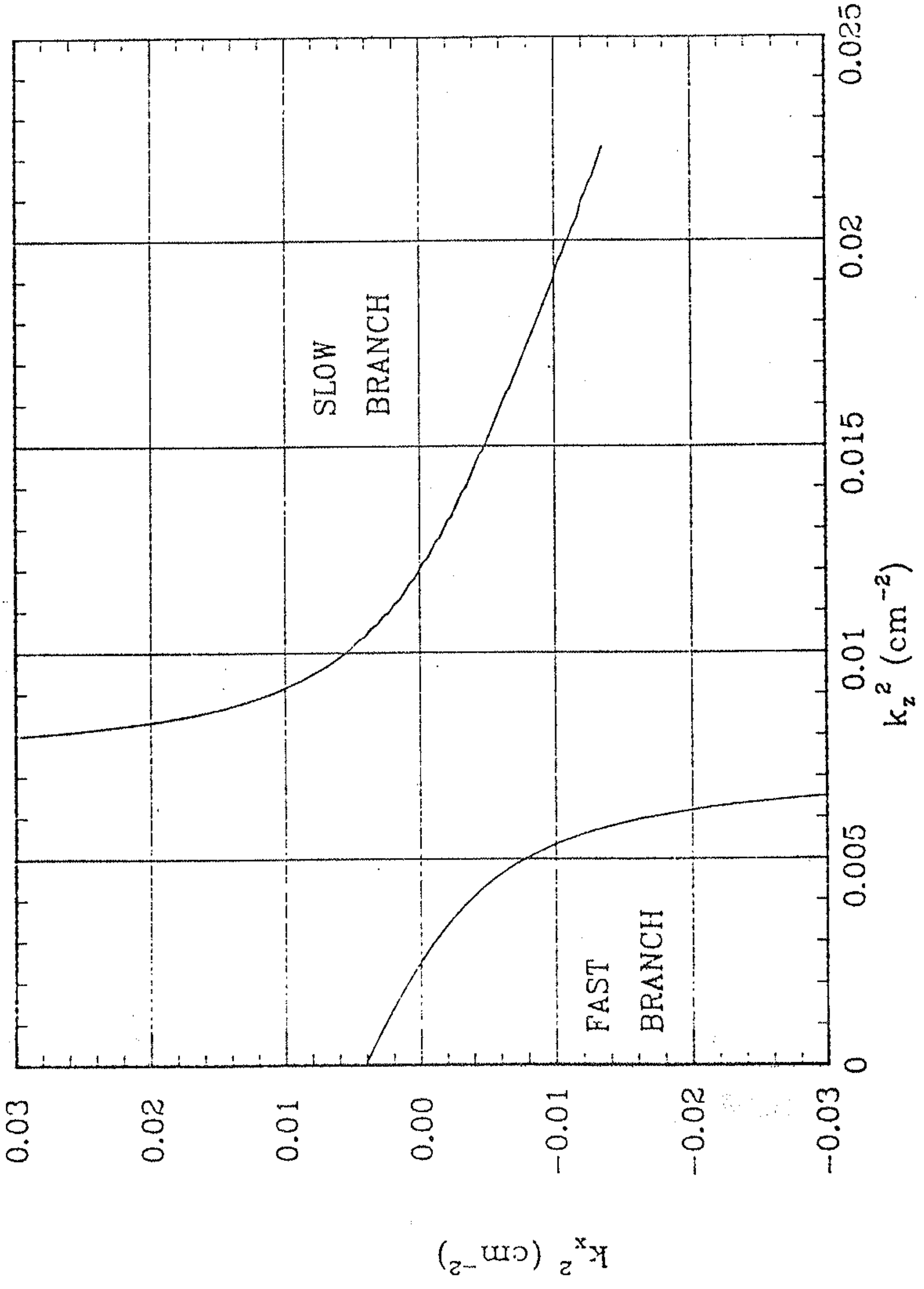
SLOW BRANCH
FAST BRANCH
k_z^2 (cm^{-2})
k_x^2 (cm^{-2})
0
0.005
0.01
0.015
0.02
0.025
0.03
0.02
0.01
0.00
−0.01
−0.02
−0.03

k_x=0. Figure 3.3 is a plot of the polarization wherever $k_x^2>0$. Note that the fast wave is purely RCP and the slow wave purely LCP for k_x=0. These points correspond to the usual normal modes of propagation along a field line. The point at which k_x^2 gets large is referred to by Stix[1] as the perpendicular ion cyclotron resonance.

We can examine some important polarization effects by writing P in the following form:

$$P = \frac{iE_x}{E_y} = \frac{\omega}{\omega_c} \frac{1}{\left(1 + \frac{k_z^2 c^2}{\omega_p^2}\left(1 - \frac{\omega_c^2}{\omega^2}\right)\right)} \qquad (3.12)$$

For $\omega=\omega_c$, P=1, and the electric field is right circularly polarized for all values of ω_p and k_z. (All values of ω_p are not strictly correct since implicit in the ICRF approximations is that $\omega_p \gg \omega$ which for our plasmas is well satisfied down to densities of 10^{10} cm^{-3}.) Since the heating of ions depends on the presence of a LCP component to the RF electric field at the ion cyclotron resonance zone, the cold plasma model would predict zero heating. A second observation about Eq. (3.12) is that for high field incidence, which for the Octupole experiment corresponds to the resonance zone crossing the midcylinder above the antenna, the perpendicular ion cyclotron resonance will always occur somewhere between the antenna and the mod-B surface where $\omega=\omega_c$. Near the antenna where the density is low and $\omega_c>\omega$ the second term in the

Fig. 3.3 Polarization wherever $k_x^2>0$ for case shown in Fig. 3.2.

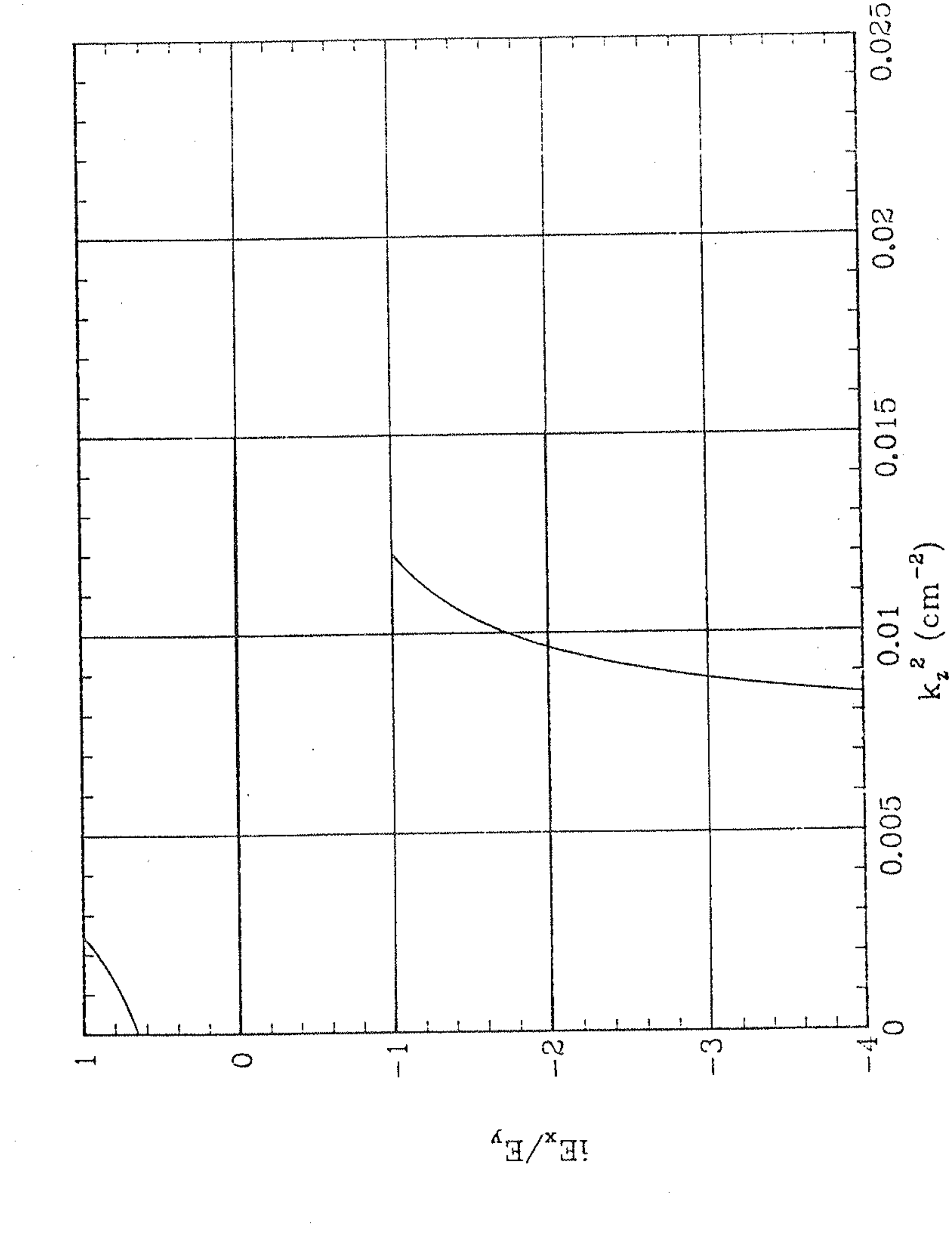
iE_x/E_y
1
0
−1
−2
−3
−4
0
0.005
0.01
0.015
0.02
0.025
k_z^2 (cm^-2)

denominator of Eq. (3.12) is negative with a magnitude greater than one. As the density increases and ω_c approaches ω the second term becomes less negative and eventually reaches a value of -1 at the perpendicular ion cyclotron resonance. Continuing towards the center of the machine we reach the $\omega=\omega_c$ layer where as discussed above P=+1.

3.3 Inhomogeneous Cold Plasma Theory

As mentioned earlier it's the warm plasma corrections to the plasma dielectric tensor that will provide some E^+ at the resonance zone and thus allow for some heating. Before discussing the warm plasma effects there is still some interesting physics to be learned from the cold plasma theory. First, ignoring polarization for the moment, we predict the magnitude of the RF electric field at the resonance zone, in particular E_y ($\hat{y}$ is the antenna direction) which was measured experimentally both with and without plasma. After all, even if we can show the presence of some E^+ at the resonance zone, no heating will result if the magnitude of the electric field there is vanishingly small. Second, we can draw some interesting comparisons with Barter's[3] experiment which, though quite similar to the Levitated Octupole experiment, has some important differences which are vital to explaining the heating.

We examine accessibility by deriving a differential equation for E_y. Combining Maxwell's Eq. (3.4) and the cold plasma dielectric tensor Eq. (3.7) we obtain

$$-\nabla^2\vec{E} + \vec{\nabla}(\vec{\nabla}\cdot\vec{E}) - k_o^2 \begin{pmatrix} S & -iD \\ iD & S \end{pmatrix} \begin{pmatrix} E_x \\ E_y \end{pmatrix} = 0 \qquad (3.13)$$

Assuming $\frac{\partial}{\partial y}=0$ and $\frac{\partial}{\partial z}=ik_z$, Eq. (3.13) can be written in the form,

$$\begin{pmatrix} k_z^2 - Sk_o^2 & +iDk_o^2 \\ -iDk_o^2 & -\frac{\partial^2}{\partial x^2} + k_z^2 - k_o^2 S \end{pmatrix} \begin{pmatrix} E_x \\ E_y \end{pmatrix} = 0 \qquad (3.14)$$

where S and D are known functions of x since they depend on the density and magnetic field. The antenna is defined to be at x=0. The top equation gives the familiar expression,

$$E_x = \frac{iDk_o^2}{Sk_o^2 - k_z^2} E_y \qquad (3.15)$$

which when substituted into the second equation yields

$$\frac{\partial E_y}{\partial x^2} + c(x)E_y = 0 \qquad (3.16)$$

where,

$$c(x) = \frac{(Sk_o^2-k_z^2)^2-D^2k_o^4}{Sk_o^2-k_z^2} \quad .$$

From the form of Eq. (3.16) we can expect exponential (evanescent) and sinusoidal (propagating) type solutions. It is shown by Stix[5] that at the singular point of Eq. (3.16) the asymptotic solutions join smoothly and there is no singularity in E_y. Equation (3.16) is solved numerically for given density and magnetic field profiles using a fourth-order Runge-Kutta routine. The equation is solved as an initial value problem where $E_y(o)$ and $E_y'(o)$ are specified. The value of $E_y(o)$ is normalized to 1, but the initial slope at x=0 must be chosen correctly for the particular k_z being used in order to get a physical evanescent solution near the edge. In the vicinity of the antenna where the density is very low

$$c \simeq -k_z^2$$

and the dispersion relation reduces to

$$k_x^2 = -k_z^2$$

The E_y field is measured to fall off exponentially near the antenna as $\exp(-x/\beta)$ where $\beta \approx 10$ cm (Fig. 4.1). The above relations which hold near the antenna therefore require

$$1/\beta = k_z \simeq 0.1 \text{ cm}^{-1}$$

Figure 3.4 shows the solution to Eq. (3.16) for $k_z=0.1$ cm^{-1} for the vacuum and plasma cases. The "vacuum" case is actually for a low density of 1×10^{11} cm^{-3} everywhere for reasons stated earlier, however, the solution still maintains the smooth decay with a slope close to that at $x=0$. Figure 3.5 shows the magnetic field profile used in solving for both the plasma and vacuum solutions and the density profile used in solving for the plasma solution. The thing to note in Fig. 3.4 is that $E_{y\ \mathrm{plasma}}$ is not very different from the vacuum case. A similar plot using data taken with the electric field probe (Fig. 4.1) confirms this behavior experimentally. In Fig. 4.1, E_y is attenuated appreciably near the separatrix, but that is a separate effect due to the field null and thus the high conductivity in the toroidal direction which enables the plasma to shield out the RF. The perpendicular ion cyclotron resonance is illustrated in Fig. 3.6 with a plot of E_x/i as calculated from Eq. (3.15). From Figs. 3.6 and 3.4 we calculate E^+ and E^- with plasma at $\omega=\omega_c$ to be

Fig. 3.4 Solution to differential equation for E_y (Eq. 3.16). Magnetic field and density profiles are shown in Fig. 3.5.

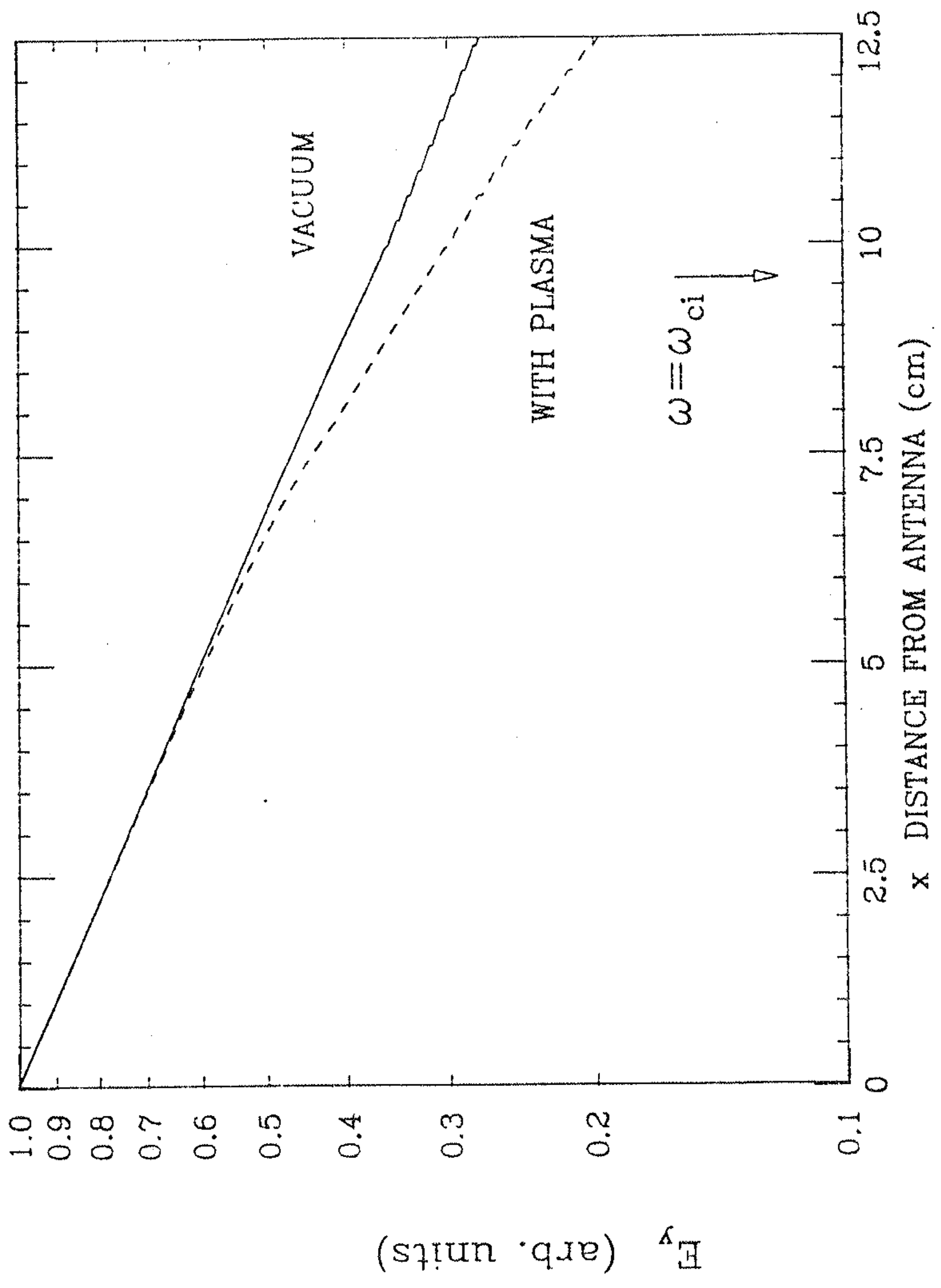
E_y (arb. units)
1.0
0.9
0.8
0.7
0.6
0.5
0.4
0.3
0.2
0.1
0
2.5
5
7.5
10
12.5
x DISTANCE FROM ANTENNA (cm)
VACUUM
WITH PLASMA
$\omega = \omega_{ci}$

Fig. 3.5 Magnetic field and density profiles used in solving Eq. 3.16.

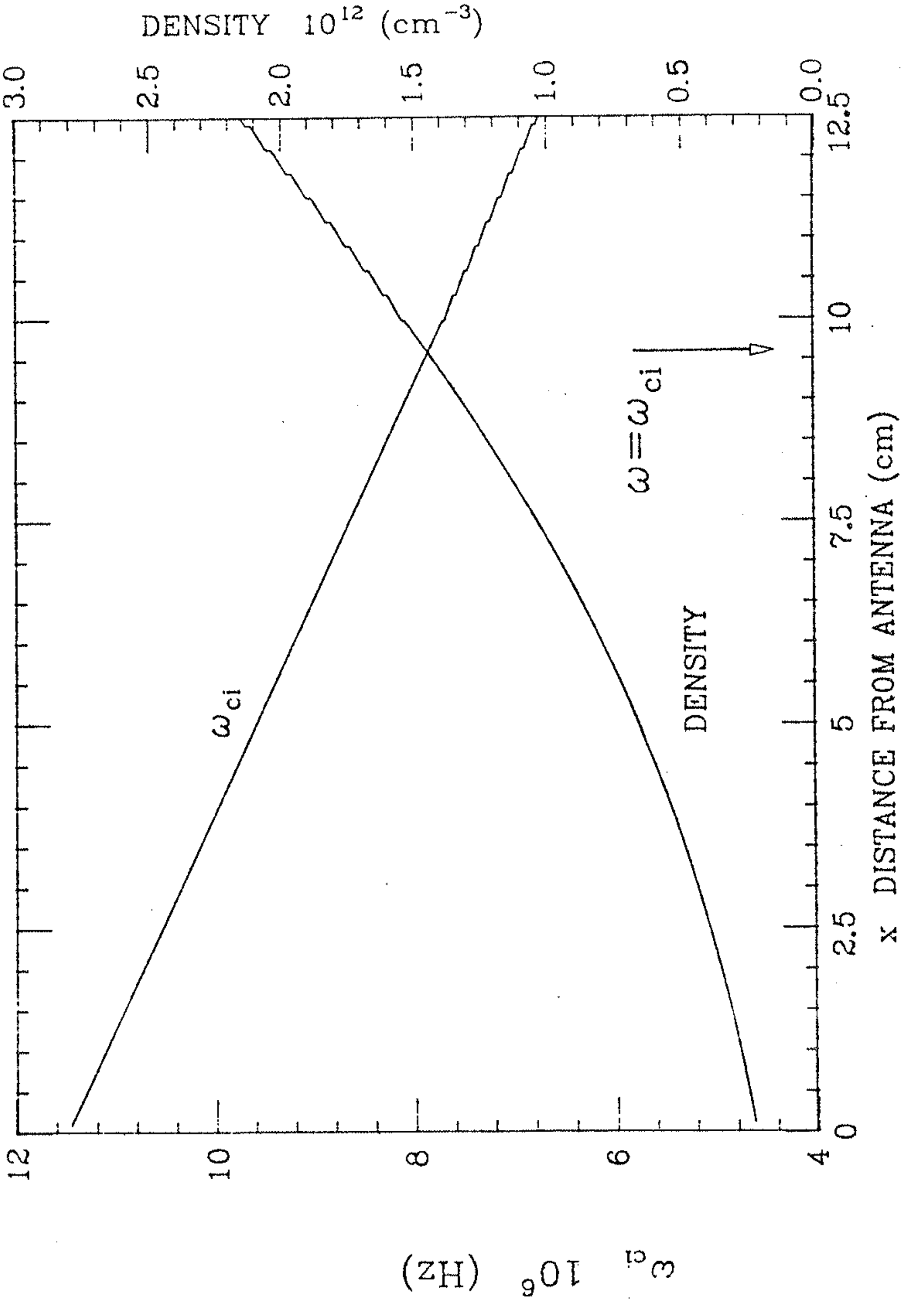
DENSITY 10^{12} (cm^{-3})
3.0
2.5
2.0
1.5
1.0
0.5
0.0
ω_{ci}
$\omega = \omega_{ci}$
DENSITY
0
2.5
5
7.5
10
12.5
x DISTANCE FROM ANTENNA (cm)
12
10
8
6
4
ω_{ci} 10^6 (Hz)

Fig. 3.6 E_x as calculated from Eq. 3.15.

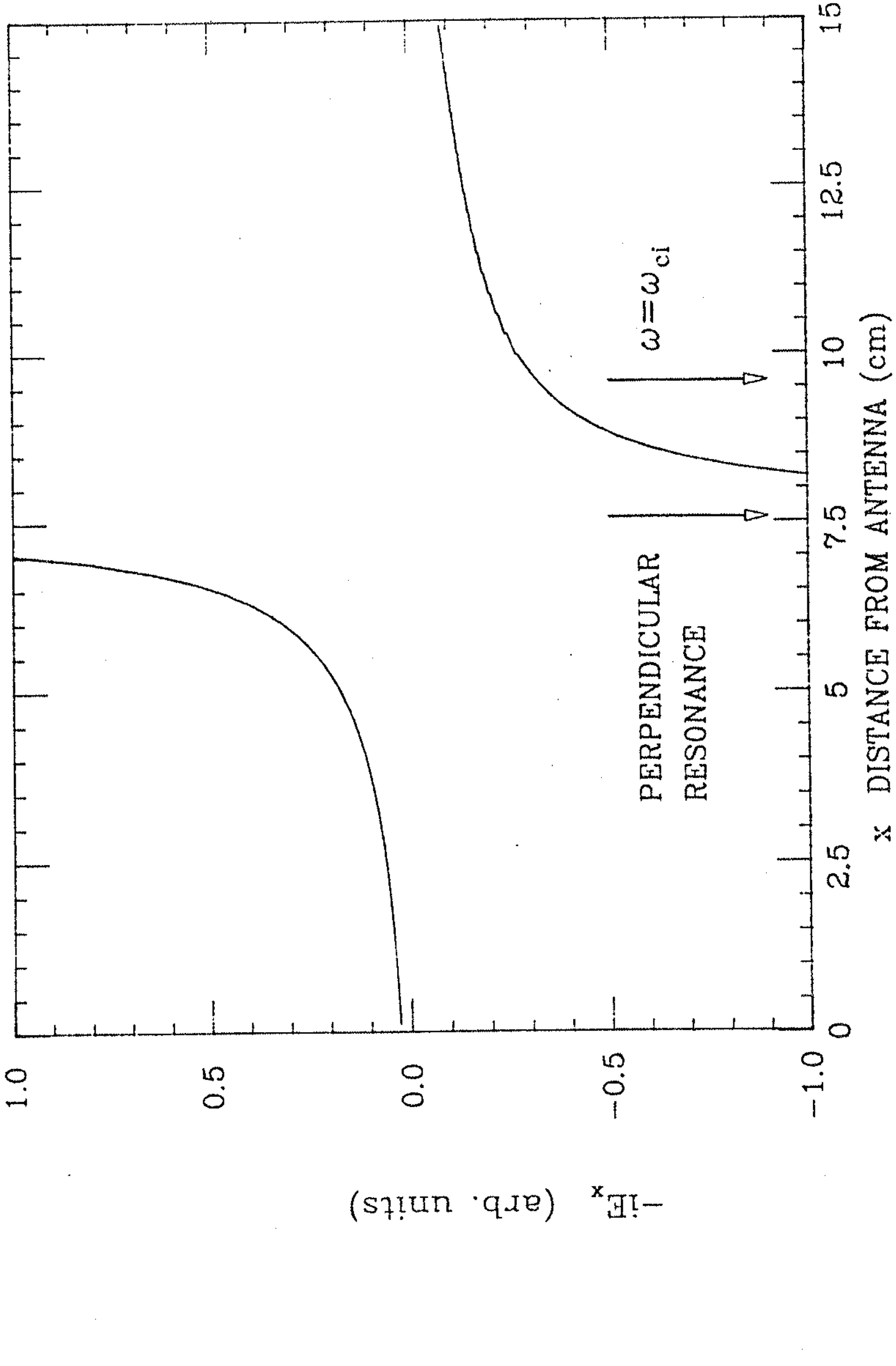
1.0
0.5
0.0
−0.5
−1.0
$-iE_x$ (arb. units)
0
2.5
5
7.5
10
12.5
15
x DISTANCE FROM ANTENNA (cm)
PERPENDICULAR
RESONANCE
$\omega=\omega_{ci}$

$$E^{+} = \frac{1}{\sqrt{2}}(E_x + iE_y) = 0$$

$$E^{-} = \frac{1}{\sqrt{2}}(E_x - iE_y) = 2E^{-}_{vac} \quad .$$

As in the homogeneous plasma model, the left-hand component to the electric field for the inhomogeneous plasma is calculated to be zero. However, we have learned that the magnitude of the toroidal RF electric field is only slightly perturbed from the vacuum case. The left-hand component has gone to zero, but the right-hand component has doubled to keep the same E_y as present in the vacuum.

At this point we address the question of a mechanism that will allow for the presence of some E^{+} at the $\omega=\omega_c$ layer. The distance from the $\omega=\omega_c$ layer where $E^{+}=0$ to the perpendicular ion cyclotron resonance where $E^{+}\neq 0$ is defined to be a tunnelling zone for the LCP component. An analysis similar to this but performed in cylindrical coordinates was done by Barter[3]. Using an analytic expression for the magnetic field along the Octupole midcylinder, we solve for the position of the perpendicular ion cyclotron resonance using Eq. (3.12). The perpendicular ion cyclotron resonance is given by,

$$1 + \frac{k_z^2 c^2}{\omega_p^2}\left(1 - \frac{\omega_c^2}{\omega^2}\right) = 0$$

where the density and k_z are treated as free parameters. Knowing the position of the resonance zone we calculate the width of the tunnelling zone from

$$\Delta r = X_{perp.res.} - X_{\omega=\omega_c} \quad .$$

We ask what energy ion will possess a gyroradius such that,

$$\rho = \Delta r \quad .$$

This analysis was done for both the small Octupole (Barter's experiment) and the Levitated Octupole. The results are plotted in Figs. 3.7 and 3.8. For a given k_z, ions with energies above the curve possess gyroradii large enough to span the tunnelling zone and thus wash out the plasma shielding of E^+. Note that the perpendicular cyclotron resonance lies closer to the $\omega=\omega_c$ layer for smaller wavelength modes. A better analysis considering the spectrum of k_z's that sum to make the electric field is presented in the next section. However, the point to be made here is that because of the relative sizes, the small Octupole fields are dominated by shorter wavelengths than the Levitated Octupole. Comparisons of plots of the E_y electric field in Barter's thesis with those for the Levitated Octupole (Figs. 4.1 and 4.2) show that there is approximately a factor of 2 in the scale lengths. The conclusion we draw from Figs. 3.7 and 3.8 is that for the small

Fig. 3.7 Graphical illustration of ´tunneling´ effect on the left-hand component of the RF electric field for the Small Octupole.

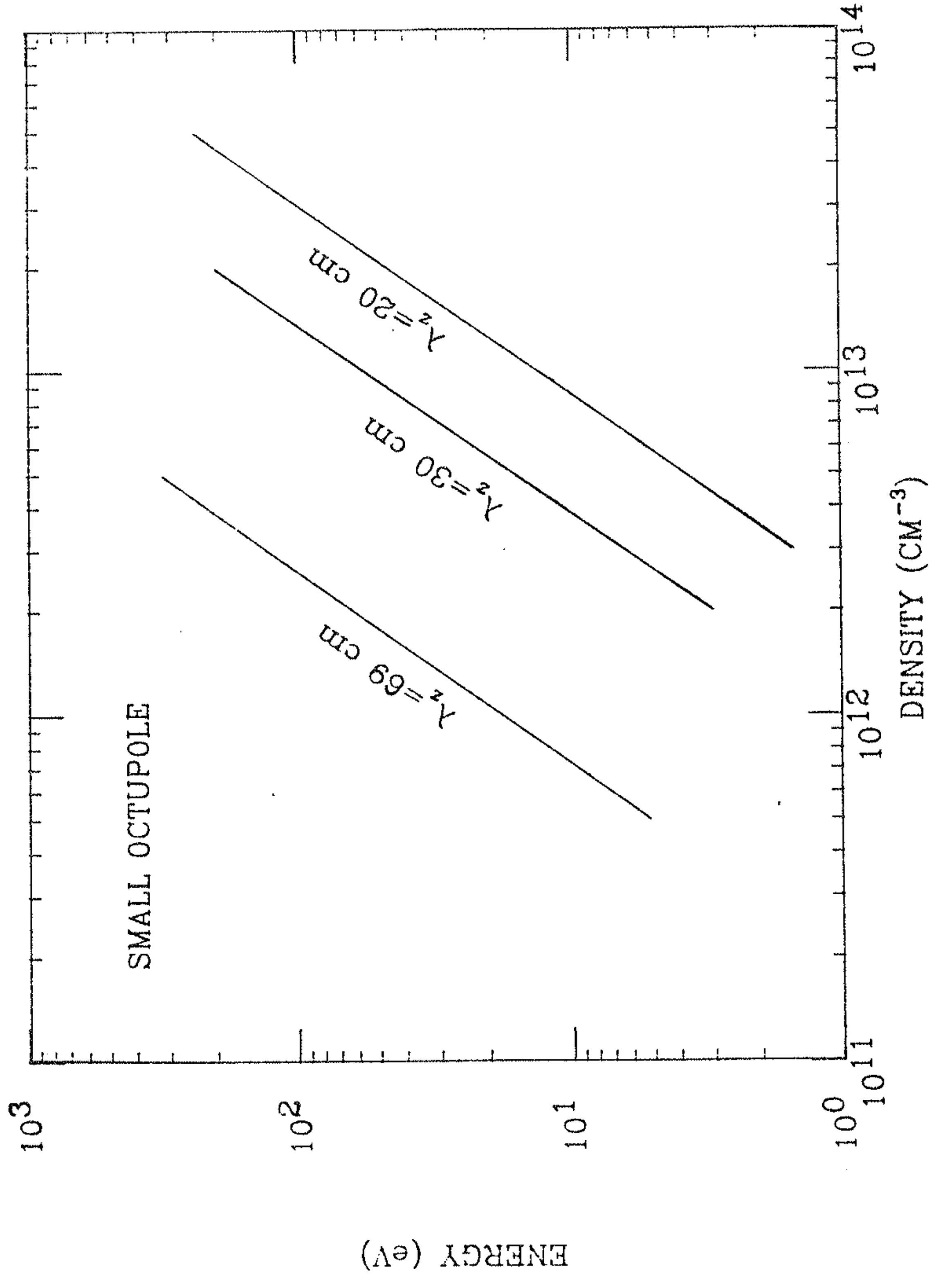
SMALL OCTUPOLE
λ_z=20 cm
λ_z=30 cm
λ_z=69 cm
ENERGY (eV)
10^3
10^2
10^1
10^0
DENSITY (CM^{-3})
10^{11}
10^{12}
10^{13}
10^{14}

Fig. 3.8 As in Fig. 3.7, but for Levitated Octupole.

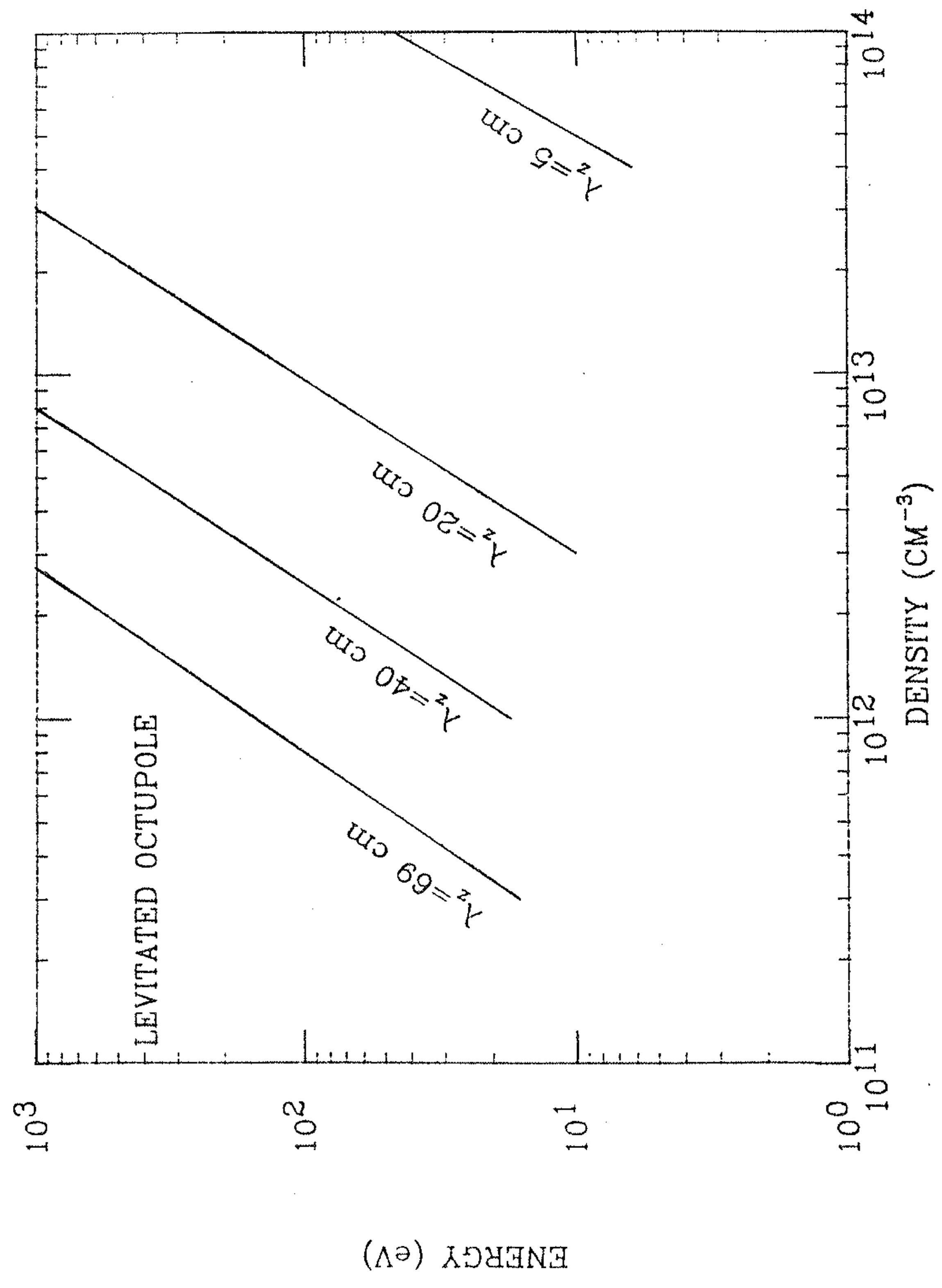
LEVITATED OCTUPOLE
λ_z=69 cm
λ_z=40 cm
λ_z=20 cm
λ_z=5 cm
ENERGY (eV)
10^0
10^1
10^2
10^3
DENSITY (CM^{-3})
10^{11}
10^{12}
10^{13}
10^{14}

Octupole parameters $(n(\omega=\omega_c)\lesssim 1.5\times 10^{12}$ and $\lambda_z\approx 30$ cm), ion temperatures of only a few eV are necessary for ions at the resonance zone to "feel" some E^+ and thus get heated. However for the Levitated Octupole, because of its larger size and somewhat higher densities ($\lambda_z\approx 60$–70 cm, $n(\omega=\omega_c)\gtrsim 1.5\ 10^{12}$), temperatures of several hundred eV are needed for gyroradii to span the tunnelling zone. In Barter´s theoretical analysis of the loading he used the vacuum electric field. It appears that this is not justifiable for the Levitated Octupole, and so a different mechanism is needed to explain the heating.

3.4 Lowest Order Hot Plasma Corrections

In this section we apply the lowest order hot plasma corrections and consider the more realistic case of a continuous k_z spectrum to calculate the magnitude of E^+ at the resonance zone. To do this we will be using the experimentally measured and theoretically derived fact that E_y does not vary much from its vacuum value. We will find that a broad k_z spectrum (short wavelengths) is optimal for heating. This result is similar to the one derived in the last section, but rather than finite gyroradius effects, in the lowest order hot plasma correction it is a doppler shift which supplies some E^+ at the resonance zone. It should be noted that $k_x\rho_i$ terms do come into the hot plasma theory, but they appear in higher order terms than will be considered here.

Before proceeding to the calculation we present a simple physical picture to illustrate the interdependence between the doppler shift and the k_z spectrum. In Fig. 3.9 we consider broad and narrow k_z spectrums for both the cold and hot plasma models. The abscissa represents the position of an ion along a field line, and the ordinate is the magnitude of the electric field. Since the waves are evanescent, the sign of the electric field is the same everywhere at any instant in time. In Figs. 3.9a and b there is of course no doppler shift since the ion is not moving along the field line and thus, independent of its z-position, it sees an electric field oscillating at frequency ω. In Fig. 3.9c with a narrow k_z spectrum, there will be some doppler shift, and in Fig. 3.9d a greater doppler shift with the broader k_z spectrum. For example, in Fig. 3.9d, if the phase of the electric field is such that it is increasing as the ion moves along the field line, the ion feels an up-shifted frequency, and a down-shifted frequency if the electric field is decreasing. This mechanism effectively broadens out the resonance zone and results in a finite amount of E^+ being present for heating.

To quantify this effect we start by writing down the hot plasma tensor elements to first order[6,7].

Fig. 3.9 Physical picture of Doppler broadening of resonance zone.

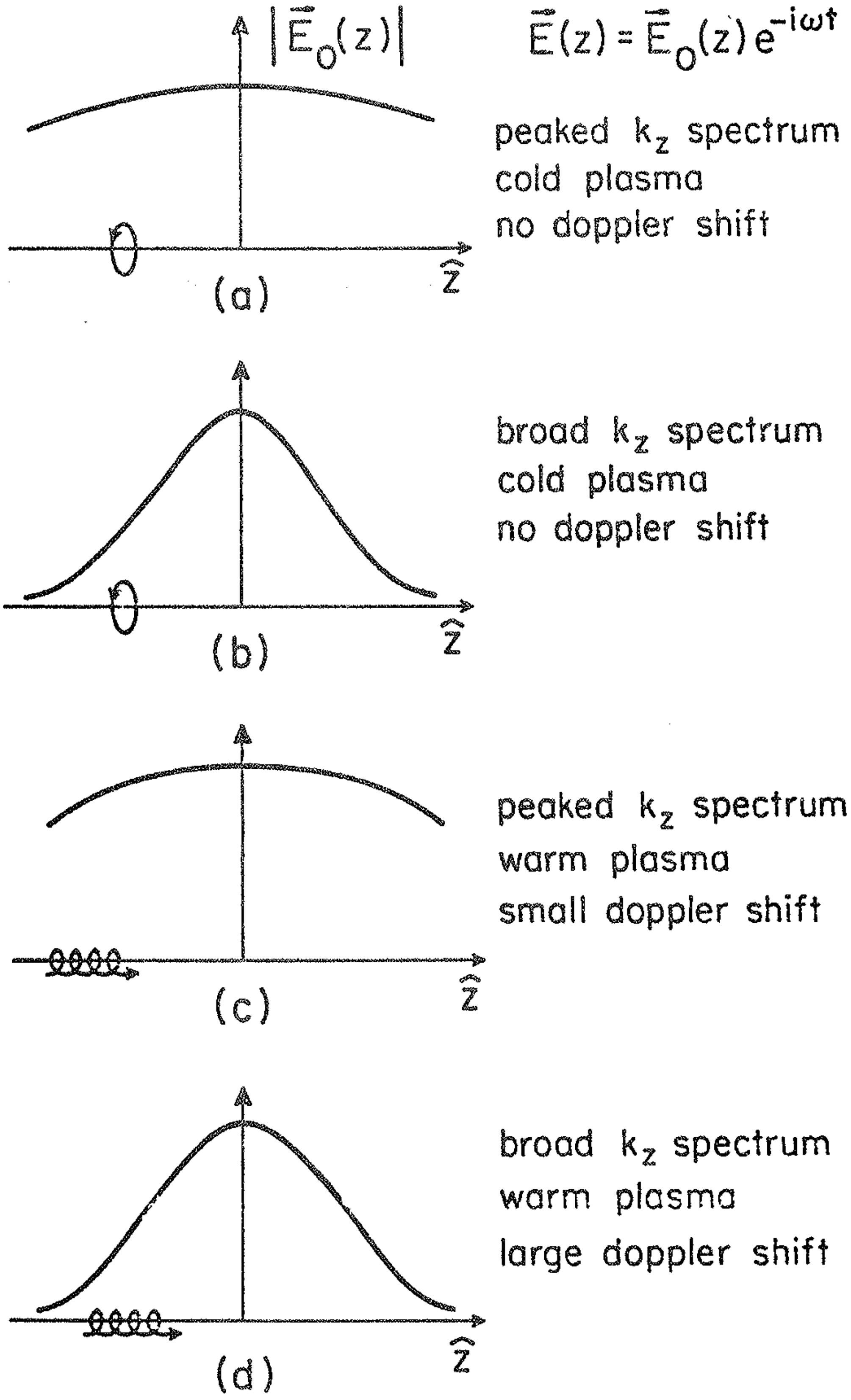
$|\vec{E}_0(z)|$
$\vec{E}(z) = \vec{E}_0(z)\, e^{-i\omega t}$
peaked k_z spectrum
cold plasma
no doppler shift
$\hat{z}$
(a)
broad k_z spectrum
cold plasma
no doppler shift
$\hat{z}$
(b)
peaked k_z spectrum
warm plasma
small doppler shift
$\hat{z}$
(c)
broad k_z spectrum
warm plasma
large doppler shift
$\hat{z}$
(d)

$$S = k_o^2 + \frac{1}{2} \sum_\alpha \varepsilon_\alpha \mu_1$$

$$D = \frac{1}{2} \sum_\alpha \varepsilon_\alpha \nu_1 \tag{3.17}$$

where,

$$\varepsilon_\alpha = \frac{\omega_{\rho\alpha}^2 k_o^2}{\omega k_z v_\alpha}$$

$$\mu_1 = Z_1(\xi_1) + Z_{-1}(\xi_{-1})$$

$$\nu_1 = Z_1(\xi_1) - Z_{-1}(\xi_{-1})$$

$$\xi_1 = \frac{\omega + \omega_{c\alpha}}{k_z v_\alpha} \quad .$$

Here α indicates the particle species, $\omega_{c\alpha}$ is a signed quantity, k_z is the absolute magnitude of k_z, v_α is the thermal velocity=$(2kT_\alpha/m_\alpha)^{1/2}$, and Z is the plasma dispersion function of argument ξ. As stated earlier the spatial structure of the electric field is due to a fourier spectrum of k_z's which is determined by the geometry of the antenna and the nearby boundaries such as the rings and floor. For a constant height (x) above the antenna, the vacuum electric field E_y, (recall $\hat{y}$ is in the direction of the antenna), has a gaussian shape (Fig. 4.2) in z where z is the distance from the midcylinder. We fourier transform the measured vacuum field,

$$\vec{E}_{vac} = E_o e^{-(z/\alpha)^2}\hat{y} \quad , \tag{3.18}$$

where α is the gaussian width, to obtain

$$\tilde{E}_{vac}(k_z) = \frac{E_o}{\sqrt{2}}\,\alpha\, e^{-k_z^2\alpha^2/4}$$

where the tilde signifies a fourier transformed quantity. Since $E_{x\ vac}=0$ then,

$$\tilde{E}^+_{vac}(k_z) = \frac{i}{\sqrt{2}}\,\tilde{E}_{vac}(k_z) = \frac{i}{2}\,E_o\alpha e^{-k_z^2\alpha^2/4} \quad . \tag{3.19}$$

Using the subscript p to denote plasma quantities we have,

$$\tilde{E}^+_p(k_z) = \frac{1}{\sqrt{2}}\,(\tilde{E}_{xp}+i\tilde{E}_{yp}) \quad . \tag{3.20}$$

The x-component of the electric field is given by

$$\tilde{E}_{xp} = \frac{iDk_o^2}{Sk_o^2-k_z^2}\tilde{E}_{yp} \quad . \tag{3.21}$$

Using the assumption that each fourier component of the toroidal field (E_y) penetrates unattenuated, then Eq. (3.20) can be written as

$$\tilde{E}_p^+(k_z) = \frac{iE_o}{2}\alpha\, e^{-k_z{}^2\alpha^2/4}\,(1-P(k_z)) \tag{3.22}$$

where $1-P(k_z)$ can be considered the plasma response function. Recall $P(k_z)=-Dk_o^2/(Sk_o^2-k_z^2)$ where D and S are defined by Eq. (3.17). In general the plasma dispersion function is complex, and the inverse fourier transform must be performed separately on the real and imaginary parts of Eq. (3.22). We evaluate the magnitude after we do the inverse fourier transform for $\omega=\omega_c$ and $z=0$. The $z=0$ case is examined to find the magnitude of E^+ where the resonance zone crosses the midcylinder ($z=0$) and comes closest to the antenna (Fig. 1.1). Since the fields are evanescent this is the region on the resonant mod-B surface where the fields are strongest, and thus, where most of the heating takes place. Further discussion of this is given in the next chapter where ion and electron temperature profiles are presented. A computer program was written to calculate the inverse fourier transform

$$E^{+}(z=0) = \left| \frac{i}{\sqrt{2\pi}} \frac{E_o}{2} \alpha \int_{-\infty}^{\infty} e^{-k_z{}^2\alpha^2/4}(1-P(k_z))dk_z \right| \quad (3.23)$$

The heating rate or loading is proportional to

$$n|E^{+}|^2 \quad (3.24)$$

where the density and E^{+} are evaluated at the resonance zone. The results for α=8.6 cm at various temperatures are plotted in Fig. 3.10. The vacuum E_y is normalized to 1 and is dimensionless making $|E^{+}_{vac}|^2$=0.5$|iE_{y\ vac}|^2$=0.5. The density (n) is expressed in units of 10^{12} cm^{-3}, and the vacuum curve is defined by n/2. The plasma attenuates the vacuum E^{+} with the attenuation being greater for the colder plasmas as we expect; however, it is interesting to note that the attenuation is not very sensitive to temperature above 10-20 eV. The point is that, even for the very cold cases, there is a finite amount of E^{+} at the resonance zone. For example, at 1×10^{12} cm^{-3}, the loading is down by about an order of magnitude for a nearly "worst" case of 5 eV. This means that the left-hand component is ~30% of its vacuum value. Remember the cold plasma model predicts E^{+}=0 for all densities and k_z´s, and hot plasma effects are important and can account for the heating.

Fig. 3.10 Temperature effects on the loading for a given k_z spectrum.

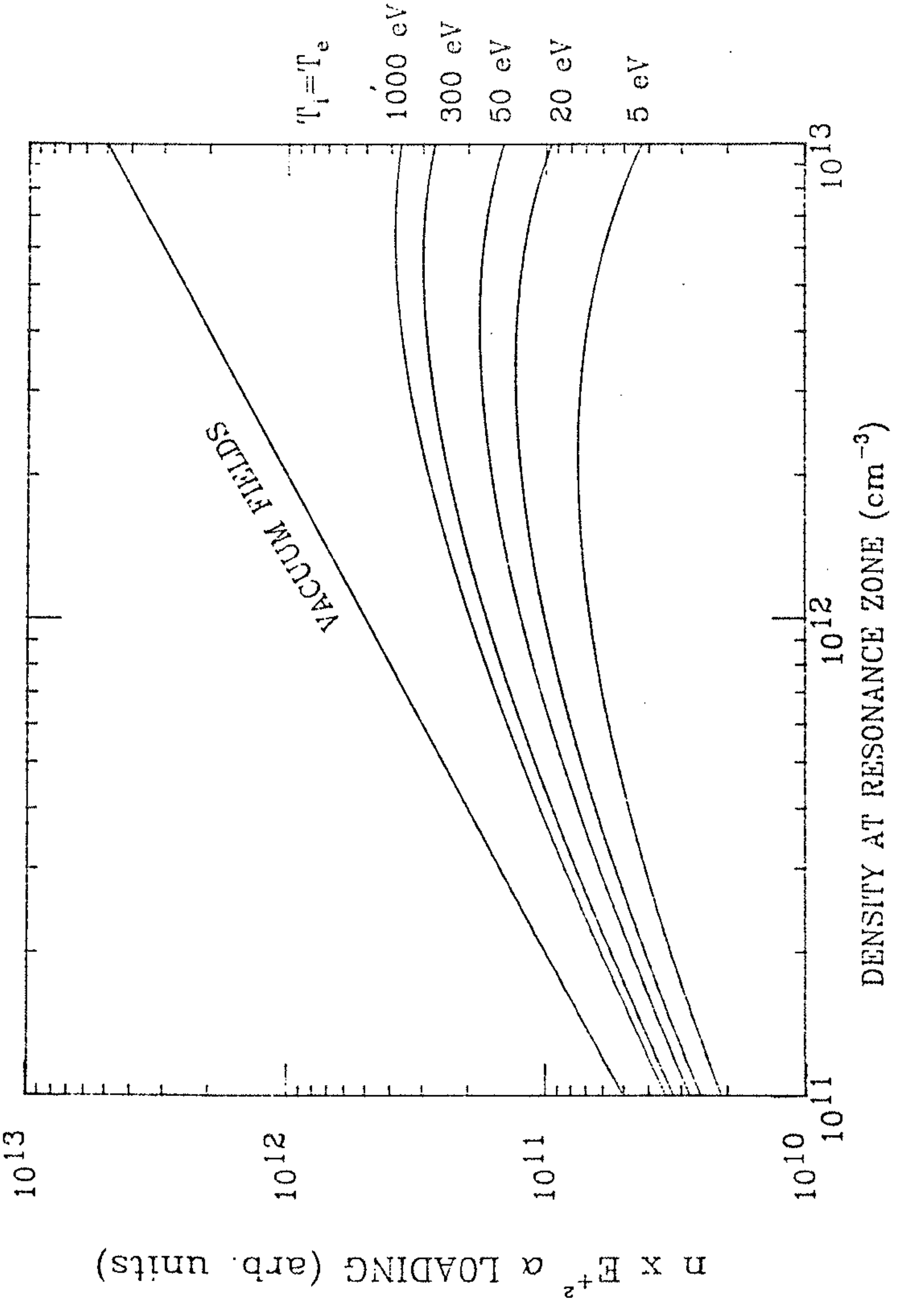
VACUUM FIELDS
$T_i = T_e$
1000 eV
300 eV
50 eV
20 eV
5 eV
10^{11}
10^{12}
10^{13}
DENSITY AT RESONANCE ZONE (cm^{-3})
10^{10}
10^{11}
10^{12}
10^{13}
n x E^{+2} α LOADING (arb. units)

Figure 3.11 shows how the loading depends on α, the parameter which determines the k_z spectrum. Spectra with short wavelength modes have a smaller value for α and thus exhibit heavier loading. Further results of the warm plasma calculation are presented in the next chapter with the experimental heating results.

To summarize the results so far, we have shown:

1) Homogeneous cold plasma theory predicts $E^+=0$ at the resonance zone and therefore predicts no heating.
2) Inhomogeneous cold plasma theory also predicts $E^+=0$ at the resonance zone but the magnitude of the toroidal component of the electric field, E_y, penetrates well to the resonance zone. This result is confirmed by experimental measurements.
3) The warm plasma theory, using the lowest order corrections to the plasma dispersion tensor elements, predicts that there will be some E^+ at the resonance zone. The magnitude depends on the density and temperature as well as the parameter α which describes the gaussian profile of E_y along a field line.

3.5. Damping

The heating rate involves the density and the square of E^+ summed over all volume elements in the machine where $\omega \simeq \omega_c$. The discussion up to this point has addressed only the question of calculating the magnitude of E^+ at the resonance zone. We now

Fig. 3.11 Parallel wavelength effects on the loading for a given plasma temperature.

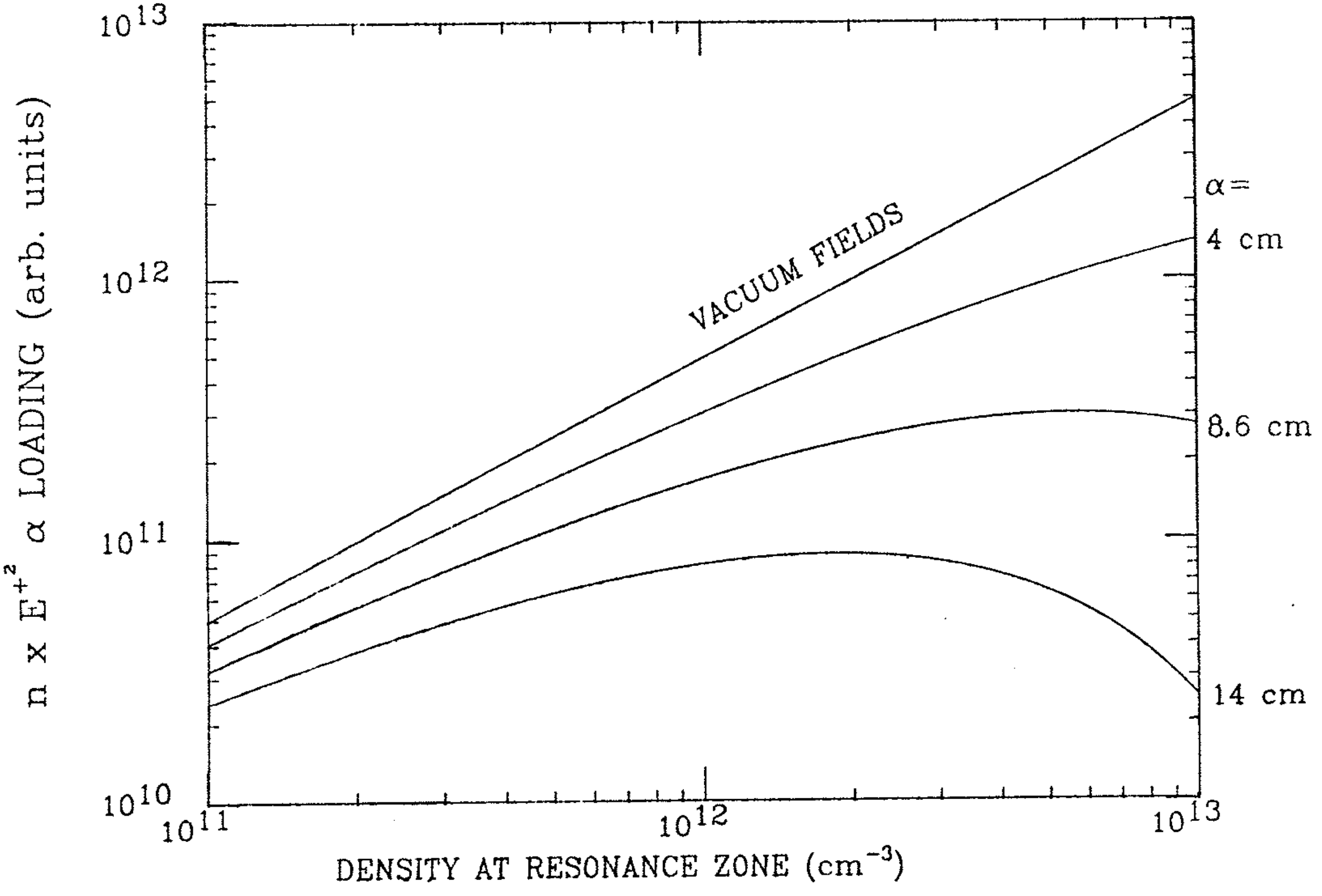
n x E+² α LOADING (arb. units)
DENSITY AT RESONANCE ZONE (cm⁻³)
10¹⁰
10¹¹
10¹²
10¹³
10¹¹
10¹²
10¹³
VACUUM FIELDS
α=
4 cm
8.6 cm
14 cm

calculate the heating rate for a given magnitude of E^+ at the resonance zone.

The approach is to consider the plasma as a resistive medium by introducing an imaginary component to the frequency $\nu \ll \omega$ and then to calculate the power absorbed per unit volume from

$$\frac{dP}{dV} = \mathrm{Re}\left|(\overleftrightarrow{\sigma}\cdot\vec{E})^{*}\cdot\vec{E}\right| \quad . \tag{3.25}$$

This method was also used by both Sprott[2] and Barter[3]. In order to bring out the explicit dependence of the heating on E^+ we perform a similarity transformation on the conductivity tensor expressed in a cartesian coordinate system[8],

$$\begin{matrix} \sigma_{11} & i\sigma_{12} & 0 \\ -i\sigma_{12} & \sigma_{11} & 0 \\ 0 & 0 & \sigma_{33} \end{matrix} \tag{3.26}$$

to obtain the tensor in a $\hat{R}$, $\hat{L}$, $\hat{Z}$ coordinate system,

$$\begin{matrix} \sigma_{11}-\sigma_{12} & 0 & 0 \\ 0 & \sigma_{11}+\sigma_{12} & 0 \\ 0 & 0 & \sigma_{33} \end{matrix} \qquad (3.27)$$

where in MKS units,

$$\sigma_{11} = i\varepsilon_o\omega_p^2 \frac{\omega-i\nu}{(\omega-i\nu)^2-\omega_c^2}$$

$$\sigma_{12} = i\varepsilon_o\omega_p^2 \frac{\omega_c}{(\omega-i\nu)^2-\omega_c^2} \qquad (3.28)$$

$$\sigma_{33} = \frac{i\varepsilon_o\omega_p^2}{\omega-i\nu} \quad .$$

This allows us to express Eq. (3.25) in the circularly polarized coordinate system as

$$\frac{dP}{dV} = \text{Re}[(\sigma_{11}-\sigma_{12})^*|E^-|^2 + (\sigma_{11}+\sigma_{12})^*|E^+|^2] \quad . \qquad (3.29)$$

The first term is about zero for $\omega \simeq \omega_c$ as we would expect, and after taking the real part of the second term we obtain,

$$\frac{dP}{dV} = \frac{-\varepsilon_o\omega_p^2\nu(\omega^2+\omega_c^2+\nu^2+2\omega\omega_c)|E^+|^2}{(\omega^2-\omega_c^2)^2+\nu^2(2\omega^2+2\omega_c^2+\nu^2)} \quad . \tag{3.30}$$

For $\omega\tilde{=}\omega_c$ the power per unit volume absorbed by the plasma is given by

$$\frac{dP}{dV} = \frac{e}{B_o}\,\frac{4\gamma|E^+|^2}{(1-\rho^2)^2+4\gamma^2} \tag{3.31}$$

where we've adopted the Barter notation $\rho=\omega_c/\omega=B/B_o$ and $\gamma=\nu/\omega$. Using the identities,

$$\lim_{\gamma\to 0}\frac{1}{\pi}\,\frac{\gamma}{x^2+\gamma^2} = \delta(x) \tag{3.32}$$

and

$$\delta(x^2-a^2) = \frac{1}{2a}\,[\delta(x+a)+\delta(x-a)]$$

Eq. (3.31) can be expressed in the form,

$$P = \pi e\int n|E^+|^2\delta(B-B_o)dV \quad . \tag{3.33}$$

A computer program calculates the integral for a given density profile, magnetic field strength, and electric field spatial structure. Barter used the vacuum electric fields for the Small Octupole, but, for the Levitated Octupole, plasma effects become important, and using the vacuum field would not be correct. This added complication brings extra free parameters into the theory such as the k_z spectrum and plasma temperature. We have calculated using a slab model the magnitude of E^+ where the resonance zone crosses the midcylinder. The slab model is interfaced with the Octupole field geometry in the following manner. Equation (3.33) is evaluated for each point on the resonant mod-B surface using the actual local density (the resonance zone crosses different flux surfaces) and the attenuated E^+ as calculated by the warm plasma slab model as if the point being evaluated were on the midcylinder. This is reasonable since most of the heating takes place near the bottom of the resonance zone, close to the antenna, and near the midcyliner. The factor by which $|E^+|^2$ is suppressed from the vacuum is given by Figs. 3.10 and 3.11. The numerical results were fitted to an analytic expression by a nonlinear regression analysis which was then subsequently used in the computer code to calculate Eq. 3.33.

The model as applied to the Levitated Octupole has some built in assumptions that may be inaccurate. The model uses straight field lines whereas the Octupole field lines are highly convoluted in places. The slab model was used because near the region of interest, above the antenna, the field lines are somewhat straight, and on the midcylinder they are in fact parallel to each other. The slab approximation also makes the fourier spectrum for the electric field at a constant height above the antenna not quite the same as the spectrum on an Octupole field line. Another assumption involves using a Maxwellian velocity distribution to take into account the warm plasma effects. It is reasonable to guess that near the antenna the velocity distribution for ions may be somewhat anisotropic. However, as we shall see in the next chapter the damping model coupled with the warm plasma model to estimate the magnitude of E^+ at the resonance zone gives results that are in reasonable agreement with the experiment.

REFERENCES - CHAPTER 3

1. T.H. Stix, The Theory of Plasma Waves (McGraw-Hill, N.Y., 1962), Chaps. 1,2.
2. J.C. Sprott, Ph.D. Thesis, University of Wisconsin (1969).
3. J.D. Barter, Ph.D. Thesis, University of Wisconsin (1976).
4. T.H. Stix, Nuclear Fusion 15, 737 (1975).
5. T.H. Stix, Physics of Fluids 3, 19 (1960).
6. B.D. McVey, MIT report PFC/RA-82-7 (1982).
7. B.D. McVey, Ph.D. Thesis, University of Wisconsin (1978).
8. C.B. Wharton in Plasma Diagnostic Techniques, R.H. Huddlestone, S.L. Leonard, eds. (Academic Press, N.Y., 1965), Chapt. 11.

CHAPTER 4

EXPERIMENTAL RESULTS AND DISCUSSION

4.1 Electric Field Measurements

The electric field probe was used to measure the E_y (toroidal) electric field on the midcylinder as a function of height above the antenna. The data are shown in Fig. 4.1. We see that from the antenna up to and through the resonance zone the electric field with and without plasma is nearly identical. The electric field in the presence of plasma is depressed near the separatrix because at the field null toroidal plasma currents are generated to buck out the RF fields. Vacuum field measurements were also done off the midcylinder at various distances above the shield. The curves with their gaussian analytical fits are plotted in Fig. 4.2. The gaussian widths for the various curves are plotted in Fig. 4.3 and fitted to the indicated power law. It is assumed that, as in the midcylinder data, E_y off the midcylinder is essentially the same with and without plasma. We are then able to deduce an expression for E_y everywhere in the vicinity of the antenna.

$$E_y = E_o e^{-x/\beta} e^{-(z/\alpha)^2}$$

where

Fig. 4.1 Measured RF toroidal electric field penetration on the midcylinder.

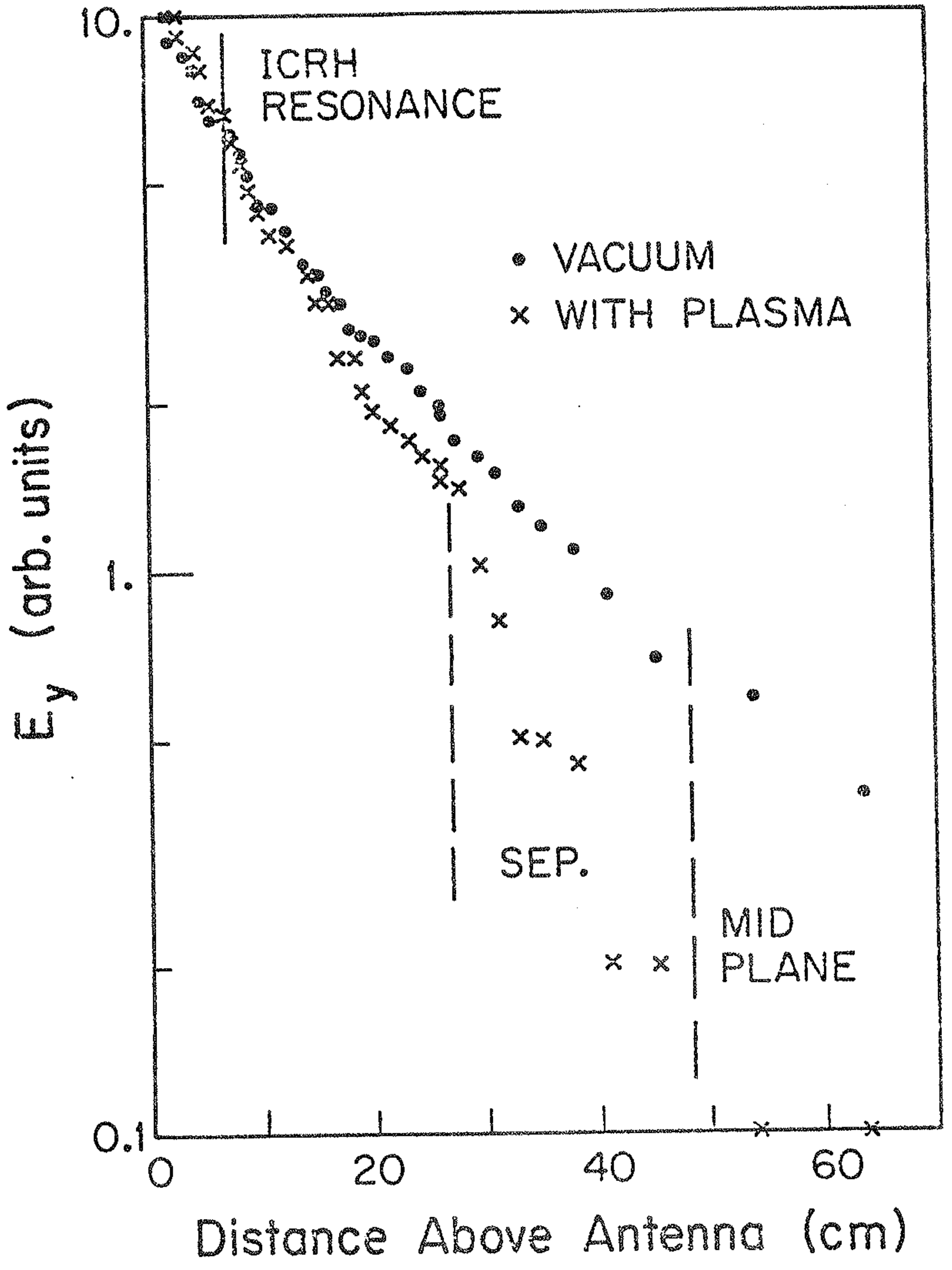
10.
1.
0.1
0
20
40
60
Distance Above Antenna (cm)
E_y (arb. units)
ICRH
RESONANCE
● VACUUM
× WITH PLASMA
SEP.
MID
PLANE

Fig. 4.2 Measured off-axis RF toroidal electric field with analytical fit.

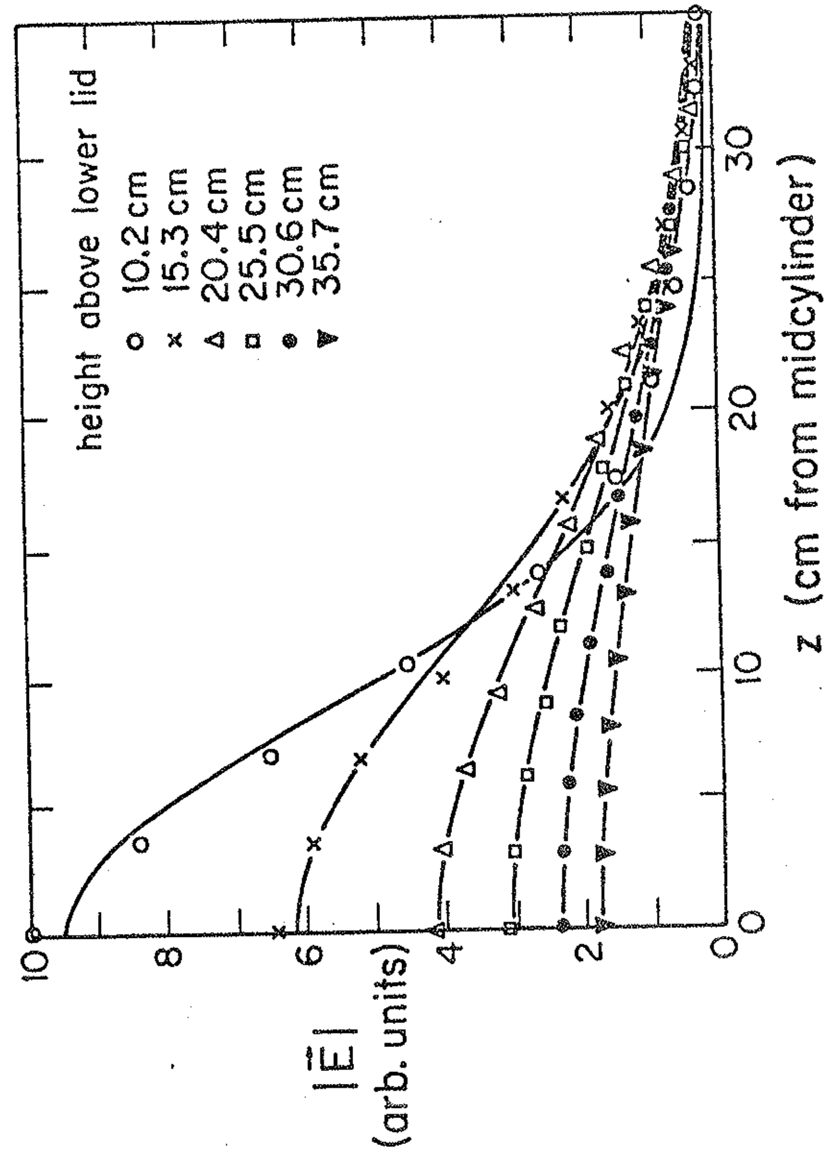
height above lower lid
○ 10.2 cm
× 15.3 cm
△ 20.4 cm
□ 25.5 cm
● 30.6 cm
▼ 35.7 cm
|$\vec{E}$|
(arb. units)
10
8
6
4
2
0
0
10
20
30
z (cm from midcylinder)

Fig. 4.3 Gaussian width for curves plotted in Fig. 4.2 as a function of height above Faraday shield.

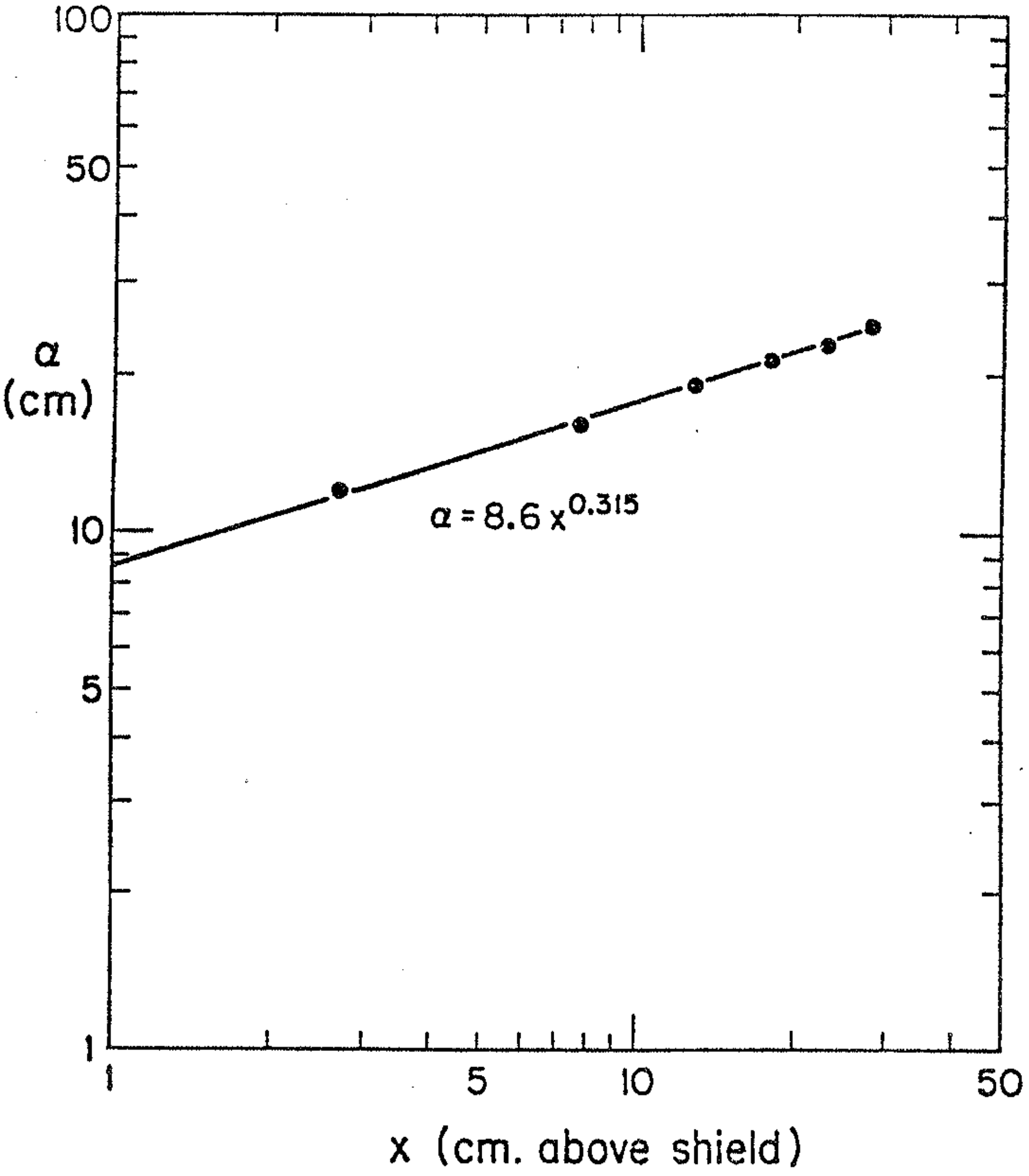
100
50
10
5
1
α
(cm)
α = 8.6 x^0.315
1
5
10
50
x (cm. above shield)

$$\alpha = 8.6\ x^{0.315}$$

and x is the distance above the Faraday shield. This expression goes into the computer code that calculates the plasma loading (Eq. 3.33).

4.2 Loading Measurement Procedure

In any heating experiment, antenna loading and Q measurements are of vital importance. It is perhaps the best test for comparison with a heating theory, and for the experimentalist it is a relatively easy measurement to make. The Octupole RF source is somewhat unconventional in that it is an oscillator with the antenna serving as the resonating tank circuit inductor. There are no matching networks or a transmission line in which to place directional couplers. A more detailed description than will be presented here on the general subject of loading measurements is given in PLP 890.[1]

Losses in a tank circuit can be modelled as being dissipated by either a resistance in series with the antenna inductance, defined here as a radiation resistance or a resistance in parallel. These models are illustrated in Fig. 4.4 and are equivalent for moderately high Q ($\gtrsim 5$) tank circuits. The relationship between the two models is given by,

$$(\omega L)^2 = R_\parallel R_{rad} \quad \text{where,}$$

Fig. 4.4 Two models of equivalent tank circuit with finite Q.

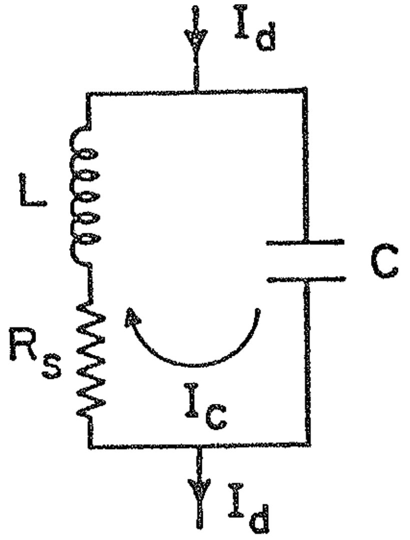

Series Resistance Model

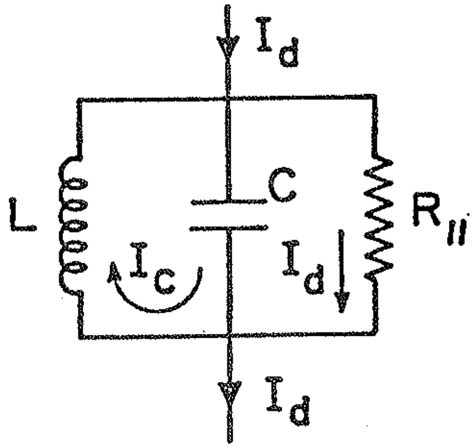

Parallel Resistance Model

$$\omega = 1/\sqrt{LC} \quad .$$

For the series resistance model,

$$R_{rad} = R_{\substack{rad\\ant}} + R_{\substack{rad\\plasma}}$$

and for the parallel resistance model

$$\frac{1}{R_{\parallel}} = \frac{1}{R_{\substack{\parallel\\ant}}} + \frac{1}{R_{\substack{\parallel\\plasma}}} \quad .$$

Since the circulating current in the antenna was measured directly with a pickup loop (Section 2.2.C), and dissipated power is given by $P=(1/2)I_c^2 R_{rad}$, the discussion and results will be presented in terms of radiation resistance. The two methods used to measure the Q of the unloaded tank circuit were.

1) Measure the bandwidth of the tank circuit, defined to be the half power level. Q is then just[2] $f_o/\Delta f$.

2) Ring the tank circuit with a square wave. The number of cycles to 1/e of the voltage, times π, is equal to[3] Q.

Both of these methods indicated a Q of ~100 for the unloaded tank circuit.

The method by which we determine the loading is to measure how much the plasma spoils the Q of the tank circuit. Therefore, we need a method of measuring the loaded Q. The loaded Q, Q_ℓ, of a tank circuit driven sinusoidally at its resonance frequency is given by,

$$Q_\ell = \frac{I_c}{I_d}$$

where I_c is the zero to peak circulating current and I_d is the zero-to-peak drive current. They are both sine waves at the RF frequency. This relationship is derived in the following manner:

$$Q = \frac{\omega \frac{1}{2} L I_c^2}{\frac{1}{2} I_d^2 R_{rad}} = \frac{\text{circulating power}}{\text{dissipated power}}$$

Since,

$$\omega L I_c = I_d R_\parallel = V_{ant}$$

then

$$Q = I_c / I_d \quad .$$

The circulating current is measured directly with the pickup loop, but with class C operation of the oscillator the total drive current is not sinusoidal, and so there is no direct way to measure the fundamental fourier component (I_d). However, a calibration was performed to relate the measured time average drive current (I^-) coming from the pulse forming network and the fundamental RF drive, I_d, by some proportionality constant k. The unloaded Q was previously determined to be 100, and thus without plasma we have,

$$Q_u = 100 = \frac{I_c}{kI^-} \quad .$$

After many shots without plasma, at various high power levels, it was determined that k is very near 0.85.

In the presence of plasma the loaded Q is thus

$$Q_\ell = \frac{I_c}{0.85I^-} \quad .$$

The series resistance of the antenna itself is given by solving for R_{ant} in the equation

$$Q_u = 100 = \frac{\frac{1}{2}\omega L I_c^2}{\frac{1}{2}I_c^2 R_{ant}} = \frac{\omega L}{R_{ant}} \quad .$$

For the Octupole antenna this turns out to be 96 mΩ.

To get the power absorbed by the plasma we measure I^- and I_c, and perform the following calculations:

$$Q_\ell = \frac{I_c}{.85I^-}$$

$$P_{diss} = \frac{\frac{1}{2}\omega L I_c{}^2}{Q_\ell} = \text{total dissipated power}$$

$$P_{ant} = \frac{1}{2}\, I_c^2\, R_{ant} = \text{Power dissipated by antenna}$$

$$P_{plasma} = P_{diss} - P_{ant} = \text{Power absorbed by plasma}$$

Finally to get the plasma radiation resistance,

$$R_{plasma} = \frac{2P_{plasma}}{I_c^2}$$

Typically the plasma spoils the Q to about 40-50% of its unloaded value. This means that about equal amounts of power go into the antenna losses and the plasma.

4.3 Loading Results

Using the experimental methods described in the previous section and the heating model presented in Chapter 3 a series of loading experiments was performed and compared with the heating theory.

Figure 4.5 shows how the loading varies with magnetic field strength. The separatrix density which varied only slightly (9.3×10^{12} cm^{-3}±10%) for the different field settings was divided out. Note that the magnetic field is expressed in terms of the charging voltage on the poloidal field capacitor bank. A setting of 5 kV corresponds to 0.72 Webers of flux in the machine and a magnetic field of 1.3 kG at the Faraday shield. The data were taken at a reduced RF power level of ~125 kW. The top theoretical curve is what one gets using the damping model with the vacuum electric field. That is the result if one assumed the plasma had no effect on the magnitude or polarization of the RF electric field. The second theoretical curve is the result taking into account the warm plasma effects for a value of α=8.6 cm. Alpha is the parameter that comes out of the theory and describes the k_z spectrum. The value of alpha used in the theoretical plot (8.6 cm) is equivalent to what is measured experimentally near the antenna (Fig. 4.3). Other values of alpha scale the theoretical curve roughly in the way indicated by Fig. 3.11. As discussed earlier, the RF shielding of E^+ has a weak temperature dependence. Since the ion temperature is observed to vary somewhat linearly with magnetic field (discussed below) this

Fig. 4.5 Loading dependence on poloidal magnetic field. Magnetic field expressed in volts on capacitor bank.

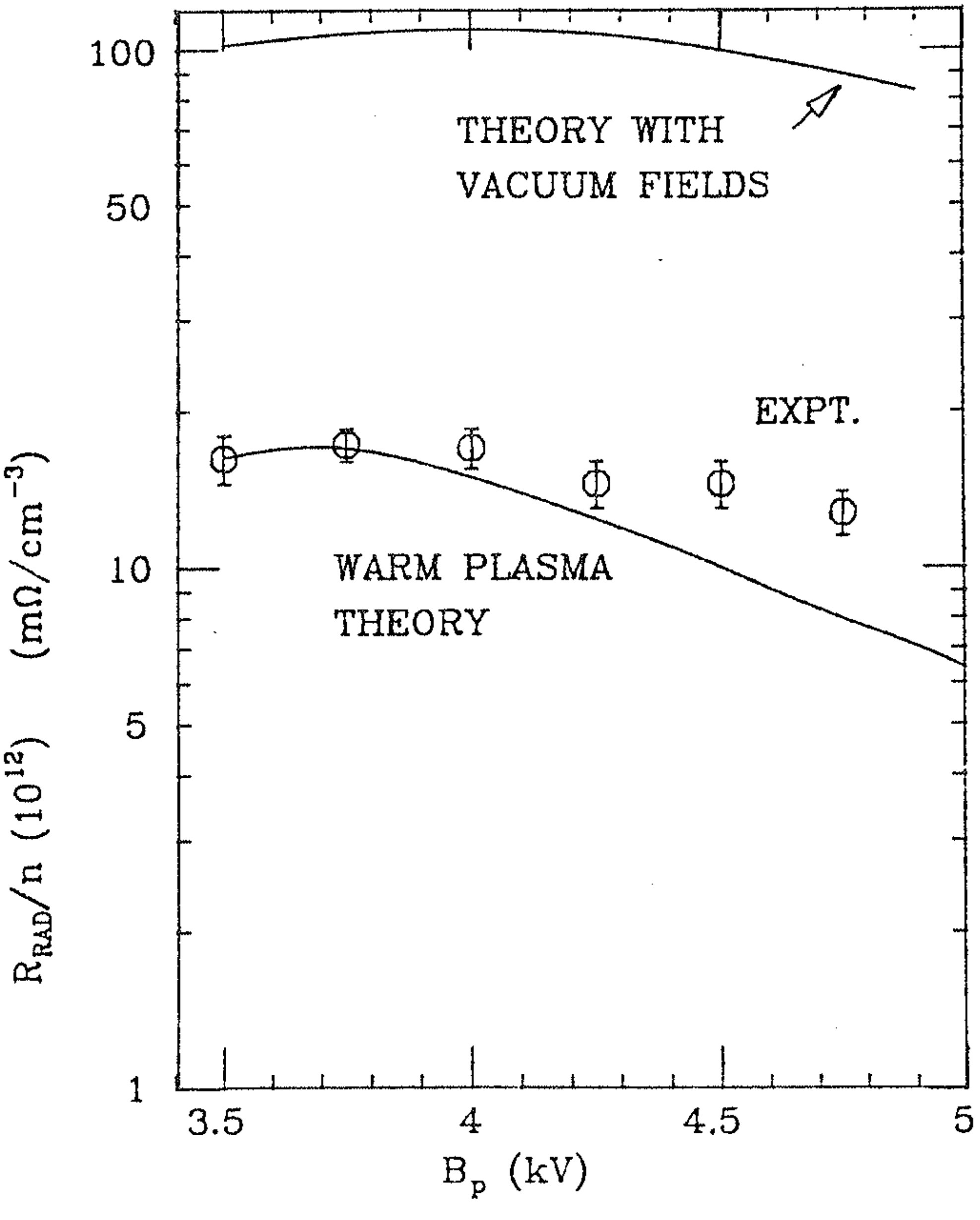
100
50
10
5
1
3.5
4
4.5
5
B_p (kV)
R_{RAD}/n (10^{12}) $(m\Omega/cm^{-3})$
THEORY WITH
VACUUM FIELDS
EXPT.
WARM PLASMA
THEORY

effect was put into the theoretical curve by having T_i vary from 75 eV at B_p=3.5 kV to 150 eV at B_p=5.0 kV. T_e was set to 40 eV for all fields. It turns out, however, because the plasma shielding effect has a weak temperature dependence, that putting in a B_p dependent ion temperature had only a small effect on the shape of the theoretical curve. As discussed in the previous chapter the warm plasma slab model predicts by how much the left-hand component of the electric field is attenuated at the midcylinder, z=0. The manner in which the slab model was interfaced to the complicated Octupole field geometry was described in Chapter 3. To lowest order, the loading is independent of magnetic field, because as the resonance zone is moved closer to the antenna, the RF electric field strength increases, but the density at the resonance zone decreases. Since the loading goes as the product $n|E^+|^2$, these effects tend to cancel. However, when the warm plasma effects are included, we see that the attenuation from the vacuum solution is greater at the higher fields and departs by a greater amount from the experiment than the low field results. From Fig. 3.11 we see that the warm plasma model predicts that the shielding of the left-hand component is more complete at the higher densities. Therefore, since the resonance zone is in regions of higher density for the higher magnetic fields, the warm plasma correction is more severe at those fields, giving the theory curve the observed shape.

One possible explanation for the qualitative difference in the theoretical and experimental curves goes as follows. At the higher field settings the resonance zone is in a region of greater magnetic field line curvature which means a greater departure from the slab model approximation. Whereas in the slab approximation energy must propagate across field lines directly from the antenna to the resonance zone, in the Octupole, energy can be transmitted to the resonance zone near the center of the machine along field lines that curve down past the sides of the antenna. This effect is not treated in the slab model. There are also other resonance broadening effects that occur with field line curvature. For example, an ion that moves along a field line from underneath the ring where the RF electric field is weak, to near the shield (closest distance between the field line and antenna), and then up towards the midcylinder, feels extra parallel gradients in the electric field that enhance the doppler effect over the slab approximation. At the lower field settings in Fig. 4.5 the resonance zone is closer to the antenna where the mirror ratio is weaker and the slab model is a better approximation.

Figure 4.6 shows how the loading scales with density for a constant magnetic field setting of 4.5 kV on the poloidal magnetic field capacitor bank which corresponds to a field of 1.12 kG at the Faraday shield. Again we include the theoretical result using the vacuum fields which scale linearly with density as indicated by Eq. (3.33). It is interesting to note that the experimental data

Fig. 4.6 Loading dependence on density.

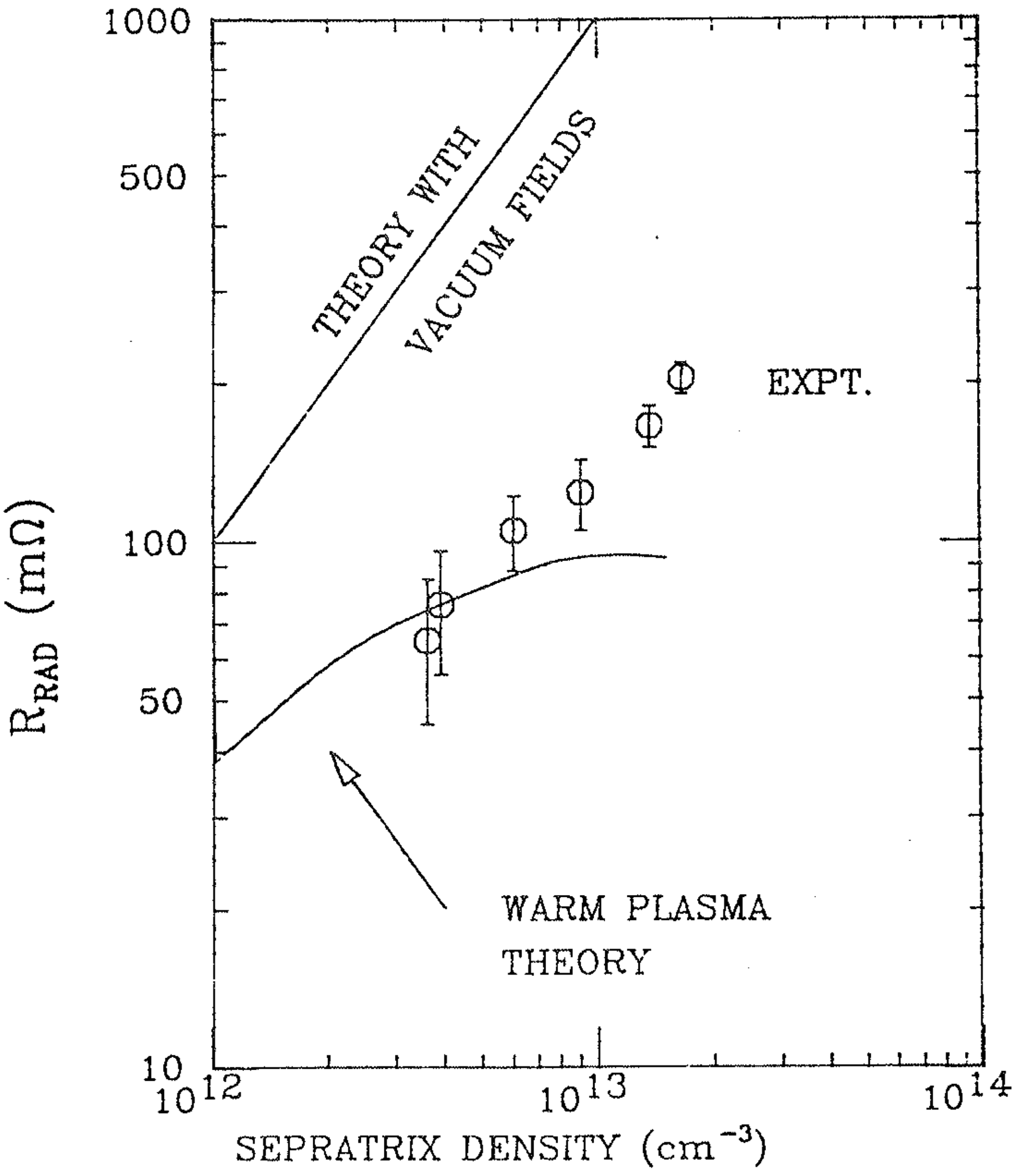
1000
500
100
50
10
R_{RAD} (mΩ)
10^{12}
10^{13}
10^{14}
SEPRATRIX DENSITY (cm^{-3})
THEORY WITH
VACUUM FIELDS
EXPT.
WARM PLASMA
THEORY

scale less than linearly with density, more like $n^{0.7}$. This is in qualitative agreement with the observation that the plasma shielding of E^+ is more complete as the density increases. The theoretical curve with the warm plasma correction is for α=8.6 cm, T_i=150 eV, and T_e=40 eV. The theoretical plot shows the loading starting to saturate at the higher densities, whereas the experimental data continue to rise. Other coupling mechanisms besides ion cyclotron damping, such as excitation of electrostatic ion cyclotron waves near the perpendicular ion cyclotron resonance and/or fast waves, may become important at the higher densities.

Figure 4.7 shows how the loading scales with power for a nearly constant separatrix density of 8.5×10^{12} cm^{-3}. Over an order of magnitude in coupled power, the loading is measured to be nearly constant within the error bars. Any temperature dependence in the loading would not necessarily show up in the range of the coupled power that is graphed because of the relatively weak variation (~50%) of the $|E^+|^2$ attenuation with temperature in the range of 50-250 eV.

4.4. The Standard Shot

RF target plasmas were usually made with the intermediate density gun. The initial turbulence from gun injection damps away in the first few hundred microseconds leaving a plasma with a $0.9-1.5\times10^{13}$ cm^{-3} density and $T_i \approx T_e \approx 20$ eV. A typical shot is shown in Fig. 4.8. The RF is turned on simultaneously with gun injection

Fig. 4.7 Loading dependence on RF power.

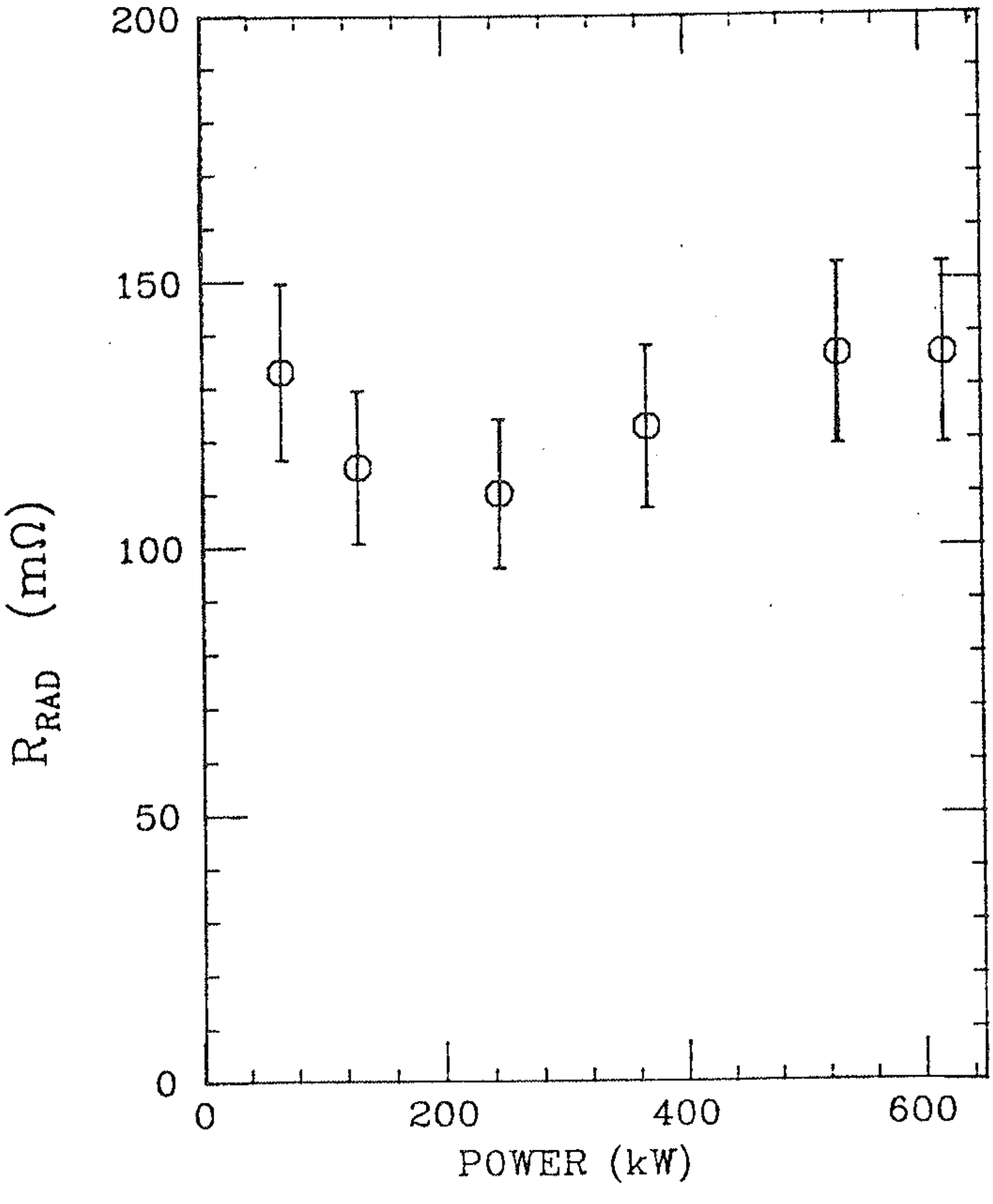
200
150
100
50
0
R_{RAD} (mΩ)
0
200
400
600
POWER (kW)

Fig. 4.8 Typical shot. Ion temperature measured with charge exchange analyzer, electron temperature with Langmuir probe, and density measured with microwave interferometer.

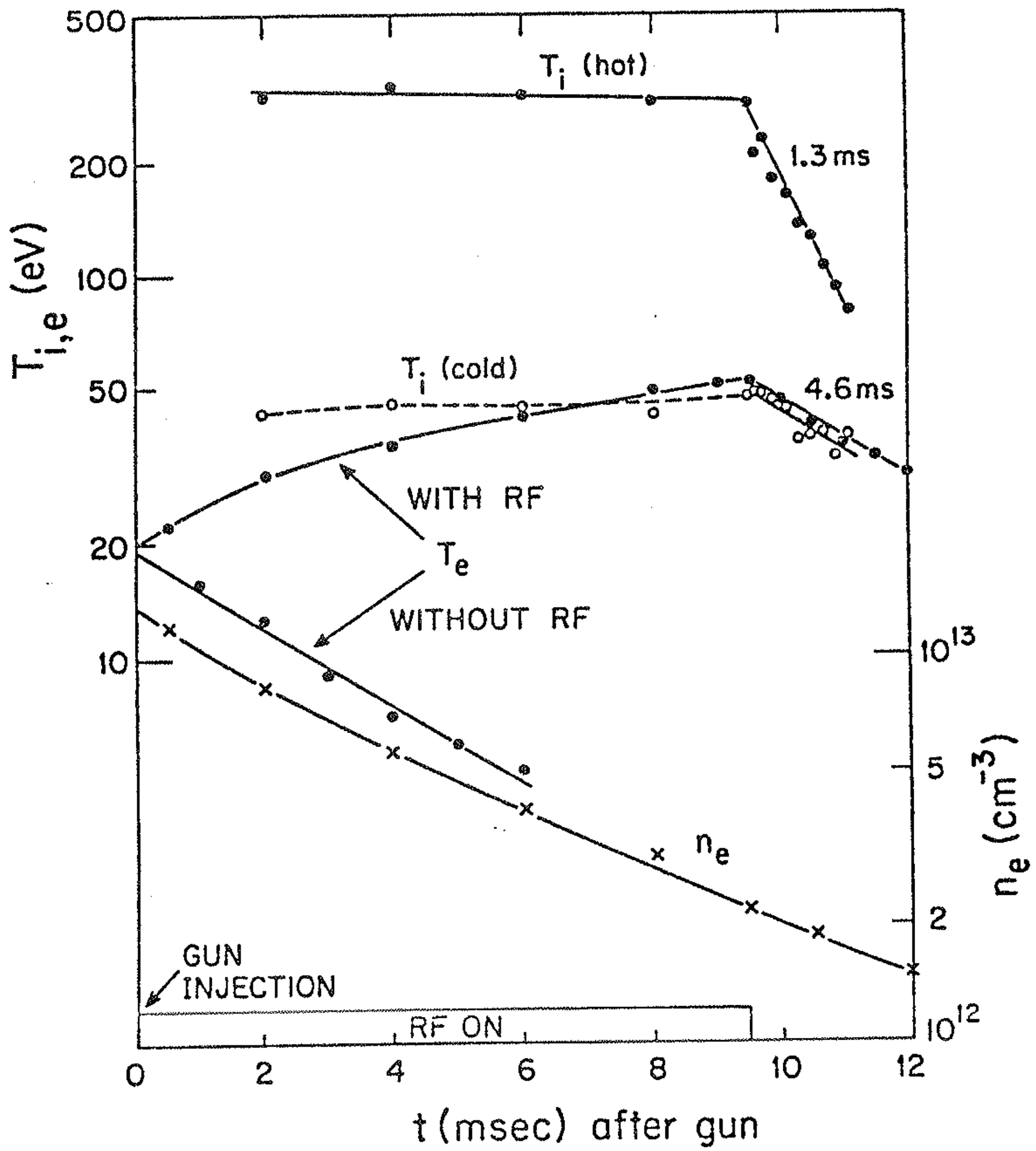
500
200
100
50
20
10
$T_{i,e}$ (eV)
T_i (hot)
1.3 ms
T_i (cold)
4.6 ms
WITH RF
T_e
WITHOUT RF
n_e
10^{13}
5
2
10^{12}
n_e (cm^{-3})
GUN INJECTION
RF ON
0
2
4
6
8
10
12
t (msec) after gun

and turned off 9.5 msec into the shot. Though the pulse forming network was designed to deliver a 10 msec pulse the leading edge of the reflection occurs at 9.5 msec, and so we crowbar 0.5 msec early in order to maintain a somewhat constant power level throughout the RF pulse.

The ion temperatures in Fig. 4.8 were measured with the charge exchange analyzer. By 2 msec into the shot, a hot tail appears which for this case (B_p=4.5 kV) is 300 eV. Assuming infinite energy confinement, we can calculate the absolute maximum rise in temperature for a given density, power, and time.

$$P_{rf} \times \frac{1}{n\mathrm{Vol.}} \times \mathrm{Time} = \Delta T_i \text{ eV/particle}$$

For 500 kW and a plasma volume of 6 m^3 this gives

$$\Delta T_i \approx \frac{500\ T(\mathrm{msec})}{n(10^{12}\mathrm{cm}^{-3})} \text{ eV/particle} \quad .$$

For a ~300 eV rise in T_i after 2 msec this puts an upper limit of ~$3\times10^{12}(\mathrm{cm}^{-3})$ on the hot ion density or approximately one-third of the total ion density. The actual hot ion fraction is probably considerably lower than this at 2 msec into the shot. The charge exchange analyzer also indicates a bulk temperature near 50 eV.

It has been observed that the electron temperature is very sensitive to machine cleanliness. The shot shown in Fig. 4.8 shows T_e for a "clean" machine. During several days of running RF discharges with no vacuum accidents, the electron temperature will start out at 20 eV and steadily rise until it equilibrates with the bulk ions as indicated in Fig. 4.8. For a dirty machine the electron temperature will fall for the first few milliseconds due to the high impurity concentration and then recover as the low Z impurities start to burn out. This is shown in Fig. 4.9. Note from Fig. 4.8 that without RF the initial 20 eV plasma decays with temperature and density decay times of ~5 msec.

In Fig. 4.8, which is a high power shot, the curve showing the density behavior looks very similar to that of a non-RF heated plasma. The initial conclusion would be that the RF does not effect the overall particle confinement; however, that turns out not to be the case. Figure 4.10 shows density for various charging voltages on the pulse forming network (PFN). The voltage on the PFN is proportional to the antenna voltage or the square root of the RF power. At lower power levels the density is higher than without RF, indicating enhanced reflux. As the power is raised, the density starts dropping in the middle of the shot, and the interferometer trace starts to look more normal. Apparently there are two competing processes. Plasma particle confinement is worse with RF, but at the lower power levels the enhanced reflux gives rise to a

Fig. 4.9 Electron temperature time evolution for a dirty machine.

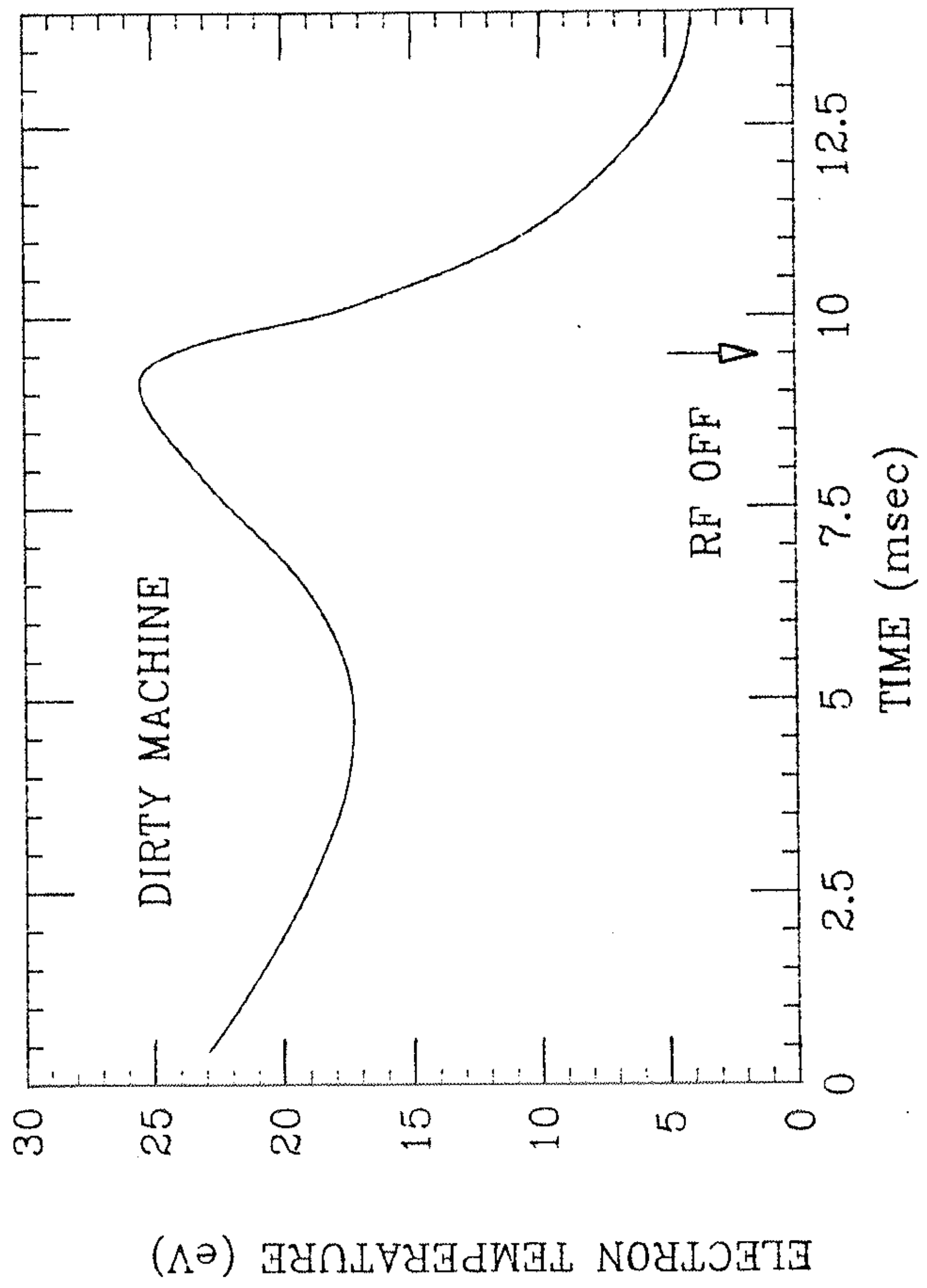
DIRTY MACHINE
RF OFF
TIME (msec)
ELECTRON TEMPERATURE (eV)
0
2.5
5
7.5
10
12.5
0
5
10
15
20
25
30

Fig. 4.10 Interferometer signal is RF power dependent.

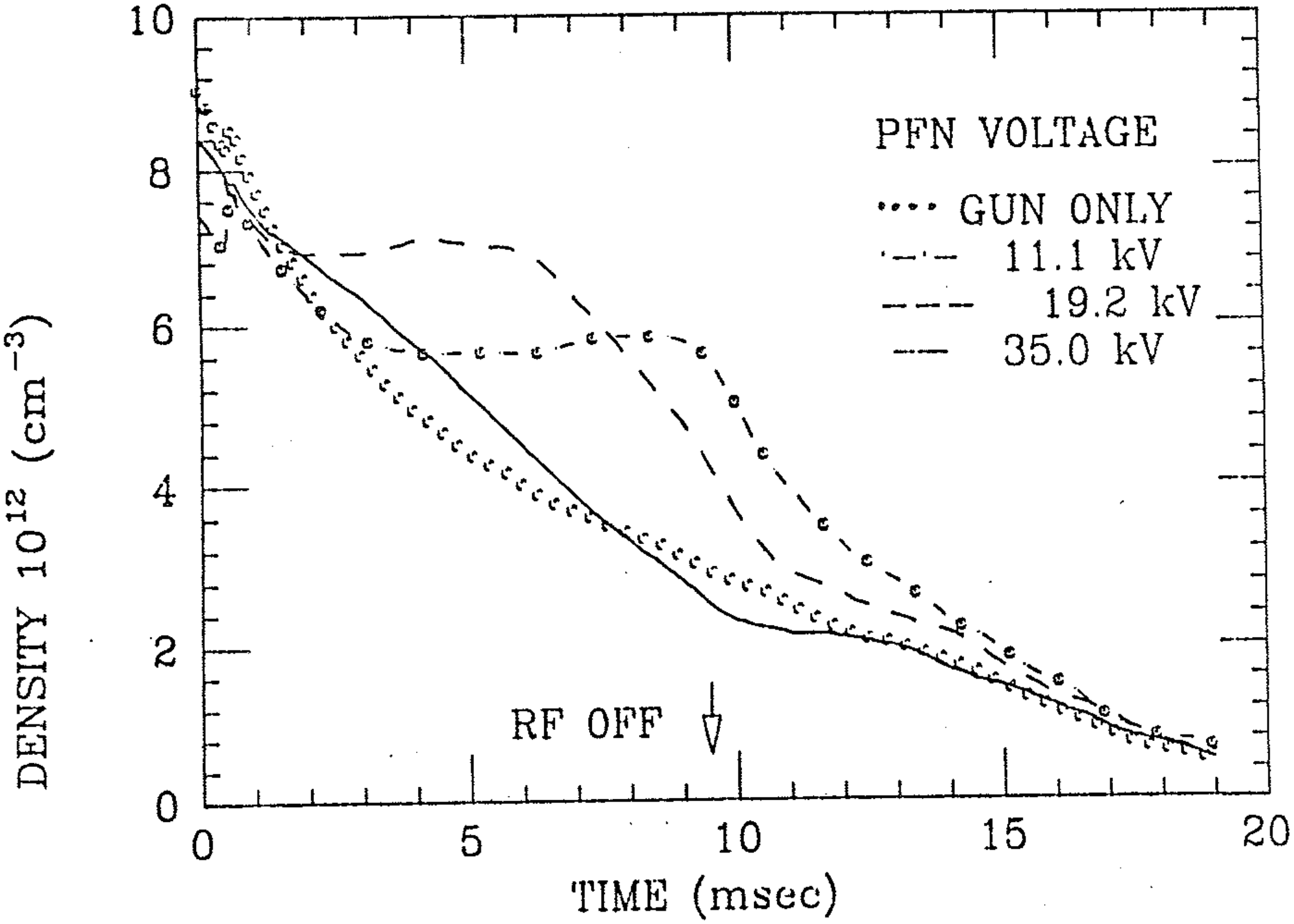
PFN VOLTAGE
GUN ONLY
11.1 kV
19.2 kV
35.0 kV
RF OFF
DENSITY 10^{12} (cm^{-3})
TIME (msec)
0
2
4
6
8
10
0
5
10
15
20

net increase in density. As the power is raised, plasma is being lost at a rate fast enough to just cancel the incoming cold hydrogen gas and impurities.

4.5 Ion Confinement Studies

The hot ion temperature is strongly dependent on magnetic field strength as illustrated in Fig. 4.11. The abscissa is the magnetic field at the antenna. It is interesting to compare these data with Fig. 4.5 which shows that the loading is only weakly dependent on magnetic field. Therefore, the ion temperature dependence on magnetic field must be related to confinement rather than input power. For all the cases in Fig. 4.11 the hot ion temperature is reached early in the RF pulse ($\lesssim 3$ msec) and then remains clamped at that value. This seems to suggest some gyroradius limit which is truncating the distribution function at a few keV and thus limiting the temperature. For example, for the standard case of 4.5 kV on the poloidal field bank and f=1.25 MHz, the poloidal field at the shield is 1.12 kG, and the resonance zone (0.822 kG) is 9 cm above the shield. The formula relating field, gyroradius, and energy is

$$\rho(\text{cm}) = 145\,\sqrt{E(\text{eV})}/B\ (\text{Gauss}) \quad .$$

For this particular case if we impose a 9 cm gyroradius limit for an ion in a 0.822 kG field then the temperature limit would be 2.6 keV. The actual limit will be somewhat higher than this because the ion feels some stronger average field between the resonance zone

Fig. 4.11 Ion temperature dependence on poloidal magnetic field. Magnetic field expressed in kG at the antenna.

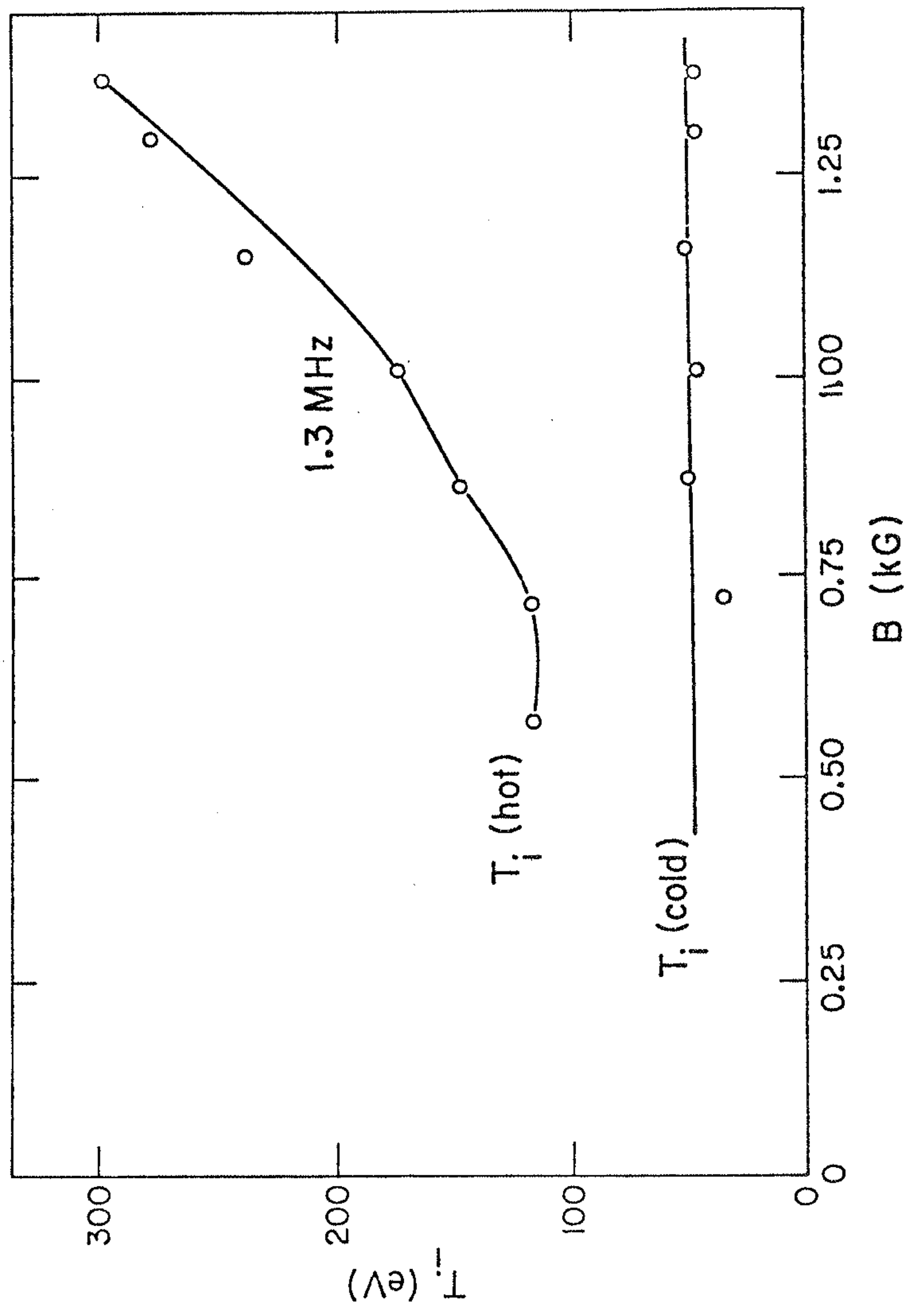
1.3 MHz
T_i (hot)
T_i (cold)
T_i (eV)
0
100
200
300
B (kG)
0
0.25
0.50
0.75
1.00
1.25

(0.822 kG) and the shield (1.12 kG). That average in this case is 0.97 kG, imposing a limit of 3.6 keV. As the field is lowered the resonance zone moves closer to the shield, and so the gyroradius limit becomes smaller along with the energy limit which goes as the square of the gyroradius. Truncation of the energy distribution function at high energies (>2 keV) has not been observed because the charge exchange signal becomes too small (noisy). Another possibility for the hot ion temperature dependence on magnetic field is that at the higher fields with the resonance zone farther from the lid, the neutral density there will be lower, yielding a lower charge exchange rate. However, it has been observed that the hot ion temperature is fairly independent of changes in gettering and thus hydrogen reflux rate. Another possibility is an anomalous B dependent radial transport. It is not well understood why the hot ion temperature is dependent on magnetic field whereas the loading is not.

Figure 4.12 shows how the ion temperature varies with density. Notice that in the 10^{12} cm^{-3} range of densities the hot ion temperature stays fairly constant. At very low densities ($<5\times10^{11}$), hot tails of several hundred eV are observed, with a 1 keV tail measured at 1.0×10^{11} cm^{-3}. It is not understood how these very hot tails can exist and still have the gyroradius limit be the correct explanation for the clamping of the hot ion temperature at the higher densities. The electrons and cold ions stay fairly well coupled over the density range investigated.

Fig. 4.12 Ion temperature dependence on density.

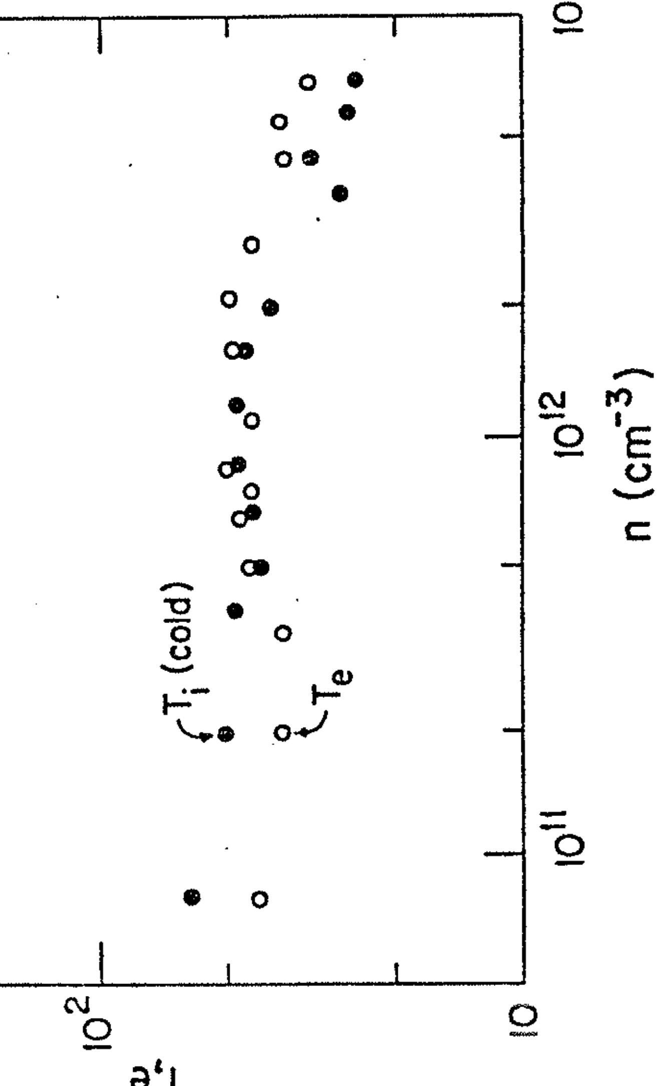
$T_{i,e}$ (eV)
10^3
10^2
10
10^{11}
10^{12}
10^{13}
n (cm^{-3})
T_i (hot)
T_i (cold)
T_e

Estimates of the absolute power being lost through charge exchange can be obtained with the charge exchange analyzer. An absolute calibration was made by Strait along with detailed calculations on the solid angle viewed by the charge exchange analyzer. Presented below is a short explanation on how an estimate of charge exchange power is obtained.

The charge exchange signal in volts is given by

$$S(E) = [\int n_0 n_i d\ell]\sigma(E)vf(E)\delta(E)\eta(E)\frac{u}{4\pi}G$$

where $\int d\ell$ is an integral along the line of sight of the analyzer and,

n_0 = neutral density

n_i = ion density

$\sigma(E)$ = charge exchange cross-section

v = proton velocity

$f(E)$ = ion energy distribution function

$\delta(E)$ = energy bandwidth of analyzer

$\eta(E)$ = stripping cell efficiency

u = product of analyzer's slit area and solid angle

G = gain of Daly detector (volts/particle).

To get a curve that only has the exponential energy dependence we plot

$$F(E) = S(E)/\sigma v E^{3/2} \eta \frac{E+V_a}{E}$$

where V_a is the pre-acceleration energy or stripping cell bias voltage. We´ve also used the relation[4] for the energy bandwidth

$$\frac{\delta E}{E+V_a} = \frac{\Delta S}{R_o}$$

where ΔS is the analyzer slit width and R_o the radius of the deflector plates center line. The E=0 intercept is

$$F_o = \int n_o n_i d\ell \frac{2}{\sqrt{\pi}} T^{-3/2} \frac{\delta E}{E+V_a} \frac{u}{4\pi} G$$

The quantities u, G, and $\delta E/E+V_a$ were measured by Strait, F_o is read off the F(E) plot, and T_i is obtained from the inverse slope. Therefore, we now have an expression for $\int n_o n_i d\ell$ which we can use to calculate charge exchange power. Note that we don´t need (and don´t have) n_o and n_i separately, and so the question of the relative population of each ion component is avoided. Assuming a thin plasma, so that n_o is constant, the charge exchange power per unit volume is

$$\frac{dP}{dV} = n_o n_i \int_o^\infty \sigma(E) v E f(E) dE \;\alpha\; n_o n_i T^{4/3}$$

For a density profile of the form

$$n_i = n_{io}e^{-\left(\frac{\psi-\psi_s}{\sigma}\right)^2}$$

an effective volume is calculated from

$$\int e^{-\left(\frac{\psi-\psi_s}{\sigma}\right)^2} \frac{dV}{d\psi}\, d\psi$$

where $dV(\psi)/d\psi$ has been evaluated by Ehrhardt[5] and Morin.[6] This effective volume multiplies df/dV to get an estimate for the charge exchange power. Figure 4.13 shows how the charge exchange power measured by this method scales with input RF power. Most of the charge exchange power comes from the hot component, and for the typical shots with ~500 kW of RF power we measure about half of that coming out as charge exchange neutrals.

Figure 4.14 shows how the ion temperature as measured with the charge exchange analyzer varies with RF power. Though the hot ion temperature rises only a factor of two over an order of magnitude in coupled power, the charge exchange analyzer indicates that the hot ion fraction is increasing. The cold component stays constant with power indicating that the bulk of the ions is coupled closely to the cold electrons.

Fig. 4.13 Estimated charge exchange power as measured with charge exchange analyzer.

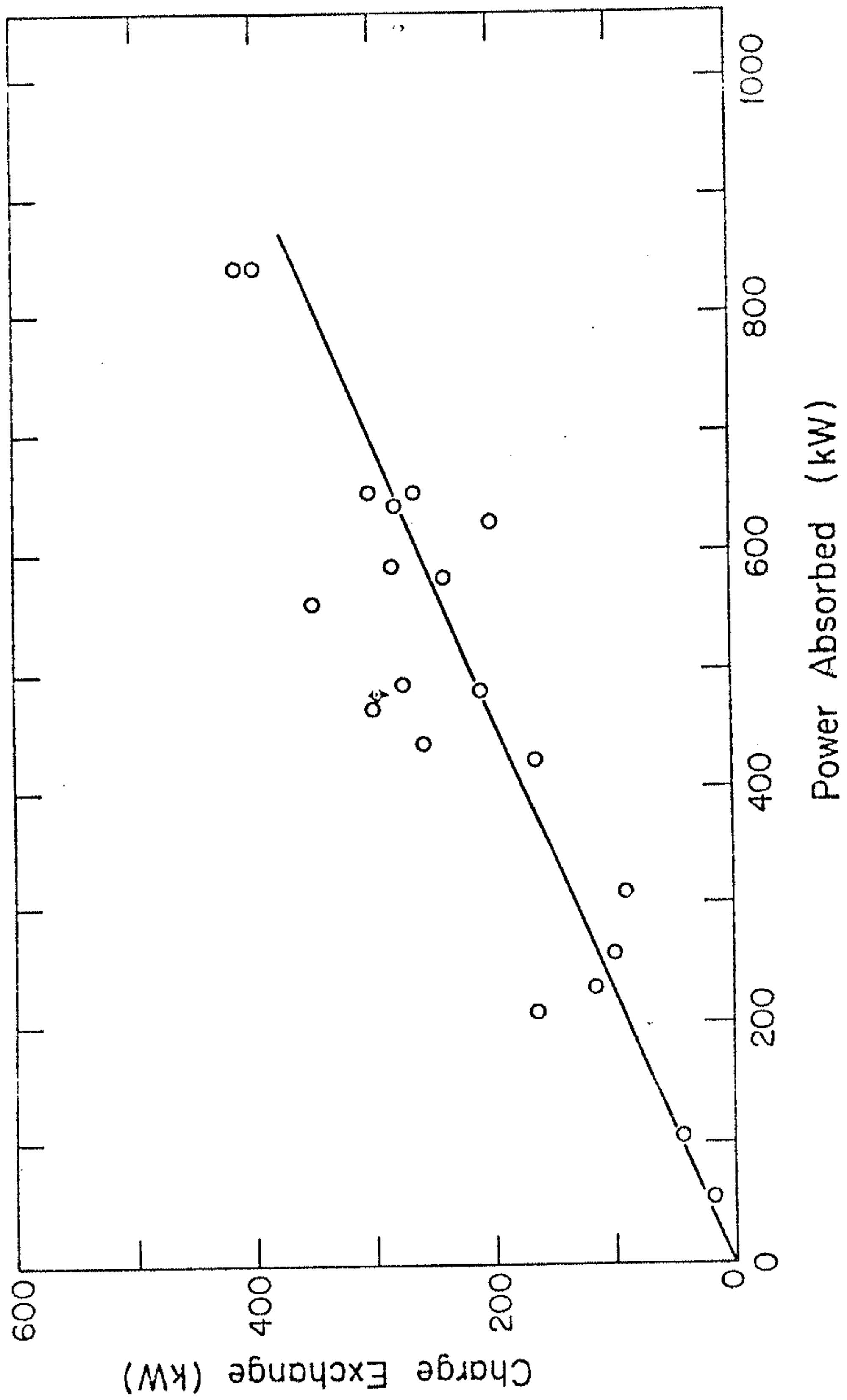
Charge Exchange (kW)
600
400
200
0
Power Absorbed (kW)
0
200
400
600
800
1000

Fig. 4.14 Ion temperature dependence on RF power.

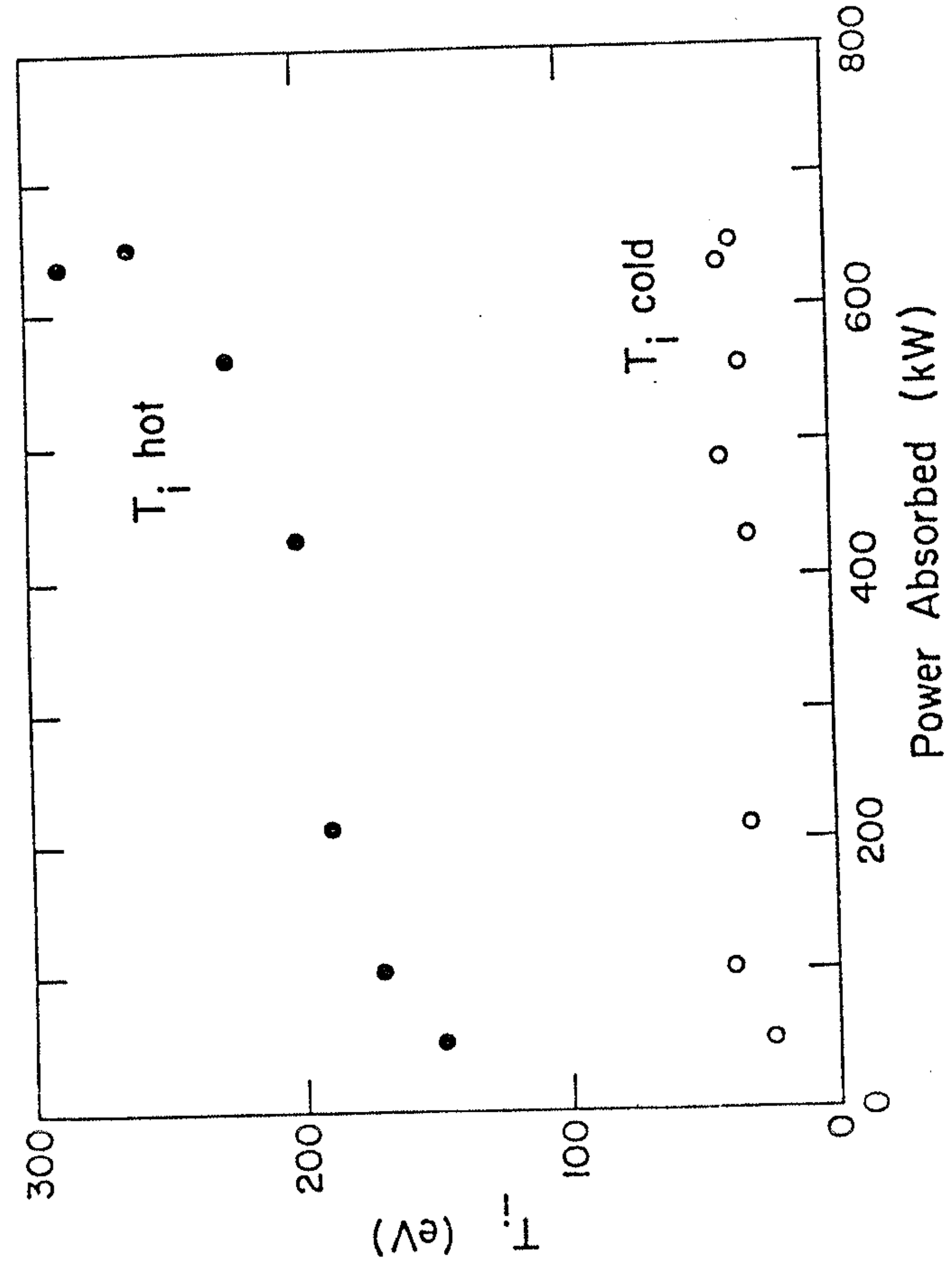
T_i hot
T_i cold
T_i (eV)
0
100
200
300
Power Absorbed (kW)
0
200
400
600
800

A gridded ion energy analyzer was used to investigate ion temperature profiles. Profiles were taken in the bridge region azimuthally away from the antenna. Therefore, ions heated over the antenna drift toroidally, and move along field lines poloidally, in order to reach the probe. An example of the time evolution of the ion and electron temperatures on a particular flux surface is shown in Fig. 4.15. For this plasma, the machine was fairly dirty, and thus the electron temperature was low. Note the ion temperature stays flat for a few milliseconds before it starts to rise nicely during the second half of the RF pulse. $T_{i\perp}$ and $T_{i\parallel}$ are well coupled indicating an isotropic velocity distribution in the bridge region. The saturation current measured in the same region with a Langmuir probe was flat during most of the RF pulse. The T_i, T_e, and J_{sat} profiles near the end of the RF pulse are shown in Fig. 4.16. The saturation current peaks on the separatrix (ψ=5.75), as it usually does in non-RF heated plasmas, but the ion temperature peaks off the separatrix. The ion temperature peaks in the common flux region at $\psi \approx 6.5$ which is the flux surface that crosses the resonance zone near the antenna. (The flux surface that is tangent to the bottom of the resonant mod-B surface for this case is ψ=6.8.) The effect of the heat source in the common flux region is also evident in the electron temperature profile which shows T_e greatest towards the edge. Further discussion of the electron temperature profile is given in the next section.

Fig. 4.15 Time evolution of plasma temperature and ion saturation current as measured on flux surface ψ=6.2 in the bridge.

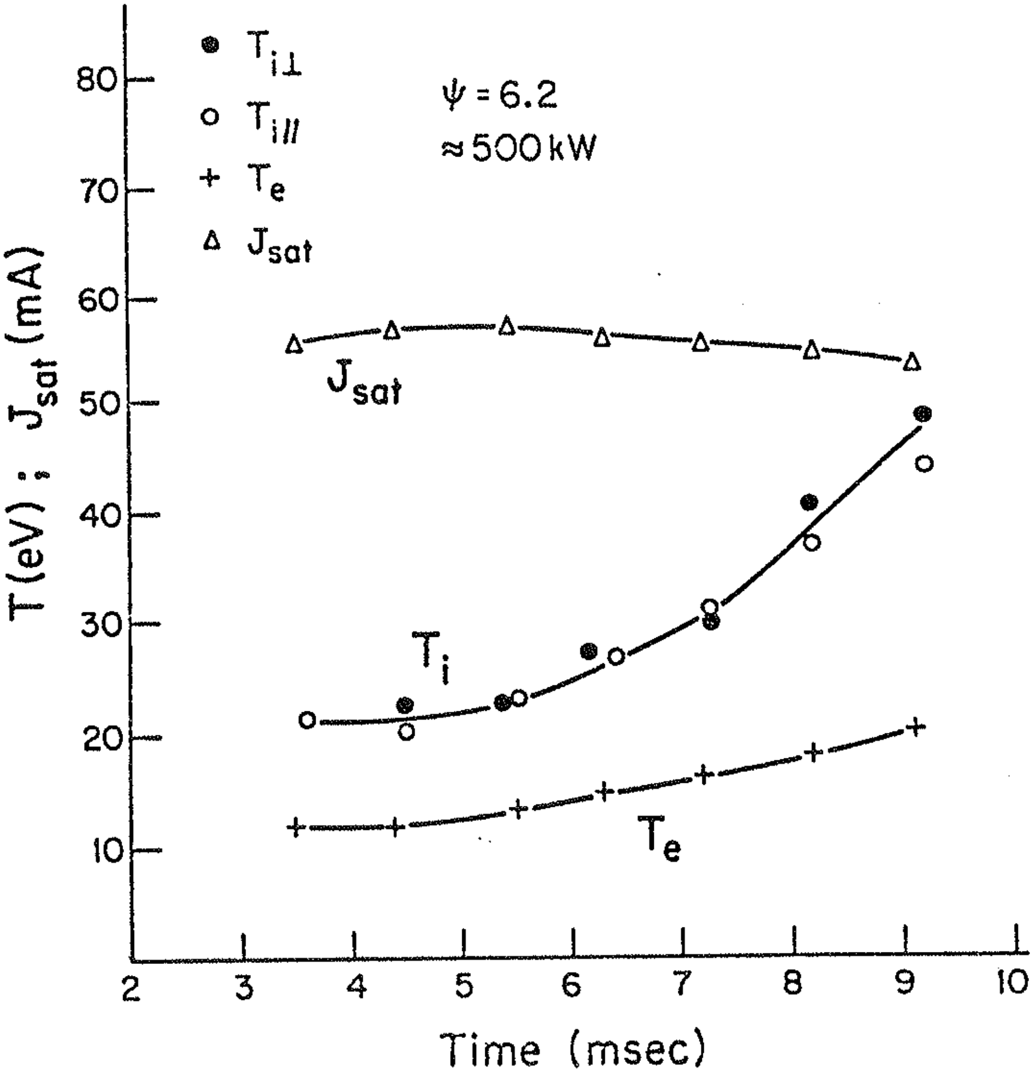
● $T_{i\perp}$
○ $T_{i\parallel}$
+ T_e
△ J_{sat}
$\psi = 6.2$
≈500 kW
J_{sat}
T_i
T_e
T (eV) ; J_{sat} (mA)
80
70
60
50
40
30
20
10
2
3
4
5
6
7
8
9
10
Time (msec)

Fig. 4.16 Profiles in the bridge region. Ion temperature obtained with gridded ion energy analyzer probe.

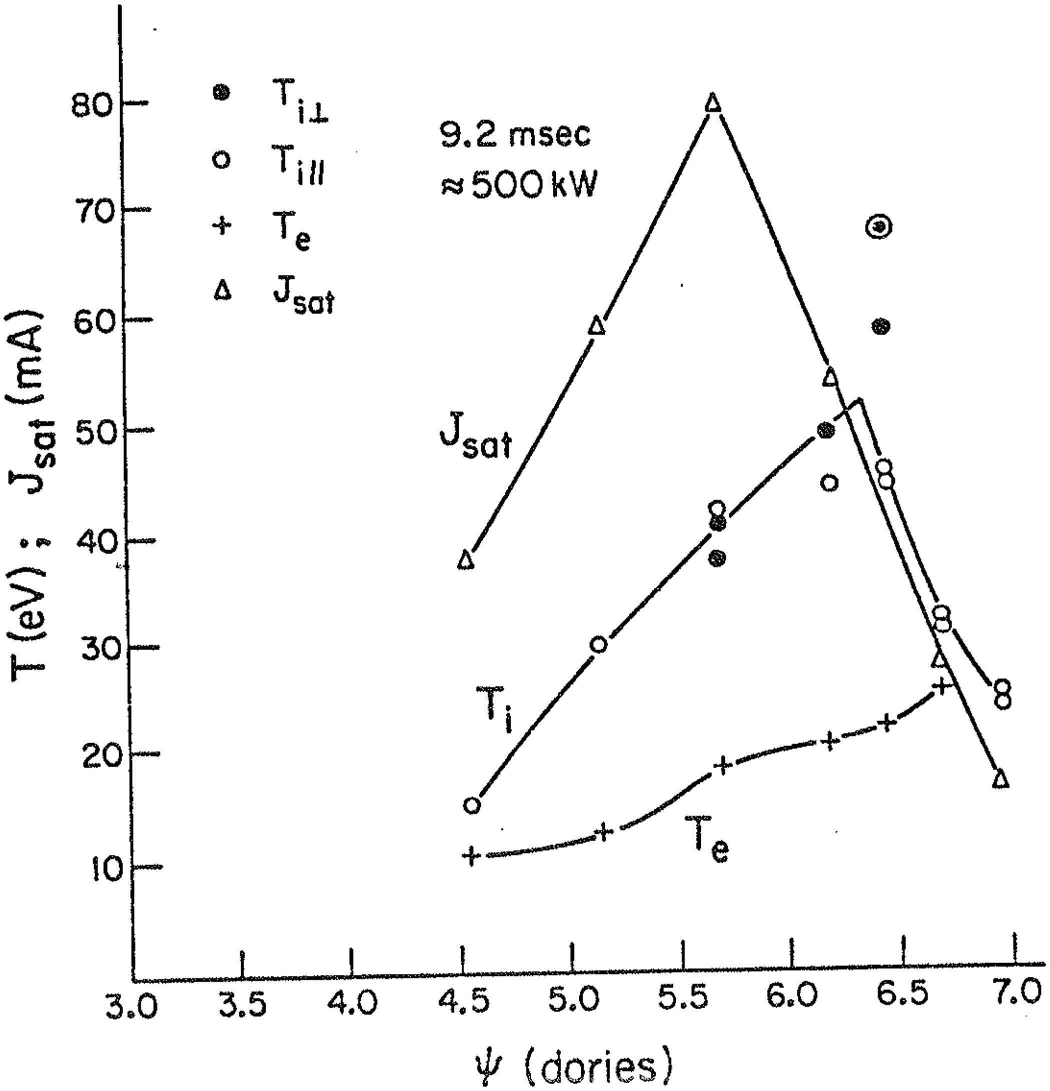
● $T_{i\perp}$
○ $T_{i\parallel}$
+ T_e
△ J_{sat}
9.2 msec
≈500 kW
J_{sat}
T_i
T_e
T (eV) ; J_{sat} (mA)
80
70
60
50
40
30
20
10
3.0
3.5
4.0
4.5
5.0
5.5
6.0
6.5
7.0
ψ (dories)

4.6 Electron Confinement Studies

As stated earlier, the electron temperature is observed to be very sensitive to machine wall conditions. Figure 4.17 shows that 30%-40% increases in T_e are made by turning up the getters. It has been observed that one signature of a clean machine is T_e rising monotonically in time during a shot. A dirty machine, even at full RF power, will have T_e fall from the initial 15-20 eV during the first few milliseconds of the RF pulse before starting to climb. T_e rises about linearly with power as indicated in Fig. 4.18. These temperatures are reached at the end of the RF pulse when the density is $\lesssim 4\times10^{12}$ cm^{-3} and the machine is clean.

An interesting electron temperature profile, illustrated in Fig. 4.19, was measured at reduced RF power on the midcylinder directly above the antenna. The separatrix is at $\psi=5.7$, and the Faraday shield is near $\psi=8$. The electron temperature peaks at about $\psi=6.8$ which is in the region of flux space that crosses the resonance zone near the antenna and therefore the region where most of the ion heating is expected to occur. In fact, Fig. 4.19 shows the same qualitative structure as the ion temperature profile, Fig. 4.16, taken in the bridge.

Some experiments to try and estimate the power being lost from the electrons by impurity radiation were performed using the bolometer (Section 2.4.6), also called a thinistor. The thinistor measures the time integrated incident energy, and the slope of the signal when plotted versus time gives an indication of the radiated

Fig. 4.17 Effect of gettering on electron temperature.

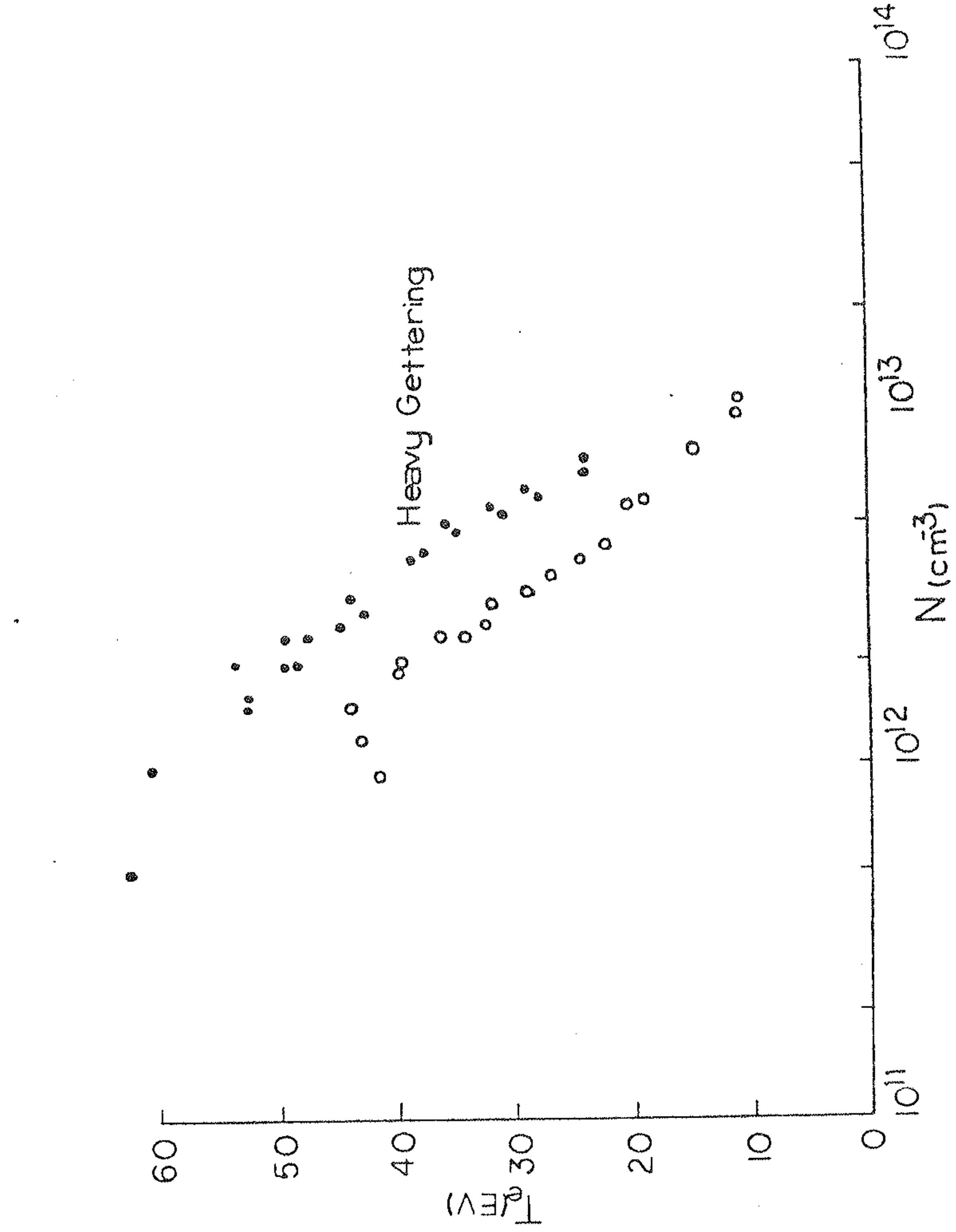
Heavy Gettering
T_e(EV)
60
50
40
30
20
10
0
10^{11}
10^{12}
10^{13}
10^{14}
N (cm^{-3})

Fig. 4.18 Electron temperature at end of RF pulse rises with RF power.

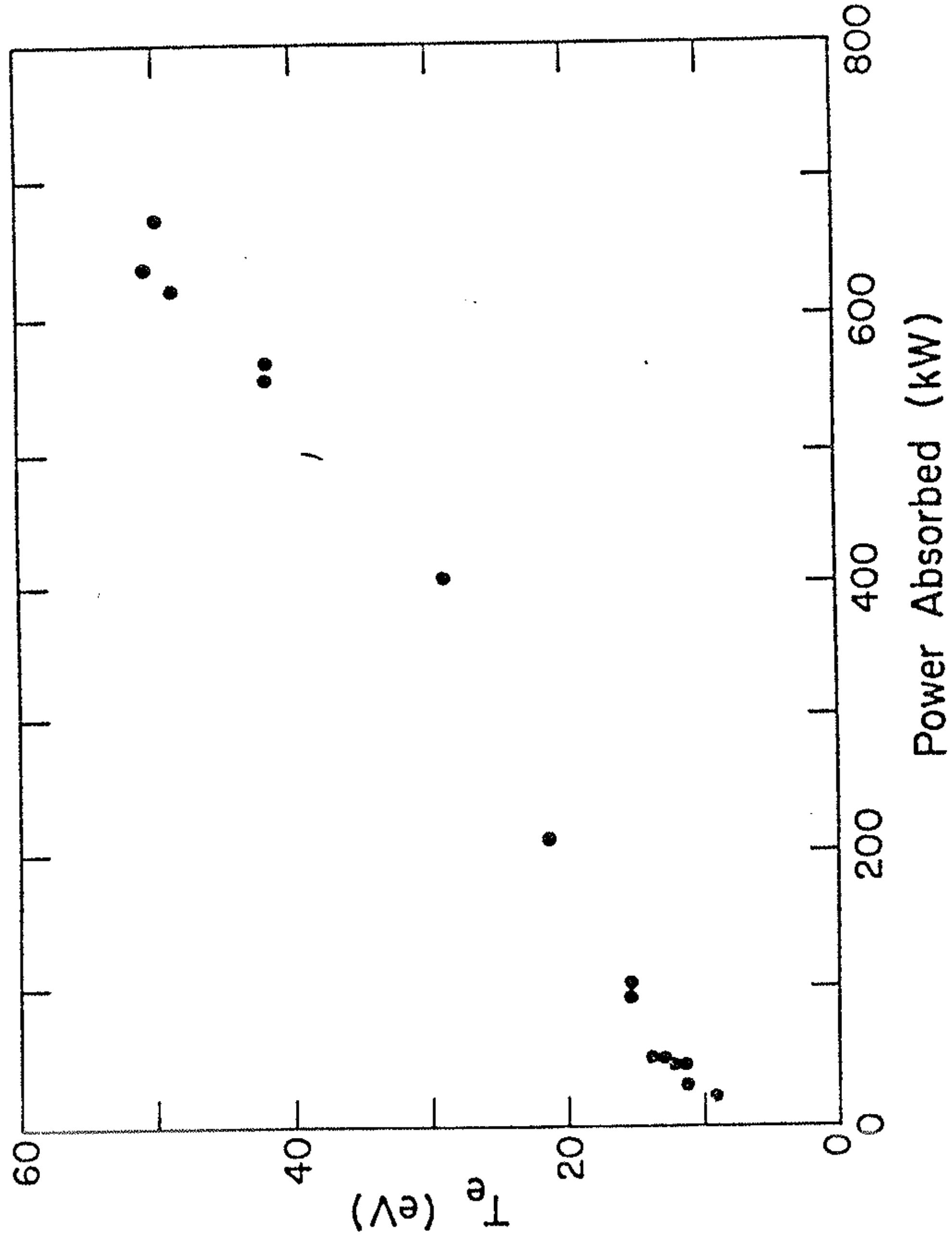
T_e (eV)
0
20
40
60
Power Absorbed (kW)
0
200
400
600
800

Fig. 4.19 Electron temperature profile taken on the midcylinder above the antenna. Temperature peaks off the separatrix in the vicinity of the ion cyclotron resonance.

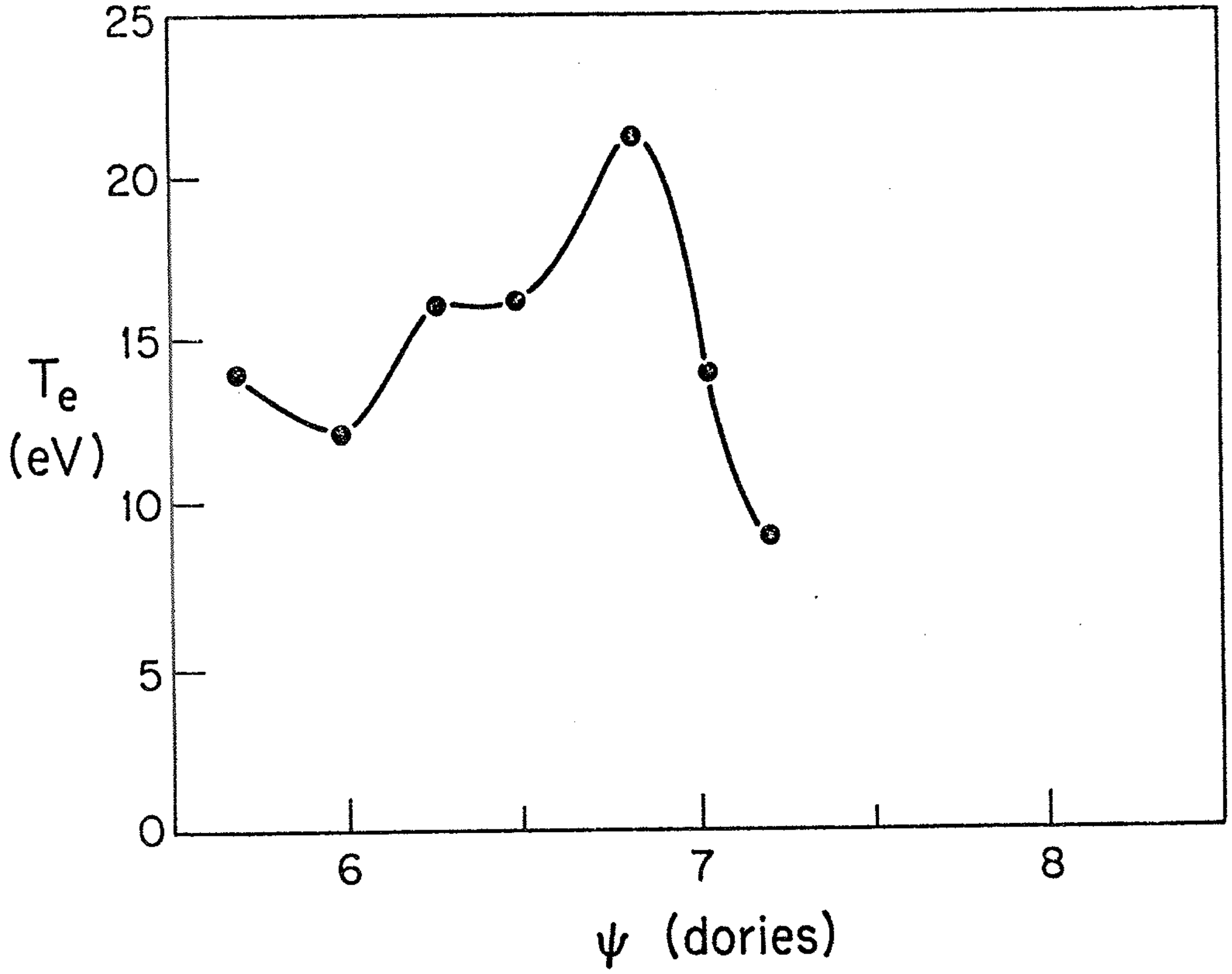
25
20
15
10
5
0
T_e
(eV)
6
7
8
ψ (dories)

power. Figure 4.20 shows T_e and the thinistor signal as functions of time under clean machine conditions. It appears that at ~3 msec there is a change in the slope of the thinistor signal indicating a decrease in the radiated power, perhaps due to the burning through of some impurity. At about the same time the electron temperature starts rising more rapidly indicating that T_e is correlated with the thinistor signal.

A nitrogen doping experiment was performed to get an estimate of the radiated power. Figure 4.21 shows the thinistor signal at the end of the RF pulse for various levels of N_2 doping. The experiment was performed under clean machine conditions with T_e staying fairly constant (43±5 eV) for all doping levels. Therefore, the measured NIII emission can be taken as a measure of the nitrogen concentration. The point labelled no doping is with RF, and the nitrogen source is just the walls. As the doping level is increased, the thinistor signal rises and nearly saturates. An upper limit on the total radiated power is obtained by assuming that the signal saturated because all the RF input power is leaving as radiation. Therefore, the no doping case, which is half the saturated value, would represent no more than half the RF input power. The conclusion is that radiation accounts for no more than half the input power when the machine is clean.

Fig. 4.20 Thinistor signal shows that radiated power level decreases slightly during the shot. Electron temperature time dependence appears correlated with thinistor signal.

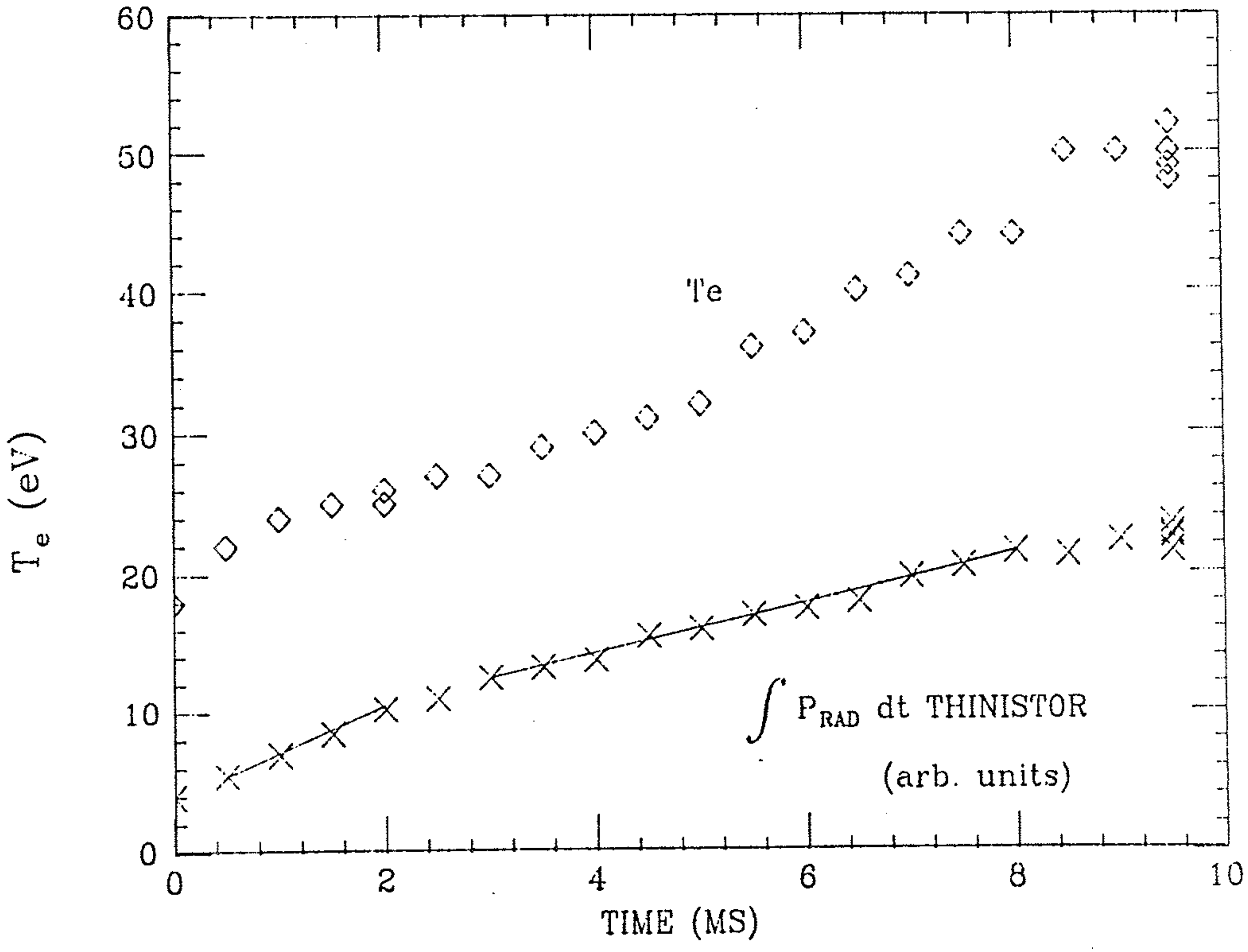
60
50
40
30
20
10
0
T_e (eV)
0
2
4
6
8
10
TIME (MS)
Te
$\int P_{RAD}\,dt$ THINISTOR
(arb. units)

Fig. 4.21 Results of nitrogen doping experiment. Radiated power saturates at twice the no doping level.

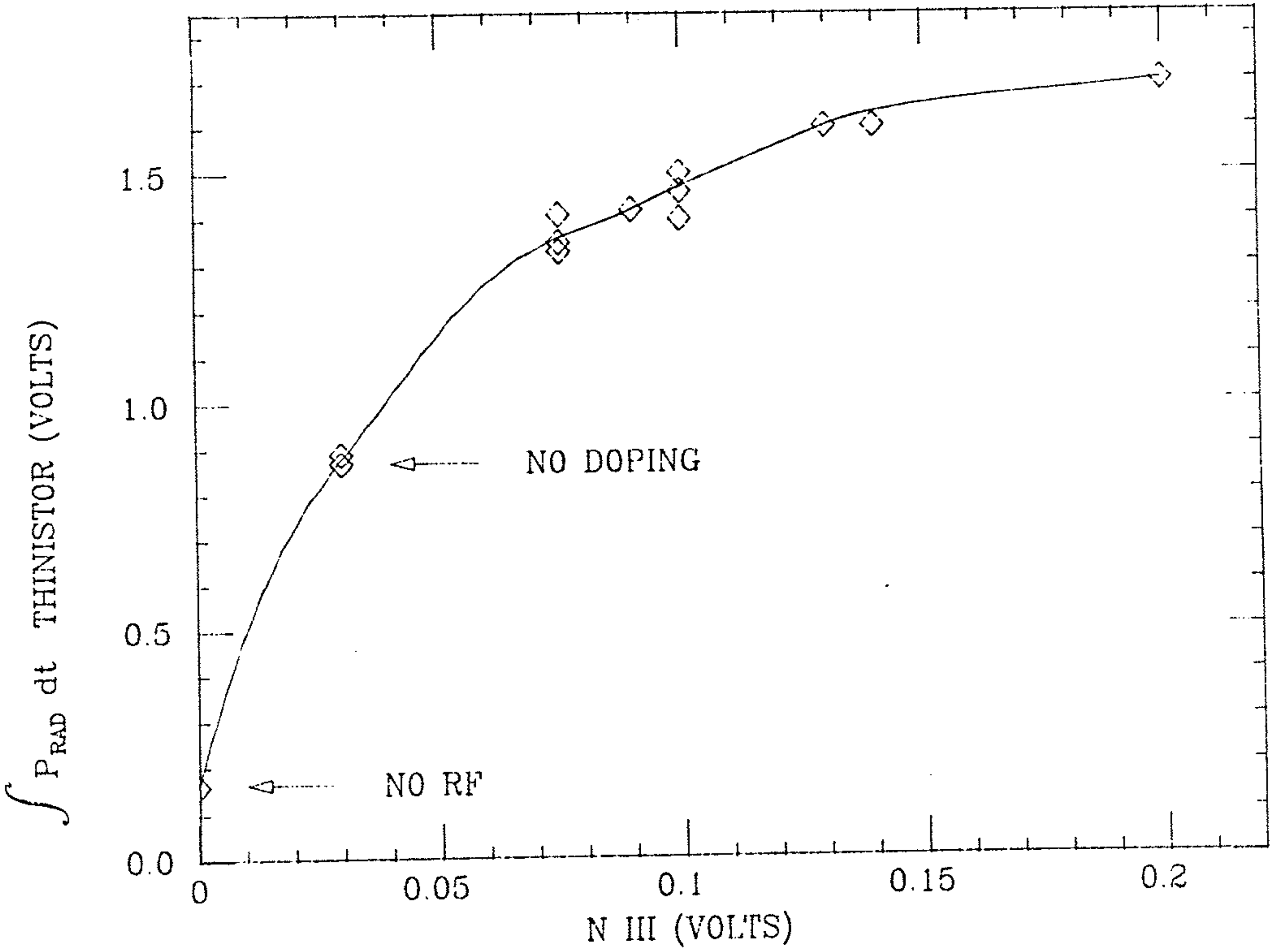
$\int P_{RAD}\,dt$ THINISTOR (VOLTS)
0.0
0.5
1.0
1.5
0
0.05
0.1
0.15
0.2
N III (VOLTS)
NO DOPING
NO RF

4.7 Power Balance

The data indicate that the hot ion energy confinement is dominated by charge exchange, and the electron energy confinement by impurity radiation. Calculations by Strait[7] considering classical ion heat conduction only, predict very large and sharply peaked ion temperature profiles, that are not consistent with the experimental data. Electron energy confinement times have been measured anywhere from ~1 to ~5 msec depending on machine cleanliness. The measured hot ion temperature varies little with electron energy confinement, consistent with the assertion that charge exchange is dominant for the hot ion species.

As a check to determine if coulomb collisions between the various species (hot ions, cold ions, and electrons) is consistent with the observed temperatures, a simple zero-dimensional computer code was written to calculate the time evolution of the temperature for each species. This is admittedly a crude model, and is only intended as a very rough check on the self consistency of the estimated power balance obtained when all the experimentally measured data (input power, confinement times, charge exchange losses, radiation losses, etc.) are combined. The processes included are: coulomb collisions between the various species, charge exchange on the ions, a loss term for the electrons to represent impurity radiation, and RF power into the hot ions. We solve simultaneously the following equations:

$$\frac{d}{dt}\left(\frac{3}{2}\, n_h\, T_h\right) = \frac{P_{RF}}{\mathrm{Vol.}} - \frac{3}{2}\,\frac{n_h(T_h-T_c)}{\tau_{ii}^{h/c}} - \frac{3}{2}\,\frac{n_h(T_h-T_e)}{\tau_{ie}} - \frac{P_{h\ c-x}}{\mathrm{Vol.}}$$

$$\frac{d}{dt}\left(\frac{3}{2}\, n_c T_c\right) = \frac{3}{2}\,\frac{n_c(T_h-T_c)}{\tau_{ii}^{c/h}} - \frac{3}{2}\,\frac{n_c(T_c-T_e)}{\tau_{ie}} - \frac{P_{c\ c-x}}{\mathrm{Vol.}}$$

$$\frac{d}{dt}\left(\frac{3}{2}\, n_e T_e\right) = \frac{3}{2}\,\frac{n_e(T_h-T_e)}{\tau_{ie}} + \frac{3}{2}\,\frac{n_e(T_c-T_c)}{\tau_{ie}} - \frac{3}{2}\,\frac{n_e T_e}{\tau_e(t)}$$

where,

$$\tau_{ii}^{h/c} = 7.34 \times 10^6\ (T_h+T_c)^{3/2}/n_c\ \ln\lambda\ \mathrm{sec}$$

$$\tau_{ii}^{c/h} = \tau_{ii}^{h/c}\,\frac{n_c}{n_h}\ \mathrm{sec}$$

$$\tau_{ie} = 3.15\times10^8\ T_e^{3/2}/n_e\ \ln\lambda\ \mathrm{sec}$$

$$\frac{P_{c-x}}{\text{Vol.}} = n_o n_i \int_o^\infty \sigma_{c-x}(E)\ v\ E\ f(E)\ d\ E$$

$$\simeq 1.83 \times 10^{-8}\ n_o\ n_i\ T_i^{4/3}\ \text{W/cm}^3$$

with temperature in eV and density in cm^{-3}. Inputs are initial temperatures, electron density, fraction of hot ions, RF power into hot ions, neutral density, effective volume, and electron energy confinement time (which itself can be time dependent if desired). Experimental parameters are used when possible, and fortunately the results are not extremely sensitive to any one parameter.

The plasma density, except for the very highest antenna voltage shots, decays less slowly with RF than without due to enhanced reflux. During the 10 msec RF pulse the loading changes $\lesssim$40%. Therefore, for simplicity the RF power and density were held constant in time. An example of the results is shown in Figs. 4.22 and 4.23. The input parameters were

$T_{ih} = T_{ic} = T_e = 10$ eV initial temperatures
0.4 hot ion fraction
5.0×10^{12} cm^{-3} electron density
500 kW RF input power for 10 msec
1.0×10^{10} cm^{-3} neutral density
4.3×10^6 cm^3 effective plasma volume,

Fig. 4.22 Time evolution of plasma temperature as calculated from zero-dimensional power balance.

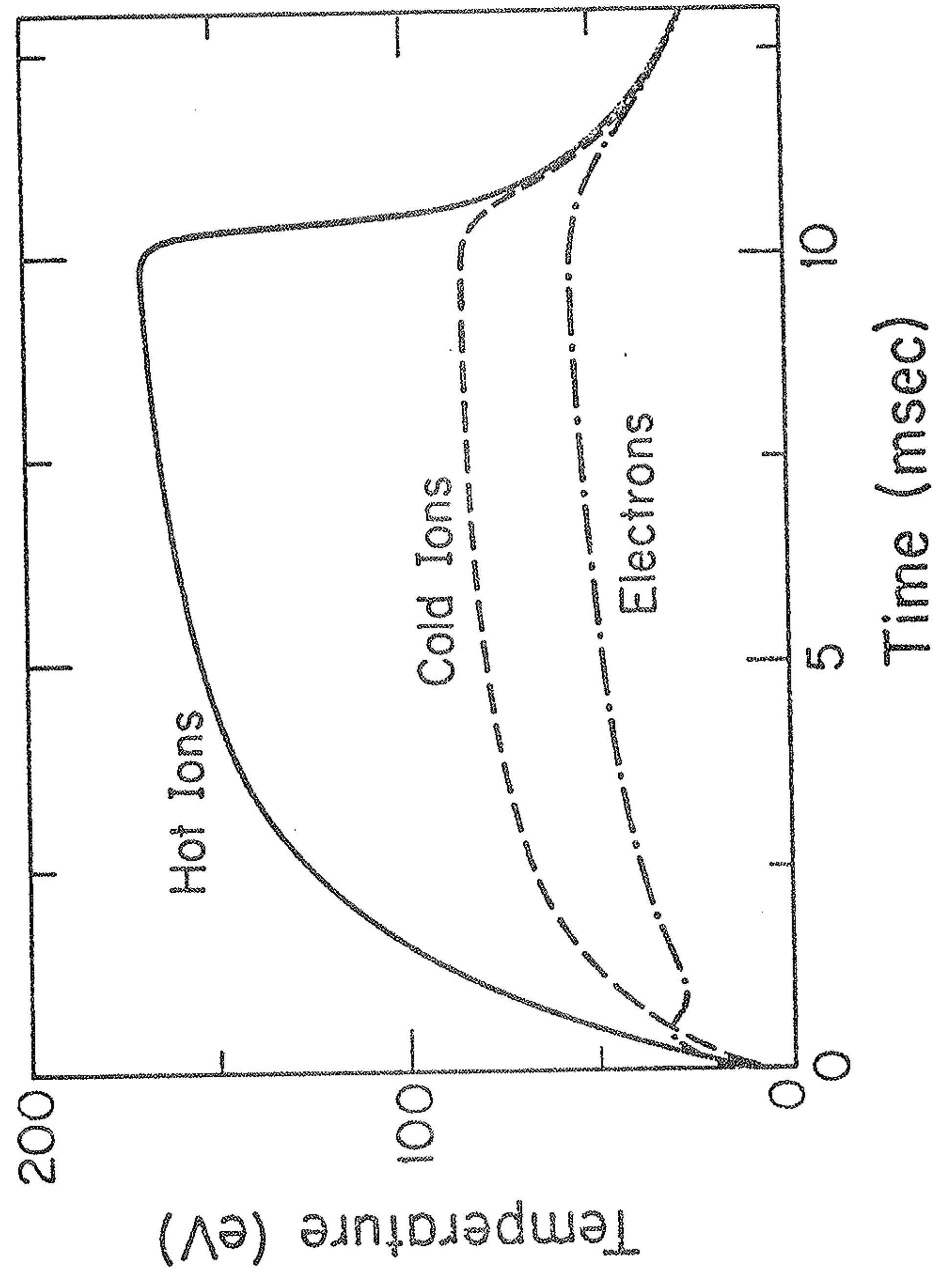
Hot Ions
Cold Ions
Electrons
Temperature (eV)
200
100
0
0
5
10
Time (msec)

Fig. 4.23 Energy losses calculated from zero-dimensional power balance.

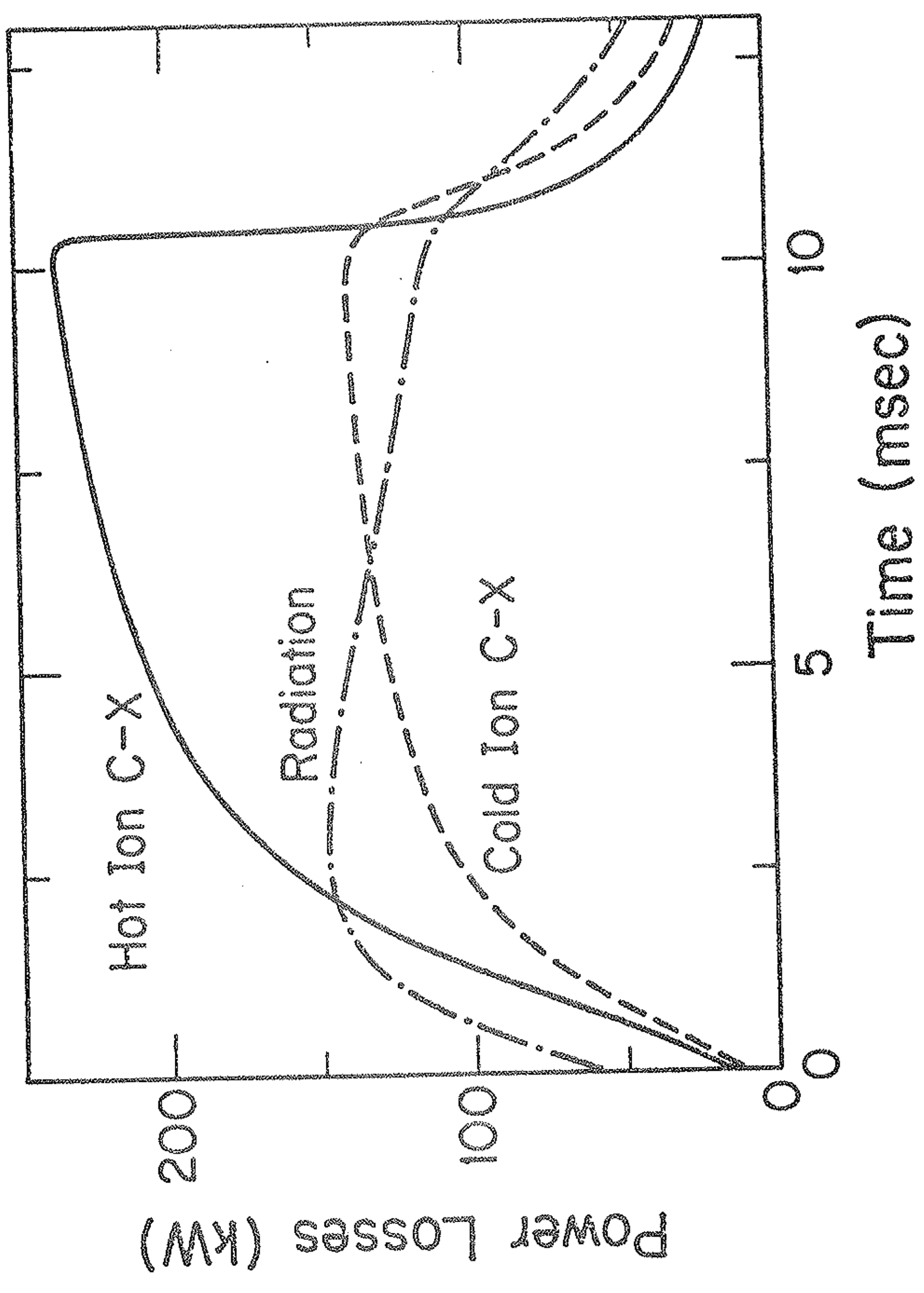
Hot Ion C–X
Radiation
Cold Ion C–X
Power Losses (kW)
200
100
0
Time (msec)
0
5
10

and the electron energy confinement time was assumed to increase linearly in time from 1 msec at t=0 to 3 msec at the end of the RF pulse to simulate the burning out of impurities. The neutral density of 1×10^{10} cm^{-3} is reasonable because it is about what the charge exchange analyzer predicts from its measured charge exchange power and relative hot and cold ion populations. A neutral density of 1×10^{10} cm^{-3} is equivalent to a pressure of 3×10^{-7} torr, which is a factor of 3-5 above the machine base pressure between shots. In any case, Figs. 4.22 and 4.23 predict temperatures and power losses that are similar to what is measured experimentally (see Fig. 4.8). Again, a zero-dimensional code cannot claim to model a very complex power balance, but it is at least satisfying that the predictions are in good qualitative agreement with the experiment.

For a representative shot, 500 kW of RF power is coupled into a 5×10^{12} cm^{-3} plasma with approximately half the power going out as charge exchange (Fig. 4.13). For clean plasmas ($T_e \gtrsim 40$ eV) no more than half the power is radiated (Fig. 4.21). The calculated equilibration times for the various species are all within the range of 1-2.5 msec and, as discussed above, are consistent with the observed temperature evolution.

REFERENCES - CHAPTER 4

1. C.M. Fortgang, University of Wisconsin PLP 890 (1983).
2. *The Radio Amateur´s Handbook*, R. Meyers, ed. (American Radio Relay League, Conn., 1975).
3. J.D. Jackson, *Classical Electrodynamics*, (John Wiley and Sons, N.Y., 1975), Chap. 8.
4. H.P. Eubank and T.P. Wilkerson, Rev. of Sci. Instr. 34, 12 (1963).
5. A.B. Ehrhardt, University of Wisconsin PLP 703 (1976).
6. D.C. Morin, University of Wisconsin PLP 524 (1973).
7. E.J. Strait, University of Wisconsin PLP 903 (1983).

CHAPTER 5

CONCLUSIONS AND PROPOSALS FOR FUTURE STUDY

Ion and electron heating have been observed with the application of radio frequency power in the ion cyclotron range of frequencies. Electron and ion temperatures are raised to 40-60 eV with an ion tail at 300 eV, which otherwise, without the application of RF, would be near 10 eV or less. Atomic processes dominate the power balance, the most important being charge exchange for the hot ions, and impurity radiation for the electrons.

The heating theory is tested by comparing the plasma loading with a theoretical heating rate calculation. The calculation uses a slab model and considers more complicated effects such as finite temperature and the antenna parallel wavelength spectrum. We have shown reasonable agreement between theory and experiment with regard to the loading.

This thesis tried to touch on all the relevant aspects of a heating experiment; however, there are certain questions that merit further investigation.

Ion saturation current profiles at various toroidal positions but at a constant poloidal angle, (preferably near the antenna), would be useful in determining if the local high electric fields at the antenna, or the hotter plasma as a whole, is responsible for enhanced particle losses with RF.

Further ion temperature measurements with the gridded energy analyzer probe are needed. Specifically, insertion of the probe on the midcylinder near the lower lid will detect ions with large perpendicular energy, mirror trapped over the antenna.

Loading measurements over a wider region of parameter space would be useful. In particular at low density, 10^{11} cm^{-3}, it is predicted that the plasma shielding of the left-hand component of the RF electric field decreases, and the simpler calculation of the heating rate with the vacuum electric field becomes more applicable. However, these measurements are difficult to make with the present technique, because at low density, power losses are dominated by the antenna itself, making for large error bars in the data.

Recently a second antenna has been installed on the top lid, directly above the antenna used for this thesis. Besides being able to increase the input power with the second antenna, there are some interesting physics experiments that can be performed by using the two antennas in conjunction. At high densities, it might be possible to set up poloidal eigenmodes which could be detected by using the second antenna as an electrostatically shielded $\dot{B}$ probe. Also, we have recently installed new limiters on the bottom antenna, closer to the Faraday shield, in an attempt to shorten the parallel wavelengths excited by the antenna. The heating model predicts that this will enhance the heating rate, and, with the second antenna, we can directly compare the loading with and without limiters close to the Faraday shield.

Of course, most of the experiments performed for this thesis can be redone with two high power sources, running together during a shot, either in parallel or series. We expect that more RF power will result in better bulk heating, and therefore, more interesting plasmas with which to do experiments.